Protection Optimisation via Novel Simulation – A Bridge to the Next Generation of Armour Development

David Anthony Howells, MEng

Submitted to Swansea University in fulfilment of the requirements for the degree of Doctor of Philosophy

Swansea University

2023

Abstract

Primary blast lung injury is a contributor to lethality in both military and civilian life. Mitigation of such injuries is a topic which would benefit from deeper investigations of the mechanism(s) by which these injuries manifest. For this purpose, this study has developed 1D and 3D finite element models alongside physical models of the human thorax to be used in blast simulations and experimental testing respectively.

The initial hypothesis was that injury was governed by the action of stress waves within a few milliseconds after loading begins. The threshold of injury scenario outlined in the literature was investigated with consideration for the differences in loading (long-duration and short-duration). A comparison of the 1D and 3D computational models indicated that 1D modelling was insufficient in capturing the requirements for accurately predicting blast injury.

Several parameters were explored computationally as metrics for prediction of primary blast lung injury. The conclusion formed was that tensive stress presents the most consistent indicator of injury in both long-duration and short-duration blasts. A value of 8.7kPa was proposed as a threshold value for injury using this parameter. This is substantially lower than the external loads applied. Distributions of all stresses in the 3D computational models were indicative of realistic injury distribution, proven through comparison of the time varying position of stress contours with CT images of PBLI victims.

A reduced-scale physical thorax model was constructed following a material characterisation study of PolyJet materials. Experimental blast loading of this model using a shock tube indicating that the external load was representative of the internal loads. Results were inconclusive due to excessive vibrations, however there are indications that reflections scattered by the mediastinum were detected. This first iteration of the model can undergo significant improvements and represents a promising platform for future investigations of primary blast lung injury.
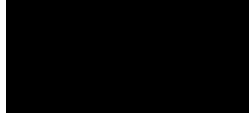
Declarations

This work has not previously been accepted in substance for any degree and is not being concurrently submitted in candidature for any degree.

Signed………David…Anthony…Howells…………………………………..
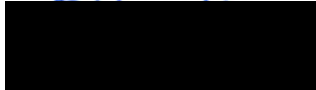
Date…………30/06/23……………………………………………………………….

This thesis is the result of my own investigations, except where otherwise stated. Other sources are acknowledged by footnotes giving explicit references. A bibliography is appended.

Signed…………David…Anthony…Howells………………………………...

Date…………30/06/23……………………………………………………………….

I hereby give consent for my thesis, if accepted, to be available for electronic sharing.

Signed…………David…Anthony…Howells………………………… …...

Date…………30/06/23……………………………………………………………….

The University's ethical procedures have been followed and, where appropriate, that ethical approval has been granted.

Signed……………David...Anthony...Howells…………………………… .

Date…………30/06/23……………………………………………………………….

Contents Page

Dedication

This thesis is dedicated to the memory of my grandmother and grandfather. Though they may not have been able to witness the end of this journey, I am certain that this conclusion was long envisioned by them with far greater clarity than I. Their love, support, and confidence in me has been a great guiding hand through difficult times and I hope I have made them proud.

It is further dedicated to all the friends, family, and work colleagues who have supported me in this endeavour. I could not have done this without the many kind words, advice, long discussions, and financial support that I've been blessed with. Thank you all for your unending efforts.

Acknowledgements

List of Figures

Figures

Lists of Acronyms and Tables

Acronyms

ALE	*Arbitrary Lagrangian-Eulerian*
AM	*Additive Manufactured*
ASII	*Adjusted Severity of Injury Index*
ATD	*Anthropomorphic Test Device*
BTD	*Blast Test Device*
CEL	*Coupled Eulerian-Lagrangian*
CONWEP	*Conventional Weapons*
FE	*Finite Element*
ODE	*Ordinary Differential Equation*
PBLI	*Primary Blast Lung Injury*
SDOF	*Single Degree of Freedom*
WE	*Wave Equation (1D)*

Tables

List of Equations

Equations

1. Introduction to Blast Loading

1.1 Blast Threat

The blast from an explosive event is an ever-present modern threat around the globe. From distant military conflicts to industrial accidents, the potential for explosive detonations remains an unfortunate likelihood and the need for protection systems is vital to minimising life-changing injuries and threat to life. Although effective systems can already be produced and are being continually developed, a stronger understanding of the mechanisms by which injuries are inflicted can lead to greater protective effectiveness and/or efficiency. Steps towards improved protection include greater precision in mitigating specific causes of injury and identifying anatomical locations at greatest risk. This information is also important to reduce inadvertent increases to the risk of injury whilst making design choices (i.e., exacerbating one mechanism of injury whilst attempting to limit another). This study aims to introduce the threat posed by blasts, seek improvements in understanding the mechanisms of injury, and provide a step towards developing a computational model capable of better assessing injury risks to improve the design of the next generation of protection systems.

The significance of blasts is most apparent in military conflicts, demonstrating the prevalence and severity of injuries that can be inflicted. Reports indicate that more than 50% of injuries in action within conflicts of the Yugoslav wars (1991-1992) were inflicted by blast devices [1]. Furthermore, a report on UK military activity in Afghanistan from 2006 to 2007 found that 66% of deaths were attributed to the effects of blasts. In this same conflict, primary blast lung injury (PBLI) was identified in 7% of injured personnel in Iraq and 11% of cases in Afghanistan [2]. The presence can increase up to almost 80% of non-survivors within whom it was the sole cause of mortality in 17% of these studied cases [3]. These statistics show the prevalence of blast injury, particularly PBLI, as a leading contributor to mortality rates. This remains an ongoing concern in the world as inactive warzones continue to claim lives, usually through minefields, and new conflicts inevitably arise, such as the ongoing war in Ukraine.

Blasts originate from a chemical process of exothermic oxidation of an explosive material, a subset of the energetic material classification. This process generally requires a fuel, oxidiser, and an initiator of the reaction. High-order explosives will constitute both the fuel and oxidiser, producing a rapid reaction known as a detonation. Low-order explosives have separate chemical compounds for the fuel and oxidiser and produce a burning reaction of deflagration, a much slower reaction. Both reactions cause the release of energy and a phase change from solid/liquid to gas. The rapid expansion of product gases is the definition of an explosion, which is readily achieved in the detonation reaction

but can also be generated in deflagration in confined spaces [4]. The consequences of an explosion are categorised as blast modes based on the different types of loading produced throughout the event.

1.2   Blast Modes

During an explosion, there are several resulting modes through which damage can be inflicted to an object or injury to a person. Although impersonal, this study will often refer to both as "subjects" due to both being potential targets/victims in explosive attacks or accidents. A subject will likely be exposed to several blast modes simultaneously, creating a complex series of loads. The dominance of each mode is dependent on the explosive material/device detonated and the environment in which the detonation occurs which may amplify or mitigate specific modes. Whilst this study will ultimately focus on the primary mode, it is important to understand the role each has in mortality rates and how the mechanism of injury differs between each. An overview of detonation products and their injurious effects is shown in figure 1 overleaf.

The primary mode of a blast refers to the compression of air around the explosive material. The oxidation reaction creates product gases rapidly, compressing the surrounding air into a region of high pressure. This is typically spherically shaped around the explosive though it can depend on the geometry of the explosive itself and the surrounding environment. This region of compressed air, referred to as a shock front, will expand outwards from the explosive at supersonic speeds governed by the pressure difference of the air. Pressure magnitude in the shock front will decay with increasing distance from its origin. A spatial point will experience the passing of the shock front as a near instantaneous rise in pressure (on the order of micro-seconds) followed by a period of decay (several milliseconds). When impacting on a subject, a compressive load is applied to its surface [1, 3-6]. This mode is particularly known for being an invisible killer for two reasons: as it propagates as air it can be difficult to see with the naked eye, and the type of loading applied to surfaces can penetrate through materials. This respectively means it can be difficult to determine subjects affected by it, and the damage it creates can be difficult to detect as it may be internal with no presence at the surface through which it entered [1, 3-6].

The secondary mode concerns the impact of small or sharp fragments that are generated during the detonation event. Fragments can originate from casing(s) around the explosive material or destruction of surrounding geometry. Fragments are accelerated by direct imparting of kinetic energy during detonation or the passing of the shock front. When they impact a subject, they penetrate the surface, which is a key characteristic of this mode of injury. For a victim, this could mean bleeding, tissue trauma, and loss of organ function, all resulting in potential mortality [1, 4, 6, 7]. Much of the probability of risk of this mode of injury is due to the range of the fragments generated (dependent on the force generated by the explosive), the number of fragments (dependent on the design of an

explosive and the environment), and the exact location where the injury occurs. It is difficult to predict where a fragment will impact in a realistic blast event, particularly for improvised explosive devices [4]. Recent studies have focused on capturing typical fragment impact locations within statistically significant ranges with validation through experiments [8]. For optimisation of protection, it can be identified which locations would be the most detrimental to receive such injuries. For example, a fragment penetrating a vital organ would have much greater probability of causing mortality. From this basis, efforts have been made to predict the likelihood of penetration of soft tissues and fracture of bones based on standardised fragment shapes. Further analysis has been performed on the expected shape of a wound including damage to proximal tissues [4, 6, 7, 9, 10].

Tertiary injury mode also describes damage due to impacts, but more precisely from collisions between larger objects that are not penetrative. For example, tertiary mode includes impact from large debris or movement of the subject itself into the surrounding environment. This can lead to a similar type of loading as primary mode, a pulse of high magnitude pressure acting on a surface for a duration. Compared to primary blast mode, this loading is usually reduced in magnitude but acts over a longer duration. The presence of this mode is highly dependent on the context of the blast scenario (charge size, environment, subject, etc.) [1, 4, 6, 11, 12].

Additionally, quaternary and quinary modes have been discussed in the literature. Quaternary refers to damage resulting from chemical or burning effects (such as the inhalation of toxic gases or burns from the generation of a fireball). The definition of quinary can vary however it is generally used to refer to clinical effects that are not specifically generated by the explosive material, such as injury due to the immune response of the body (such as inflammation) or psychological considerations. The presence of these effects is highly dependent on the explosive device and/or the bodies response to injury [4, 6, 12-16].

1)	Primary Injury	–	Pressure Loading from the Blast Wave (Lead Edge Known as the Shock Front)
2)	Secondary Injury	–	Impact of Accelerated Small Fragments (Usually Penetrative into the Subject)
3)	Tertiary Injury	–	Bodily Displacement of the Subject (and Subsequent Collision with Surroundings)
4)	Quaternary Injury	–	Detonation Products Such as Flames or Toxic Gases (Burning and Poisoning)
5)	Quinary Injury	–	Biological Responses to Trauma (Immune Response or Psychological Effects)

Figure 1: Diagram of varying injurious blast modes and their sources.

Amongst all these modes of injury, primary blasts effects have received the most attention for research. Loading from this mode is certainly present in all blast scenarios and has a high probability of lethality when the subject is situated near the explosive. It is present in many victims regardless of the cause of mortality yet can also be the sole contributor to mortality. It is known that internal organs are at risk of injury from this mode due to the penetrative nature of the loading, and fluid-filled organs such as the ear and lungs are at highest risk. Research in this field has focussed on traumatic brain injury and primary blast lung injury (PBLI), two leading causes of injury in blast events. Due to the prevalence of this mode of injury, its contribution to mortality, and the vulnerability of the lungs specifically, this study elects to delve deeper into understanding the mechanics of PBLI, which must first begin by understanding the physics by which the loading is applied.

1.3　　　Primary Blast Physics

As previously discussed, the shock front is a region of compressed air that is formed around an explosive due to the rapid generation of product gases in the chemical reaction of detonation. The shock front will expand outwards driven by the pressure differences in the air. This is generally described as being spherical (if detonation occurs above ground-level) or hemispherical (if detonation occurs at ground-level) in shape. These are referred to as air-bursts and ground-bursts respectively. The pressure relationships and propagation process are defined by the Rankine-Hugoniot jump relations and can be predicted by several methods of approximation based on experimental data. At its most simplified, the process is that of a compressive wave, many characteristics of which will become apparent in this chapter [11, 17-19].

The translation of the shock front is dependent it's velocity, which can be expressed by equation 1. This can be used to predict the velocity of the air particles in the shock front using equation 2 [17, 19].

$$U_s = c^2 \sqrt{\frac{6P_s + 7P_0}{7P_0}} \tag{1}$$

$$U_p = \frac{c\left(\frac{5}{6}\right)\left(\left(\frac{U_s}{c}\right)^2 - 1\right)}{\frac{U_s}{c}} \tag{2}$$

In equations 1 and 2 U_s is the velocity of the shock front, c is the speed of sound in the medium (approximately 342m/s for ambient air), P_s is the peak static pressure of the shock front, P_0 is the atmospheric pressure (approximately 101325Pa for ambient air), and U_p is the velocity of the air particles within the shock front.

As the shock front travels and the radius of the spherical expansion increases there is a reduction in magnitude of its pressure primarily caused by the increasing volume over which the shock front is acting [4, 19-21]. This will be referred to as spatial decay. As the energy dissipates in three dimensions, it is expected to reduce following an inverse cube function of the radius. The passing of the shock front at a fixed point in space will cause a rapid (on the order of microseconds, often treated as instantaneous) rise in pressure to a peak above atmospheric norms which will then decay as the pressure is relieved gradually (over several milliseconds). This will be referred to as temporal decay [4, 19, 21].

Following the shock front is the blast wind, a volume of gas translated at a high speed. In turn, this is followed by a release wave, in which the direction of travel is reversed and air refills the space it was previously forced out of. This can be apparent on pressure histories as a negative phase where pressure is reduced below atmospheric norms to a peak under-pressure, though with a much-reduced magnitude compared to the preceding peak over-pressure [3, 19].

The surroundings will have a significant effect on this temporal profile with a standard definition existing in the form of a Friedlander profile which would be expected in an ideal environment. An ideal environment is defined as being an open field with no obstacles or geometry present in the path of the blast wave propagation. This environment is unlikely to exist, instead a blast will occur in a complex environment with many surfaces which will cause reflections. Reflections generate additional waves travelling in various directions causing a temporal profile to experience several peaks of over- and under-pressure with varying durations. A comparison of a Friedlander profile and a realistic pressure history can be found in figure 2. Friedlander profiles of the over-pressure can be generated using equation 3 overleaf [4, 19, 22].
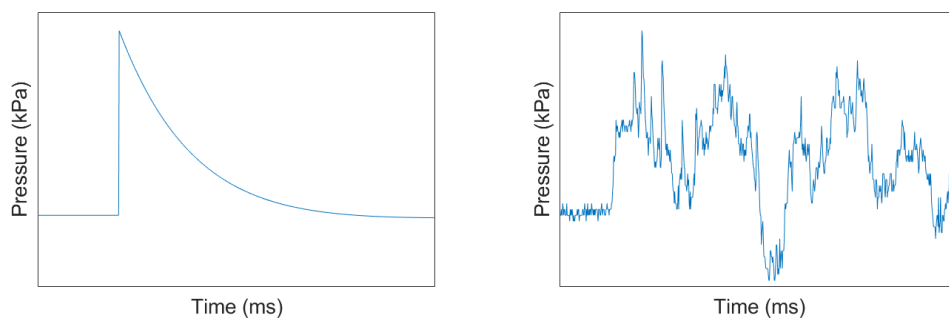
Figure 2: Examples of an idealised Friedlander waveform (left) expected in a theoretical open field, and a complex waveform (right) expected in an experimental setting. Typical injury inducing static pressure magnitudes range from approximately 60kPa to 1100kPa, with durations ranging from 0.1ms to greater than 10ms according to the Bass Lethality Curves [34]. This range highlights how magnitude and impulse are both factors in predicting injury.

$$p_s(t) = P_s \left(1 - \frac{t}{T}\right) e^{-\frac{bt}{T}} \qquad (3)$$

In equation 3 p_s is the time-dependent static pressure, t is time, T is the duration of the positive phase of the waveform, and b is a decay constant. This equation can also be used to generate idealised reflected pressure histories with corresponding constants.

Pressure measurements can be referred to as static or reflected depending on where and how the measurement is taken. Static pressure refers to a hydrostatic pressure accounting for forces resultant from the random motion of the air particles, but not due to the translation of the gas itself. Static pressure can be measured experimentally using a sensor with a surface parallel to the direction of blast propagation. This is a measurement which does not influence the pressure acting at that location. When a sensor is used to measure the pressure with a surface perpendicular to the direction of blast propagation, this would be a reflected pressure which is significantly greater than a static pressure magnitude [4, 17, 19]. This phenomenon is due to the nature of stress transfer at the boundary between two materials.

Wave reflections are governed by the acoustic impedance of a material, a value representing the material's resistance to excitation of its particles. This is dependent on density and elastic modulus (see equation 4 below). A compressive wave imparts its potential energy to the medium it propagates in as kinetic energy. When the medium cannot be translated, it is instead stressed as the material experiences strain. At boundaries between materials the stress must remain constant across both sides of the boundary. From this behaviour, we can predict the loads expected at simple boundaries using the expressions shown in equations 5 and 6 [4, 23].

$$Z = \rho c \qquad (4)$$

$$R = \frac{Z_1 - Z_2}{Z_1 + Z_2} \qquad (5)$$

$$T = \frac{2Z_2}{Z_1 + Z_2} \qquad (6)$$

In equations 4, 5, and 6 Z is the acoustic impedance, ρ is the density, in the material, R is the reflectivity of a boundary and T is the transmissivity of a boundary. Subscripts indicate which order the wave propagates through the materials.

The reflectivity and transmissivity constants describe the fraction by which the incident stress will be modified at the boundary. When considering the compressive and tensive nature of the wave as positive and negative respectively, it must also be considered that a forward propagating wave is treated as travelling in the positive direction and a backward propagating wave is negative. For example, consider the following three scenarios [4]:

1) When both materials have the same acoustic impedance, the wave will propagate across the boundary with no change in stress magnitude. The materials have identical behaviour when exposed to the loading. No reflected waves are generated.

2) When the second material has lower acoustic impedance that the first material a positive reflectivity is generated along with a positive transmissivity less than unity. This represents the physical behaviour in which the particles of the first material experience reduced resistance to motion due to the reduced stiffness of neighbouring particles and so the first material can be more easily translated. This relieves the stress in the first material whilst the second material experiences only this reduced stress. The positive reflectivity represents a backwards propagating wave of negative magnitude, interacting with the incident wave destructively to reduce the stress (see figure 3).

3) When the second material has greater acoustic impedance than the first material, a negative reflectivity is generated along with a positive transmissivity greater than unity. In this scenario the second material is stiffer and attempts to dampen the oscillations of the first material. This leads to reduction in translational motion but an increase in stress. The second material will experience a stress greater than the incident stress (transmissivity greater than unity) and the backwards propagating positive wave will interact constructively with the incident wave to increase the stress (see figure 4).

This phenomenon partly explains why fluid-filled organs are at particular risk to primary mode of blast loading: the difference of acoustic impedance at the boundary between the materials is greater than elsewhere in the body, leading to higher magnitude reflections and greater motion of the materials. When these boundaries suffer damage, it is often due to spalling, the rupture of the stiffer material that then invades the softer material [1, 4, 12, 21].
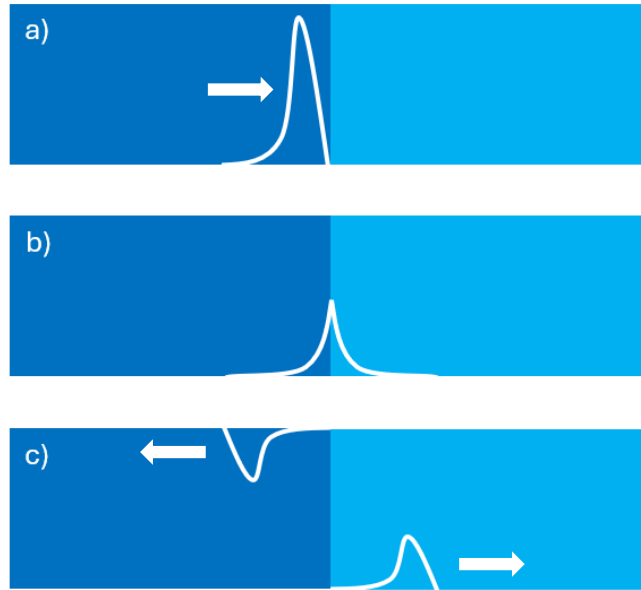
Figure 3: Diagram showing a wave transferring from a high acoustic impedance material (dark) to a low acoustic impedance material (light). Low acoustic impedance material is translated, relieving the stress in both materials. Part a) shows the high magnitude compressive wave approaching the interface, part b) shows the reduction in magnitude at the interface, and part c) shows the reduced magnitude backwards propagating tensile wave in the first material and forward propagating compressive wave in the second material.
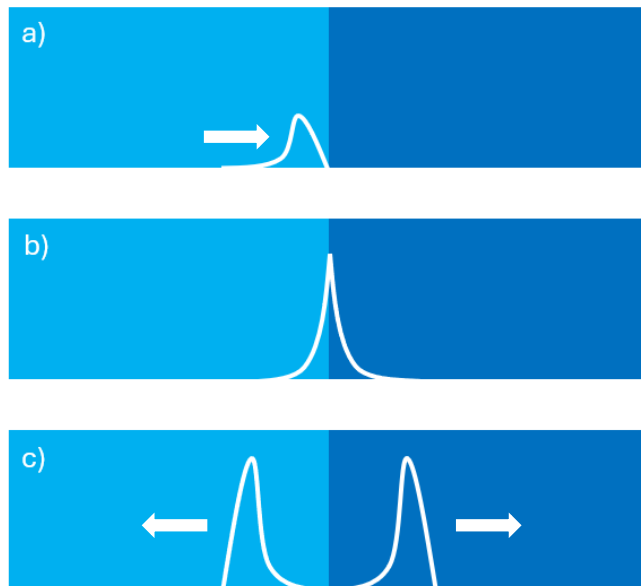
Figure 4: Diagram showing a wave transferring from a low acoustic impedance material (light) to a high acoustic impedance material (dark). High acoustic impedance material resists translation, increasing the stress in both materials. Part a) shows the low magnitude compressive wave approaching the interface, part b) shows the increase in magnitude at the interface, and part c) shows the increased magnitude compressive waves propagating in opposite directions.

This behaviour is also apparent in the concept of static and reflective pressures, with air acting as a low stiffness material and a surface as the high stiffness material. The process can be considered physically as a confinement of the motion of the air particles causing pressure to increase in the immediate vicinity of the surface. However, the loading experienced by the surface will also be affected by the angle of incidence and the size of the surface. Angled and small surfaces allow pressure to be cleared as particles travel across and away from the surface (such as around the edges of a surface). In such cases, the reflected pressure will be less than theoretically predicted as the rate of decay will be increased [4, 19, 24].

The effects of clearing on small surfaces can be approximated from equation 7. This method predicts a duration after arrival of the wave for which the pressure will experience an increased rate of decay. After this duration, it is predicted that the load will be the sum of the static and dynamic pressure. Dynamic pressure refers to forces created by the translational motion of air particles within the volume through which the shock front has passed through (i.e., pressure due to the blast wind). Whilst dynamic pressure is significantly reduced compared to static or reflected pressures, it acts over a much longer duration [19].

$$T_c = \frac{4S_c}{(1 + R_c)c} \qquad (7)$$

In equation 7 T_c is the clearing duration, and S_c and R_c are respectively the minima and maxima of the values of height of a surface and half of the width of a surface which is bounded by the ground.

1.4   Predicting Blast Loading

It has been established in the previous section that the loading produced on a surface is dependent on the offset distance to the blast source and the environment it exists within [4, 19-24]. It is also highly dependent on the material detonated. Generally, TNT is used as a reference by which other explosives are compared to. Equation 8 presents a scaling law used to compare charges based on the ratio of their heats produced during detonation [6, 19].

$$W_{TNT} = W_x \left(\frac{H_x}{H_{TNT}} \right) \qquad (8)$$

In equation 8 W_{TNT} is the mass of the charge referred to as charge weight, H is the heat of detonation specific to an explosive material, and the subscript refers to the explosive materials being converted. Table A contains data for some common explosive materials.

There are several proposed analytical methods for predicting the blast load produced by a specified explosive material with a known mass at a variable offset distance. Most of them are reliant on the

concept of scaled distance proposed by Hopkinson-Cranz [17, 19]. Equation 9 describes the relationship between the offset distance and the mass of a charge. This scaling law can be used to find the offset distances at which different masses of an explosive material will produce similar blast loading magnitude.

Table A – Heat of Detonation for Common Explosive Materials

Explosive Material	Heat of Detonation (MJ/kg)
TNT	4.1 – 4.55
C4	5.86
RDX	5.13 – 6.19
PETN	6.69
Pentolite 50/50	5.86
Nitroglycerin	6.3
Nitromethane	6.4
Nitrocellulose	10.6
Amonium Nitrate	1.59

$$Z_x = \frac{R_x}{\sqrt[3]{W_x}}$$

(9)

In equation 9 Z_x is the scaled distance and R_x is the offset distance of a point of interest from the blast source. The scaled distance is used in equations proposed by Kinney, Brode, Newmark, Mills, and Kingery-Bulsmash for predicting peak pressure magnitudes [17, 19].

The most widely used method for calculating blast loads is from a study by Kingery and Bulmash in which curves were fit to experimental data of pressure history measurements. There exist two sets of data, one for spherical air-bursts and the other for hemispherical ground-bursts. The methodology has seen widespread use in many studies and has since been adapted into the CONWEP (CONventional WEaPons) system for numerical simulations [18, 20]. This system will be discussed in greater depth in chapter 3, focusing on validation of computational methodologies for blast loading.

The Kingery-Bulmash data is shown overleaf in figure 5. This data can be used to find several key characteristics of blast loading including peak static pressure, peak reflected pressure, impulse of static pressure, impulse of reflected pressure, arrival time of the incident blast wave, duration of the positive phase of loading, shock wave speed, and blast wavelength. Additionally, a Friedlander decay constant can be approximated from equation 10 developed by Karlos using the parameters in tables B and C. This study aimed to develop a direct calculation of decay constant (as opposed to iterative

approximation) and utilise modern data to improve reliability of the methodology, which has been questioned in its accuracy for spherical expansions [19, 25-27].
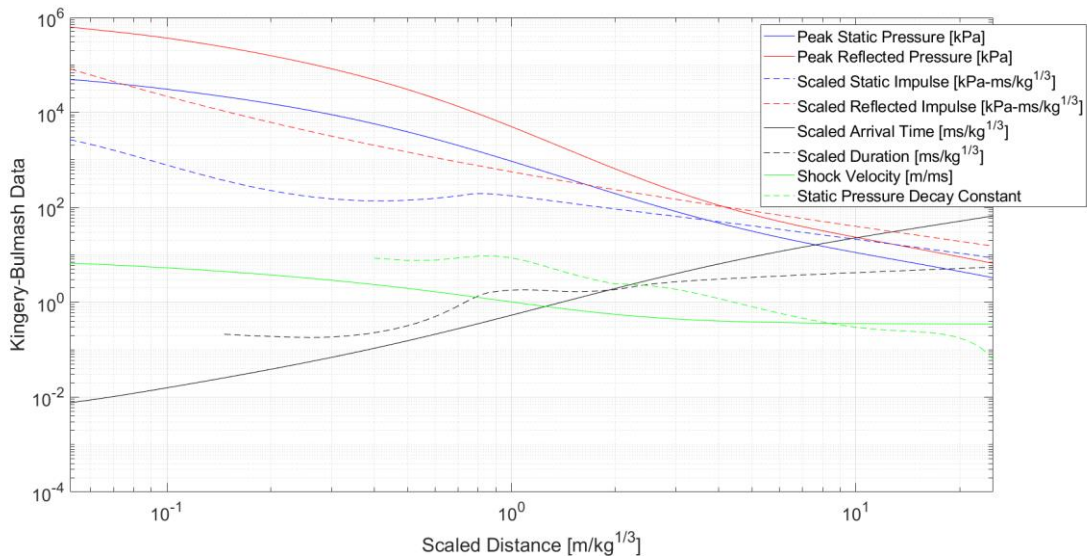
Figure 5: Kingery-Bulmash empirical data of spherical expansion blast wave propagation. Data can be used to generate pressure histories using the Friedlander equation. It should be noted that hemi-spherical expansion data is also available [27]. Scaled parameters are normalised with respect to the cube root of the charge weight. Decay constant is included through the work of Karlos [19, 25]. See equation 10 and tables B and C for more information.

$$\log_{10} b = C_0 + C_1 (K_0 + K_1 \log_{10} Z_x)^1 + \cdots C_n (K_0 + K_1 \log_{10} Z_x)^n \qquad (10)$$

Table B – Coefficients for Calculation of Decay Constant of Ideal Spherical Expansion

	Static		Reflected	
Parameter	$0.4 \leq Z_x < 2.0$	$2.0 \leq Z_x < 40.0$	$0.4 \leq Z_x < 2.0$	$2.0 \leq Z_x < 40.0$
K_0	-1.21918	0.91029	-1.19297	-0.81111
K_1	-1.02211	-1.30156	-2.1578	-0.79605
C_0	-48.18977	-0.09812	2.06997	36.02749
C_1	-149.9999	1.35537	16.80778	131.07634
C_2	-98.92512	0.3035	72.93669	149.9999
C_3	62.44699	-1.25125	149.9999	24.5694
C_4	30.85296	-2.43775	144.25099	-45.12465
C_5	-37.17606	-2.88558	32.36555	-1.25611
C_6	15.40019	6.77186	-33.83582	15.84096
C_7	10.37512	5.93303	-4.03564	-0.979
C_8	-9.26648	-11.10183	14.50199	-0.1457
C_9	9.01084	7.47192	1.0377	4.87916
C_{10}	1.86709	15.76656	-0.74065	2.68134
C_{11}	0.15419	-17.02748	4.07724	0.41271
C_{12}	5.08837	-16.90636	-2.76428	
C_{13}	1.0771		0.49798	
C_{14}	2.46682			
C_{15}	3.61837			
C_{16}	1.10167			

Table C – Coefficients for Calculation of Decay Constant of Ideal Hemi-Spherical Expansion

Parameter	Static		Reflected	
	$0.4 \leq Z_x < 2.5$	$2.5 \leq Z_x < 40.0$	$0.4 \leq Z_x < 2.5$	$2.5 \leq Z_x < 40.0$
K_0	-1.207	-0.47633	-1.39431	-0.88388
K_1	-0.6075	-0.40484	-1.131	-0.40506
C_0	-80.82064	-20.49905	-35.3029	-85.67879
C_1	-149.9999	-86.59057	-99.999	-149.999
C_2	5.86418	-130.60904	-69.1698	-0.2713
C_3	70.33463	-81.27717	22.58236	65.50689
C_4	-39.78227	14.4792	21.11283	-31.6652
C_5	1.36248	41.6428	-10.2301	-13.82701
C_6	23.70363	-26.25798	2.92917	23.51511
C_7	-15.88316	-10.67766	6.19783	-3.1931
C_8	9.64966	26.18665	-0.07562	-1.94955
C_9	4.18554	-16.53561	3.04334	7.25556
C_{10}	-2.36102	15.2393	3.38368	1.90496
C_{11}	6.42156	18.91375	0.80842	-0.39521
C_{12}	0.85025	-21.4657		
C_{13}	2.47613	6.92392		
C_{14}	3.0465	14.999		
C_{15}	2.12009	0.06951		
C_{16}	2.88949			
C_{17}	1.1488			

In equation 10 (and tables B and C) b is the decay coefficient associated with a Friedlander blast profile, Z_x is the scaled distance, and n is the polynomial order. Coefficients K and C are defined through least-squares fitting to analytically calculated b values carried out by Karlos et al [25] with polynomial order termination defined by error less than 3%.

It should be noted that the lower limit of these expressions for the decay constant are set as a scaled distance of 0.4m/kg^3. This is because it has been argued that the original Kingery-Bulmash data was based on less rigorous testing below this value leading to less accurate predictions. Smaller scaled distances can experience greater fluctuations in measurements as in the immediate vicinity of the charge the shock formation does not necessarily exhibit idealised behaviour. At such short timescales, the blast is yet to form a stable shock front that could be assumed to be uniform.

From a known explosive material of a specific charge weight, a conversion to TNT can be performed, a scaled distance calculated, and the Kingery-Bulmash data used to predict the idealised loading that will be applied. This process can be reversed to identify the expected charge weight or can be used to predict pressures upstream/downstream of a location with a known blast history. This methodology will be used throughout the studies contained in this thesis to assess experimental data and determine blast loads representative of risks for PBLI. To understand PBLI, the appropriate anatomy and physiological effects must first be explored.

2. Biological Tissues Under Blast Loading

2.1   Anatomy of the Human Thorax

When a shock front applies loading to a biological subject, it has already been made clear that the organs most at risk are those which are gas-filled. Common examples are the ears and the lungs, injury to the latter of which from loading originating from a shock front is referred to as Primary Blast Lung Injury (PBLI). The lungs are within the thorax (chest) flanking the mediastinum, a term encompassing the structures that form a vertical pillar through the human thorax, connecting the head to the abdomen. Structures within the mediastinum include the heart, several large blood vessels such as the aortic arch, the oesophagus, and the trachea [4, 6, 13, 28, 29]. The anatomy of the thorax will be discussed in greater detail presently; however, readers should refer to figures 6 and 7 for visual guides to the most significant structures/features. Readers should also refer to figure 8 in section 2.2 for CT images of the anatomy discussed.
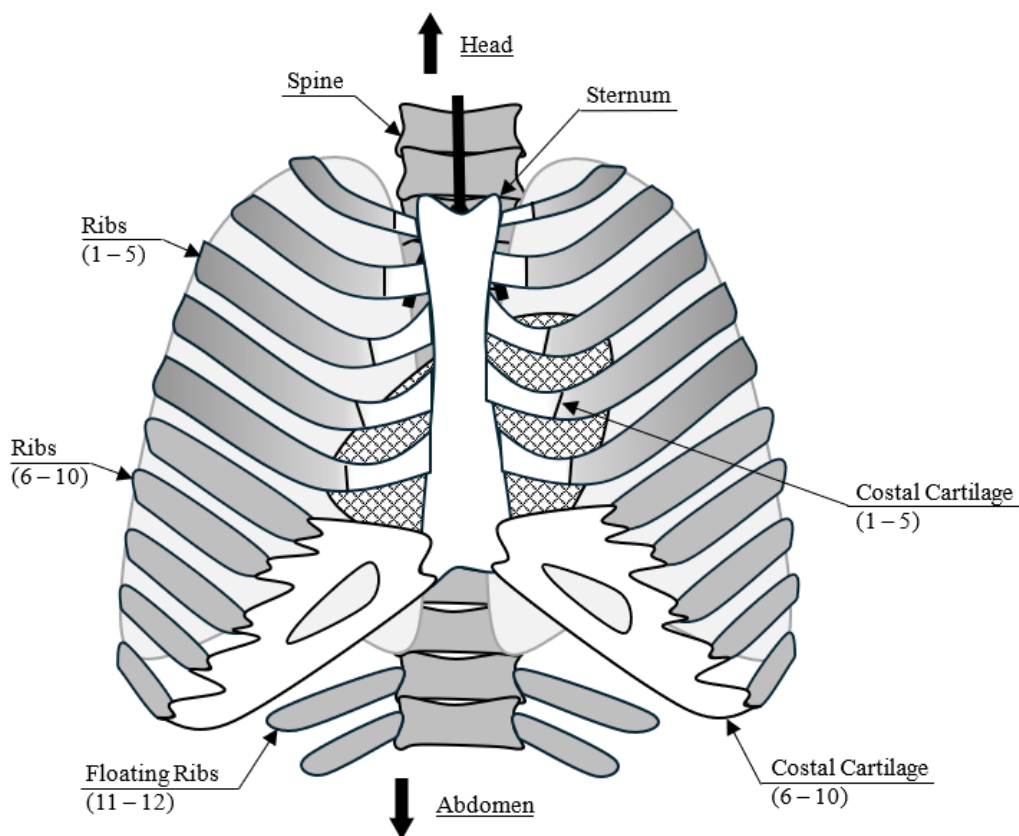
Figure 6: Diagram of approximate anatomy of the human ribcage with labels for the most significant features. Ribs connect to the sternum and spine via cartilage. See figure 7 for more details on the structures which the ribcage encloses, and figure 8 for CT images of these structures.

13
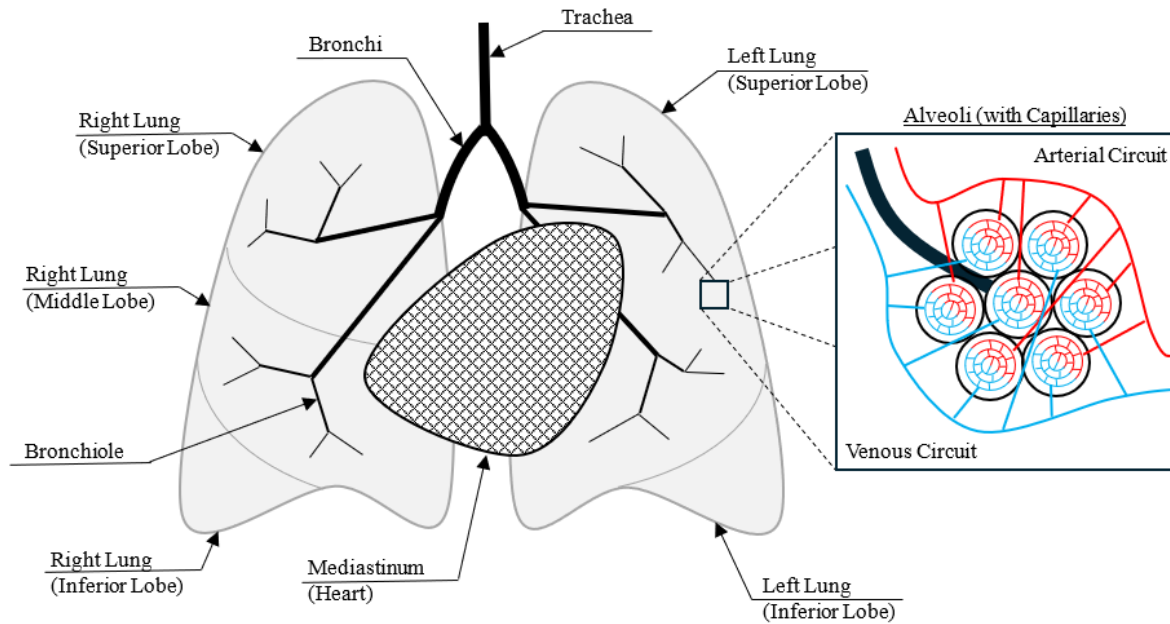
Figure 7: Diagram of approximate anatomy of the human lungs with labels for the most significant features. Bronchioles terminate in alveoli, miniscule sacs of air with a thin membrane. It is here that gas exchange occurs between the lungs and cardiovascular circuits via capillaries on the surface of the alveoli. See figure 6 for anatomy of the surrounding ribcage, and figure 8 for CT images of these structures.

The trachea connects the lungs to the mouth and nose, serving as a transport pipe for gases into and out of the body. The key function of the lungs is to extract oxygen from the air for use in the body. To do this air is inhaled through the trachea which bifurcates into bronchi. From this initial bifurcation, the bronchi lead to either the left or right lung on either side of the mediastinum. Each bronchus further bifurcates into smaller and smaller airways. When the structure becomes sufficiently small that they no longer have cartilage support, they are referred to as bronchioles [4, 6, 13, 28].

It is also worth noting that the structure of the right and left lungs is different. The heart is larger on the left side, which leads to the left lung having only two lobes, while the right lung has three. A lobe is a subdivision of the lungs based on the second generation of bifurcation stemming from each initial bronchus (the first generation of bifurcation) [13].

Bronchioles terminate in alveoli, the parenchymal tissue of the lungs. Alveoli are air sacs which facilitate the gas transfer of oxygen and carbon dioxide across their membranous layers to the blood in surrounding capillaries, part of the cardiovascular system. Oxygenated blood is pumped around the body via arteries while veins transport the de-oxygenated blood back to the lungs. The heart acts as the pump whilst the pulmonary capillaries serve as exchange terminals connecting the arteries and veins [4, 6, 13, 28, 29]. Alveoli are approximately 200 - 300 microns in diameter and the tissues here are extremely thin and delicate, meaning they are theoretically easily ruptured [13, 29]. From the vital

function that the lungs provide, PBLI can be catastrophic for the body's ability to function and leads to mortality.

The lungs are encased by the ribcage, which provides structural strength to the thorax cavity and protection of its contents. The ribcage is formed of the spine, sternum, and rib bones in addition to cartilage which connects them together. The spine is a column of vertebrae at the rear of the ribcage whilst the sternum is a plate of bone positioned centrally at the front. Bone is constructed of a shell of hard cortical bone encompassing an interior of softer and more porous trabecular bone. The space between the ribs is bridged by intercostal, subcostal, and transversus muscle [4, 6, 13, 28, 29].

The interior of the ribcage and the exterior of the lungs are coated in membranes of pleural tissue. The space between these membranes is referred to as the pleural cavity which contains serous fluid that provides lubrication such that the membranes can slide across each other. This allows inspiration/expansion and exhalation/contraction of the lungs to facilitate breathing. External to the ribcage is the skin, a multi-layered organ that encompasses the human body. The skin is the surface through which blast loading is applied and unlike the parenchymal tissue of the lungs rarely sees rupture solely due to the primary mode of blast loading [4, 6, 13, 23, 28].

Whilst the physical consequences of PBLI and the ensuing symptoms are well-known, the exact mechanism by which injury is inflicted is not fully understood. The following sections of this chapter will seek to explain the observed effects of PBLI and the existing methods by which injury and likelihood of mortality are assessed.

2.2   Clinical Symptoms of Primary Blast Lung Injury

Primary blast loading does not necessarily lead to damage to external tissues, which means that there may be no outward symptoms of injury at the surface of the thorax. This was recounted anecdotally in the First World War in which soldiers would collapse when situated near a blast despite seemingly not being directly struck by any debris or fragments [1].

However, generic symptoms may be present that indicate PBLI has occurred including coughing, chest pain, haemoptysis (coughing up blood) and dyspnoea (laboured breathing)/apnoea (cessation of breathing). Symptoms may also manifest as bradycardia (reduced heart rate), myocardial infarction (heat attack), hypotension (low blood pressure), and ischemia (reduction in blood flow/supply of oxygen) [1, 3, 6, 12, 15]. The injury itself will likely only be observable through CT or MRI imaging of the lungs.

On a CT scan, healthy lungs comprised mostly of low-density air will appear as a dark (low intensity pixels) region whilst denser tissues will appear brighter (increased intensity pixels). CT operates via passing a narrow beam of x-rays across the body and recording the magnitude of the ray that

penetrates to the alternate side. Higher density tissues (such as bone) produce stronger attenuation of the rays to reduce the magnitude that reaches the sensor. Greater magnitude rays produce an increased electrical signal at the sensor which is converted to a pixel intensity for viewing purposes [30]. In a lung suffering from PBLI, the lungs will often appear as brighter coloured/higher intensity. This is due to the rupture of tissues causing the exchange of blood and air between the pulmonary and cardiovascular systems (i.e., CT imaging the presence of higher attenuation blood/tissue within a region expected to consist of low attenuation air) [1, 3].

The rupture of tissues leading to haemorrhaging is the foremost consequence of blast loading. This is caused by spallation, fragmentation of tissue from the first material into the second as a stress wave transfers across the boundary from high impedance to low impedance, and microscopic over-distension of the alveoli causing capillary rupture. Blood haemorrhages into the airways, simultaneously contributing to blood loss from the cardiovascular system and reducing the alveoli available to perform the necessary gas exchange process. Additionally, gas can be exchanged to the venous network which can result in a venous air embolism, impeding blood flow [1, 3, 6, 15].

Clinically, haemorrhaging and the corresponding increase in intensity of pixel values on the CT would be expected to be focused on the mediastinum. It is usually dubbed as a batwing pattern of injury in the coronal and transverse planes of the human body. It is hypothesised that this pattern of injury is due to the nature of wave reflection discussed in the previous chapter. The stiffer tissues of the mediastinum are expected to generate reflections that increase the stress in the surrounding tissues causing them to be the first to rupture. As already discussed, the delicate parenchymal tissue would be expected to rupture long before the structurally thicker and stronger tissues of the mediastinum [1]. Figure 8 contains CT image examples of a set of healthy lungs and a set of lungs from a PBLI victim.

The initial treatment for PBLI is often ventilation as the symptoms indicate the patient would be struggling to breath independently or suffering from a lack of oxygenation. This must be carefully managed, as enforcing air flow into the system may worsen the patients state by creating or exacerbating embolism formation or causing additional rupture of traumatic tissue [3].
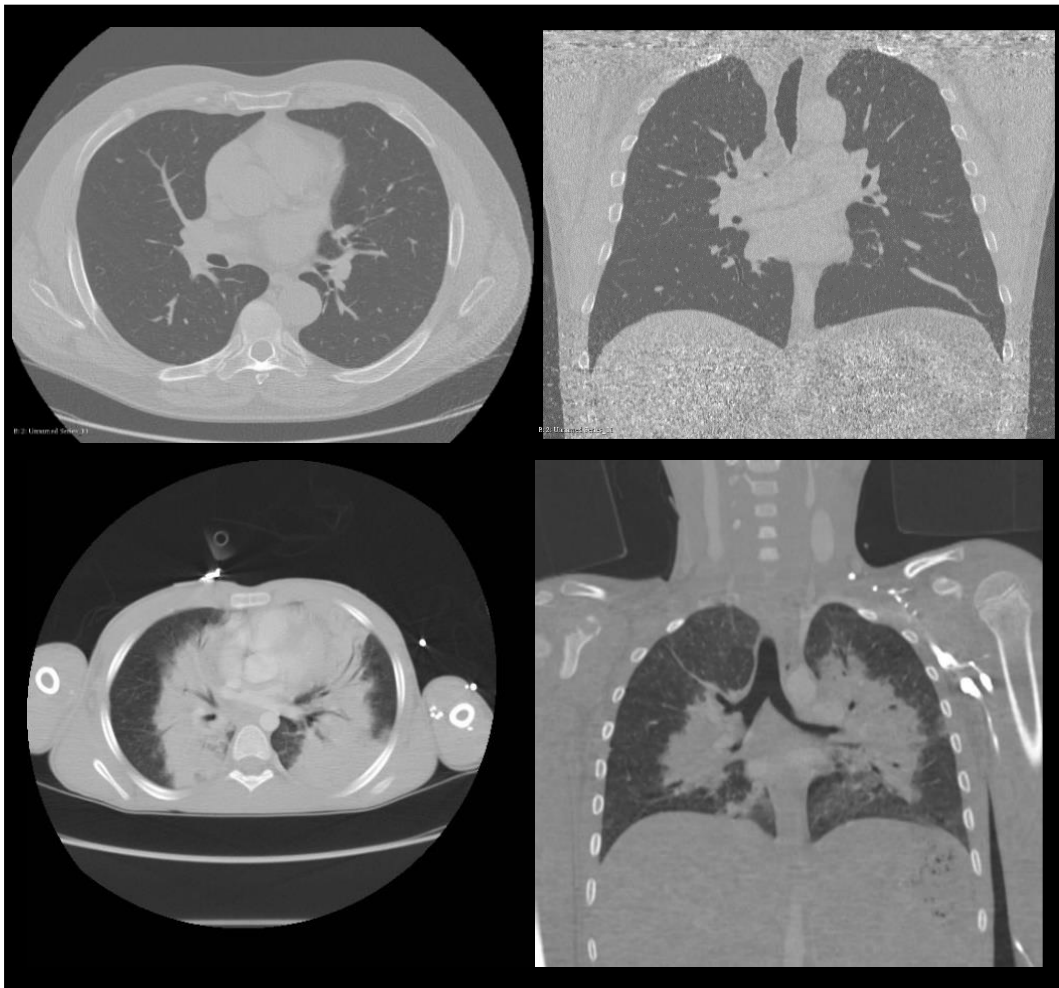
Figure 8: CT image of healthy lungs (top, provided by Cornell University's ELCAP Public Lung Image Database [31]) and CT image of a PBLI victim's lungs (bottom, provided by T. Scott [3]). Note the increased intensity of the pixels around the mediastinum in both the transverse (left) and coronal planes (right). This indicates a loss of lung function through parenchymal tissue rupture and macroscopic bleeding. The blast load that produced this injury pattern is unknown and cannot be predicted as it is from a real-world blast event.

2.3   Prediction Methodologies of Primary Blast Lung Injury

There have been several landmark studies attempting to produce a prediction of a victim's outcome when exposed to primary blast loading. The most well-known of these is the Bowen lethality curves created in the 1960's. This study focused on recording the outcomes of small mammals after blast testing and produced several curves representing levels of probability of mortality for varying blast loads. Figures 9 and 10 present the Bowen lethality curves [26, 32].
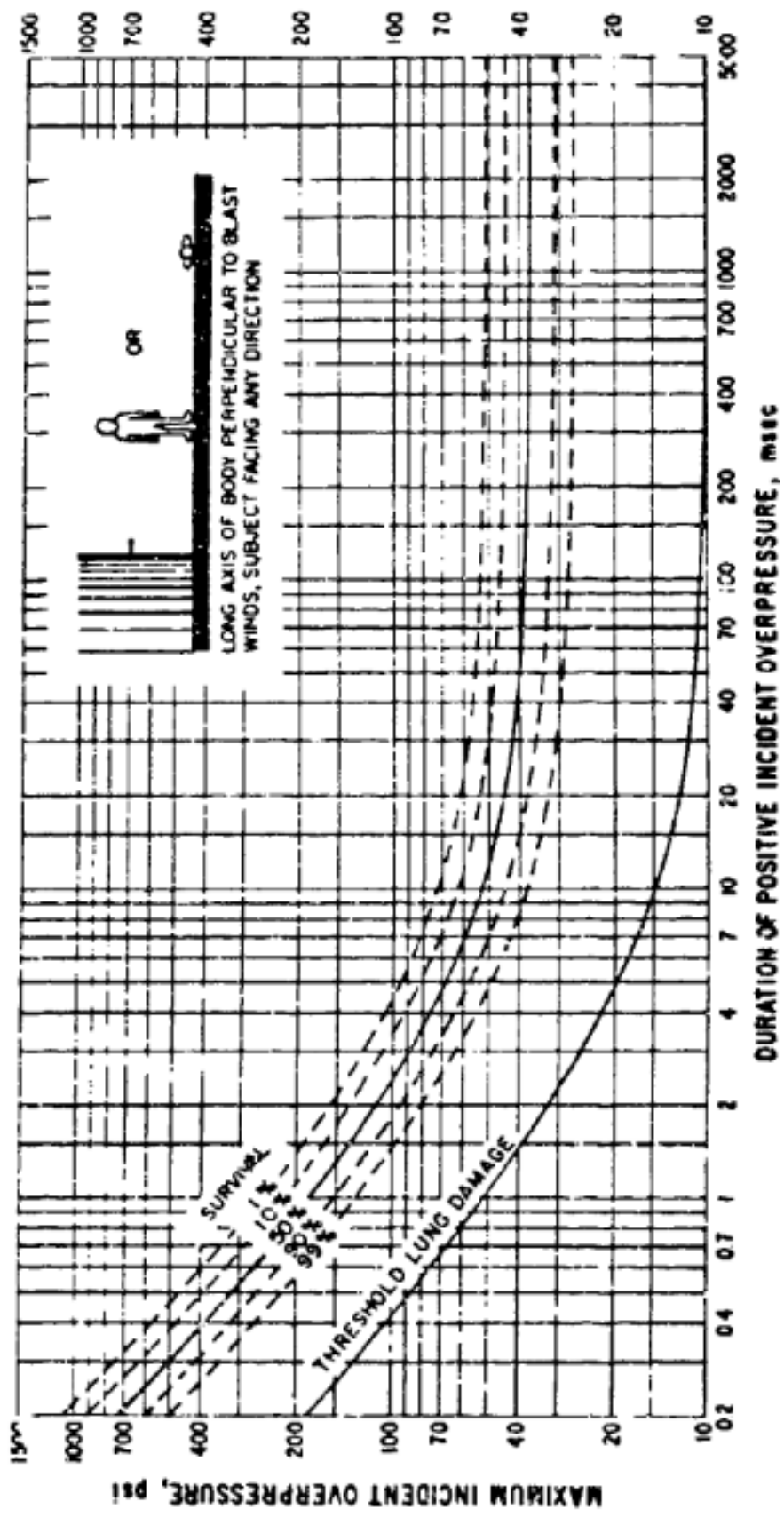
Figure 9: Bowen lethality curves for PBLI (produced in [32]). These curves are relevant to a scenario where the subject is in an open field (aside from the ground) in any orientation. These curves can be used to relate blast loads to injury severity. For example, a blast load with characteristics that would be plotted on or above one of the defined curves would correspond to a likelihood of survival as indicated by the label associated with that curve. Lethality curves are only applicable to idealised blast loading conditions (i.e., when Friedlander waveforms are applied as loading).

18
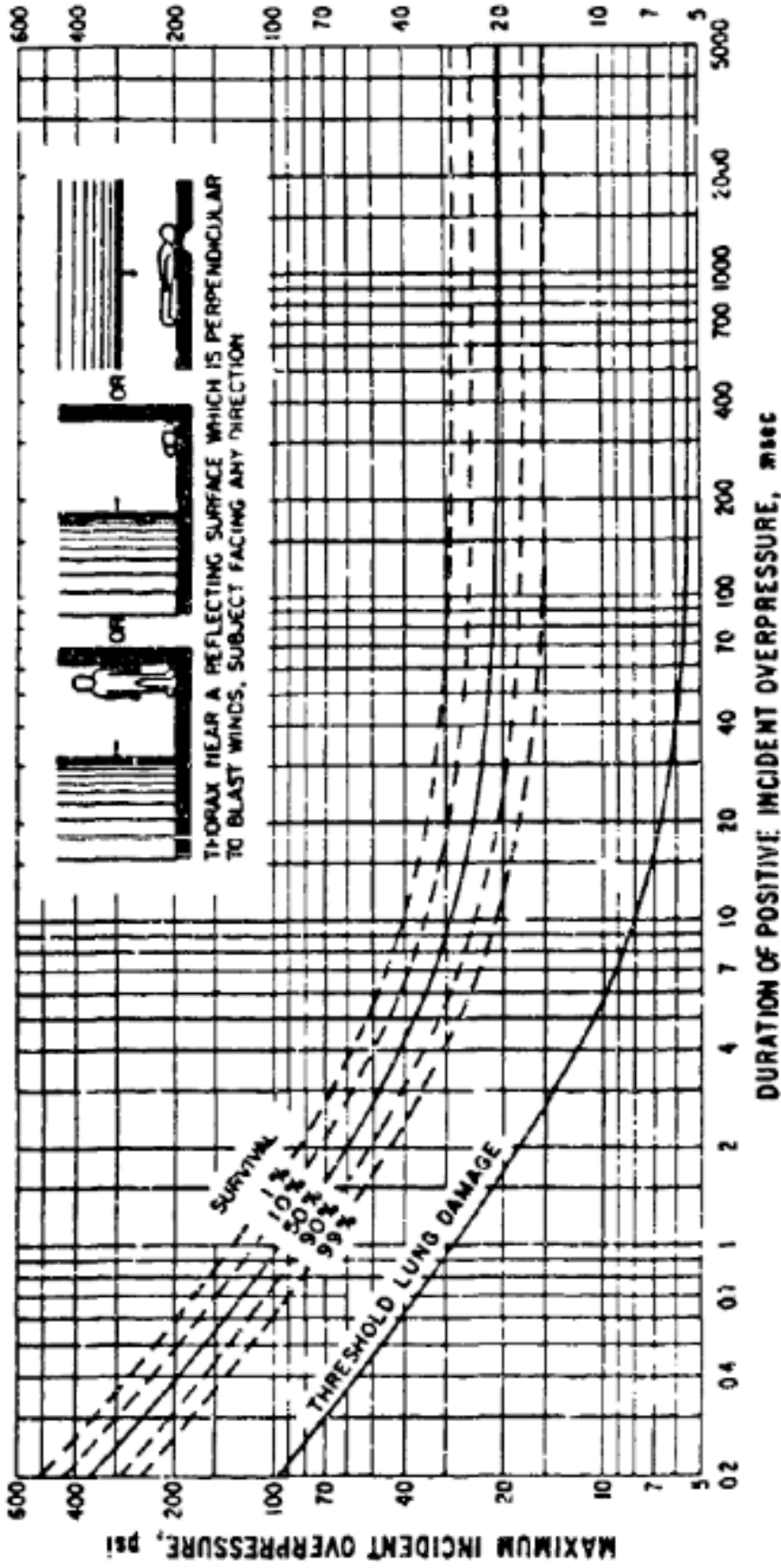
Figure 10: Bowen lethality curves for PBLI (produced in [32]). These curves are relevant to a scenario with a reflecting wall positioned behind the subject. These curves can be used to relate blast loads to injury severity. For example, a blast load with characteristics that would be plotted on or above one of the defined curves would correspond to a likelihood of survival as indicated by the label associated with that curve. Lethality curves are only applicable to idealised blast loading conditions (i.e., when Friedlander waveforms are applied as loading).

In the blast testing, subjects were exposed to blast loads from explosives suspended above the subject or shock tubes (specialised equipment that can produce an effective shock front through gas compression) directed at the thorax. They were resolved into three potential scenarios: an ideal environment in which the subject's longest axis is orientated parallel to the direction of blast propagation, an ideal environment in which the subject's longest axis is orientated perpendicular to the direction of blast propagation, or where the subject is in either orientation but with a wall positioned behind them (that will produce a reflection/confinement of the environment). From the trends observed in figures 9 and 10, with increasing surface area presented towards the blast there is increased likelihood of injury/mortality, and the presence of a confined environment further increases this probability. This is a logical conclusion as the increased surface area and confinement of the environment would certainly lead to a greater load acting on the subject [4, 6, 22, 32].

The injury curves can be used to estimate the probability of lethality for a victim experiencing a blast load of known magnitude and duration. A curve was also derived representing the threshold of injury, providing an estimate of a level below which PBLI would not be expected to be present at all. This serves as a basis through which protective systems can be designed to simply reduce the loading that reaches a subject [33].

In 2013, Bass updated the Bowen curves, particularly in the short duration regime where Bowen's results had been questioned, with modern and more robust data while making new assumptions about the orientation of the loading. The sample pool was extremely large at 2550 large animals with over 1100 of them designated as short duration (less than 30 millisecond duration according to Bass). Bass proposed that instead of a free-field and reflecting wall scenario, all scenarios would operate on the assumption that a reflecting wall was present. This provides a more conservative estimate of injury as it presumes the increased loading expected in a confined environment and can be argued to be more applicable to reality where open field scenarios are unlikely. The Bass lethality curves are shown in figure 11 overleaf [6, 26, 34].
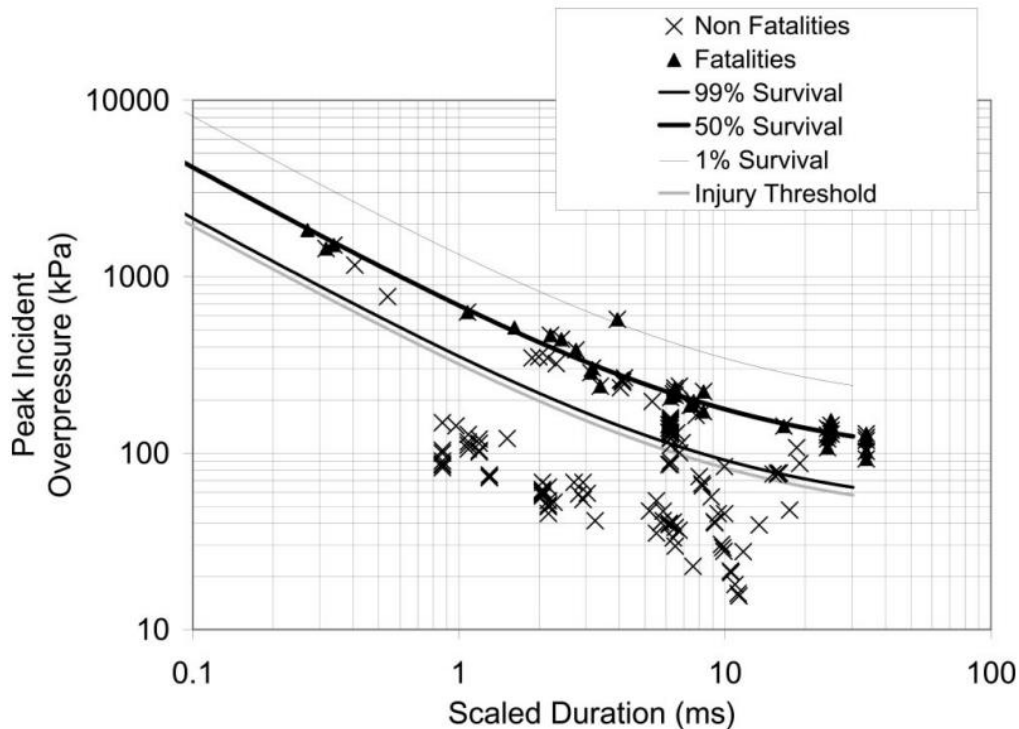
Figure 11: Bass lethality curves for PBLI with data points shown (produced in [34]). A single scenario is presented representing injury in all loading scenarios. These curves can be used to relate blast loads to injury severity. Bass' curves were derived as an intended improvement of the Bowen curves using increased experimental data. Lethality curves are only applicable to idealised blast loading conditions (i.e., when Friedlander waveforms are applied as loading).

The limitations of both generations of lethality curves are that they are only applicable for idealised Friedlander shaped blast histories (they cannot be used with complex blast histories with multiple peaks), and they offer no specificity or magnitude of injury. For example, any blast load greater than the threshold of injury curve would imply injury is present regardless of the subject's outcome, but there is no information on where that injury will occur, how extensive it will be, or how that injury manifested [26].

Another widely referenced study of PBLI is Axelsson's numerical model and accompanying blast test device (BTD) and Adjusted Severity of Injury Index (ASII) scoring system. The Axelsson numerical model is a more widely applicable method as it can be used with any blast load, but instead requires knowledge of the pressure history at four points around the circumference of a surrogate subject. Four pressure histories are recorded using Axelsson's specifically designed BTD, processed through the numerical model, and outputs are used to determine an ASII score representative of an extent of injury (culminating in >50% probability of lethality at the highest level) [6, 26, 35].

Axelsson's numerical model is a single degree of freedom (SDOF) lumped parameter model representing the thorax as four independent chest walls. The governing equation is a second order non-linear ordinary differential equation (ODE) which is solved for displacement and velocity of the

representative chest wall. All four chest walls are assumed to be equal but will experience different loading [6, 26, 35]. If it is assumed that one chest wall is facing the oncoming shock front and will experience a reflected pressure, then two are assumed to be parallel to the direction of blast propagation and will experience a static pressure, and the fourth is assumed to be at the rear of the subject and will experience a drag load. The static pressure load on each side of the thorax would be expected to be equal in an idealised environment, thus a minimum of three pressure histories are required to utilise the model. This theory is the basis of Weathervane's attempt to simulate the BTD using analytical predictions of blast loads and an assumed negligible drag load [6, 26, 35, 36]. Four sensors should be utilised in any realistic scenario where a sensor is not necessarily perpendicular to the direction of blast propagation and where reflections from the environment should be considered. The Axelsson BTD is shown in figure 12 below.
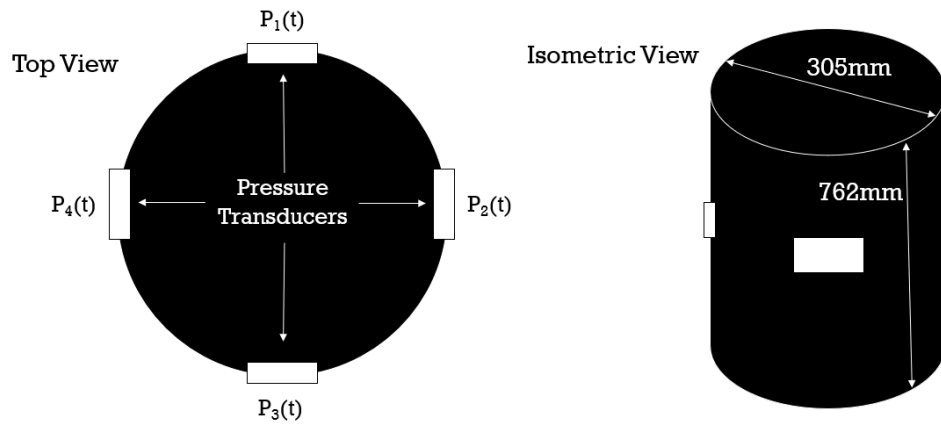
Figure 12: Diagram of the Axelsson's cylindrical BTD. Intended for experimental use, pressure transducers record four histories that are used independently in solving the Axelsson numerical model [26, 35].

A physical representation of the Axelsson numerical model is shown in figure 13. It is a Voight model of viscoelasticity, constructed of a spring and dashpot in parallel. The corresponding ODE is shown as equation 11 where M is the effective mass of the chest wall, J is the damping coefficient, K is the spring constant, x is the chest wall displacement, A is the effective area of the chest wall, $P_i(t)$ is the incident pressure at a specific time, P_0 is atmospheric pressure, and P_{lung} is the pressure within the lung. An expression for P_{lung} is given in equation 12, where V_0 is the initial lung volume and γ is the polytropic exponent (constant specific heat) for gas in the lungs. Values for each constant were derived from testing on small mammals and scaled for a 70kg mammal representing a human. Values are presented in table D [6, 26, 35].
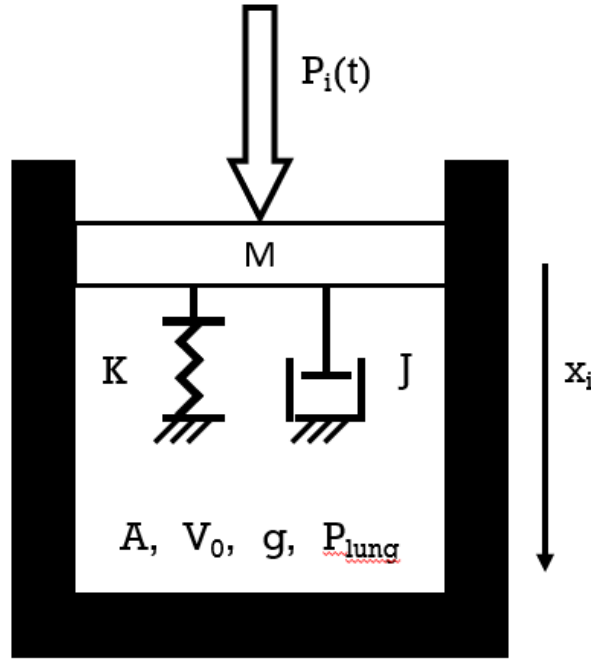
Figure 13: Physical representation of the Axelsson numerical model of a chest wall [26, 35] This model is comprised of a spring and dashpot component arranged in parallel. Each model represents one chest wall of four comprising a thorax. Each chest wall model acts independently.

$$M\frac{d^2x}{dt^2} + J\frac{dx}{dt} + Kx_i(t) = A\big[P_i(t) + P_0 - P_{lung}(t)\big] \qquad (11)$$

$$p_{lung}(t) = P_0\left(\frac{V_0}{V_0 - Ax_i(t)}\right)^g \qquad (12)$$

Table D – Axelsson Numerical Model Constants for 70kg Mammal

Parameter	Symbol	Value Scaled for 70kg Mammal
Effective Chest Wall Mass (kg)	M	2.03
Effective Chest Wall Surface Area (m^2)	A	0.082
Initial Lung Gas Volume (m^3)	V$_0$	0.00182
Damping Factor (Ns/m)	J	696
Spring Constant (N/m)	K	989
Polytropic Exponent for Gas in Lungs	g	1.2
Atmospheric Pressure (Pa)	P$_0$	101325

Solving the numerical model for each pressure history yields a velocity history for each chest wall. The average maximum velocity of each is used as the predictor of injury by calculating an ASII score using equation 13. The score categorises injury as trace, slight, moderate, severe, and greater than 50% probability of lethality, shown in table E. This method provides a direct link to the level of injury produced, but the terms used can be vague outside a clinician's expertise and significant overlap in the scores representing each injury level indicates a degree of uncertainty. For example, an ASII score of unity could fall within three different classifications in the form they are presented by Axelsson.

$$ASII\ Score\ = \left(0.124 + 0.117\left(\frac{\sum_{i=1}^{4} max\left(\frac{dx}{dt_i}\right)}{4}\right)\right)^{2.63} \tag{13}$$

Table E – Axelsson's Injury Prediction Using ASII Score

Average Maximum Chest Wall Velocity (m/s)	Adjusted Severity of Injury Index	Injury Prediction
0.0 – 3.6	0.0 – 0.2	No Injury
3.6 – 7.5	0.2 – 1.0	Trace to Slight
4.3 – 9.8	0.3 – 1.9	Slight to Moderate
7.5 – 16.9	1.0 – 7.1	Moderate to Extensive
> 12.8	> 3.6	> 50% Probability of Lethality

The ASII scoring system was created based on tests of mammals which were exposed to blasts and the corresponding injuries to the lungs, pharynx/larynx, trachea, gastrointestinal tract, and intra-abdominal region were scored according to a grading system in which the lungs and surrounding organs were assessed for location specific injury. The lungs were assessed for surface area extent of tissue discoloration due to bleeding, haemorrhaging, and hepatization. The ASII equation was fit to the experimental data to relate the peak inward chest velocity to the injury scoring system [35]. The scoring system used implies a similar probability of lethality can be achieved for singular locally concentrated injuries as numerous spatially diffuse patterns of damage, and that these patterns can manifest in varying regions in different magnitudes.

Like the Bowen/Bass lethality curves, this methodology does not provide specificity for the location of injury and does not provide a metric which can be used to directly correlate to lung tissue rupture (although the peak inward chest velocity does provide a good indicator of extent of injury).

Despite this, the Axelsson method is suitably robust and widely accepted such that it is used within the industrial sector for experimentally determining effectiveness of vehicular armour systems (as part

of the PAS300 standard [37]). This is another trait it shares with the Bowen lethality curves, which are at least anecdotally well-respected in the industrial sector and considered a good estimate for predicting the results of blast tests. Both methods are also frequently referenced by academic studies even in the modern day, and it is rare to encounter work on blast injury studies that is not grounded in the foundations they provide.

2.4 Simulated Prediction of Primary Blast Lung Injury

For investigating the lungs specifically, the most useful method is a finite element (FE) model. The seemingly earliest model was created by Stuhmiller, though it is rarely discussed in-depth in more recent studies. The most recent and comprehensive models were developed by Waterloo University's Greer (2006) [6] and Josey (2010) [13] on quasi-2D models of sheep and human thoraxes, and Yang's model of a rat (2019) [38]. Additional modern studies include effects of rotation of a human thorax and sheep thorax model on blast response [39], development of tools for assessing risk to crowds within urban spaces [22], and studies on more rigid materials [8, 40, 41] (including analysis of the combined effects of primary and secondary modes of loading [8]). Work focusing on specific detailed modelling of human lungs under blast loading is infrequent.

Stuhmiller is seemingly the first researcher to explore a finite element model of sheep thorax in 1986 42]. His material models were based on biological values adjusted to better represent results captured experimentally. His model ultimately produced results for intrathoracic pressure with strong agreement with the experimental data. Whilst it is stated that viscoelastic material models are used, exact parameters were not disclosed. A parametric study identified that the most crucial components were the density, bulk modulus, and shear modulus of the lungs (as opposed to the same parameters used for the ribs, muscle, or heart). It was concluded that the model was a vital step in proving that engineering modelling methodologies could be used to investigate blast injuries, yet further work on this model does not seem to have continued. Much of Stuhmiller's other work was instead focused on producing a similar injury model to Axelsson's using a concept of normalised work [43, 44]. This is also poorly publicised with errors noted in the original work that have been supposedly corrected or made superfluous by evolving the model to utilise a modified Lobdell model of the chest wall. This model is like the Axelsson model, describing the chest wall using spring and dashpot components. These corrections and their implementation have seemingly not been made public knowledge, being reported as private correspondence [44]. The focus of Stuhmiller's work seems to have shifted towards the Injury 8.1 software which utilises his more recent models to provide injury predictions from input loading histories [6].

The details of the Waterloo University FE models will be discussed in greater depth in future chapters (see chapter 5), but the key targets of Greer's and Josey's studies were successful in determining

stress predictions within the lungs for their various subjects including in the regions expected (confined geometry where reflections would be of the greatest magnitude).

Greer's study focused on the development of a comprehensive baseline model for investigating the pressure within the lungs and the effects of orientation. This work was revisited by Josey several years later. This model was compared with methods outlined by Bowen, Bass, Axelsson, and Stuhmiller's Injury 8.1 software for injury prediction in the development of a categorisation of injury focused on peak pressure within the lungs shown in table F. It should also be noted that the patterns of pressure magnitude were focused on boundaries (the surface of the lungs) and towards the front of the thorax where the heart model was located [1, 6, 13].

Table F – Greer Injury Predictions of Lung Tissue Damage

Injury Category	Lung Peak Dynamic Pressure (kPa)
No Injury	< 60
Trace	60 – 100
Slight	100 – 140
Moderate	140 – 240
Severe	> 240

The model developed at Waterloo University is referred to as a quasi-2D model as it is formed from a slice of a thorax two elements in height with computational symmetry conditions applied on the bounding transverse planes. The human geometry was taken from the Visible Human Project and modified to create a suitable ribcage model. Bone material properties were assigned to the upper elements and cartilage material properties were assigned to the lower elements, essentially collapsing the ribcage height variation into a 2D representation. Material properties were taken from literature with elastic models used for bone materials (cortical, trabecular, ribs, sternum, vertebrae, and costal cartilage), a rubber material model used for soft tissues (heart/blood, muscle, fat), and a Mie-Gruneisen equation of state model for the lungs. In-depth discussion of computational modelling methodologies will be discussed in chapter 4; however, it should be noted that this simulation used Arbitrary Eulerian Lagrangian (ALE) meshing to model the thorax and air simultaneously [6, 13].

A model very similar to Waterloo University's quasi-2D model is utilised in a study of rotational effects on likelihood of injury [39]. This study involved rotating an LS-DYNA based computational model of a human thorax and sheep thorax throughout 360 degrees whilst keeping the blast source stationary. As would be expected, this study found that the greatest injury was expected when the surface area presented towards the blast source was larger (i.e., to the front of the human thorax and

the side of the sheep thorax). It was conceded that the model was limited by being quasi-2D, but identified the angles of incidence which would result in the greatest likelihood of injury (60 degrees).

Whilst the most recent human thorax models are entirely computational, Yang's study on rats allowed for experimental data to be used to validate the accuracy of their own FE model. This study performed loading at several ranges using an identical blast threat to simulate different pressure magnitudes ranging from 635kPa to 109kPa peak reflected pressure. Lung surface pressures were extracted from the computational model, noting peaks ranging from 2kPa to 10kPa in regions of confinement (i.e., the apex of lung lobes, on surfaces near the mediastinum). Measurements were corroborated with autopsy of rats exposed to the same loading (10g of TNT), noting presence of tissue damage in the regions where peak pressures were observed in the subjects experiencing the greater blast loads (nearest offset positions), while correlation was weaker in the two furthest offset positions [38]. This highlights the ongoing need to understand the difference in response between short duration/near field loading and long duration/far field loading and relate it to probability of lethality.

Pope's Human Injury Predictor model differs from other models discussed in that it put more focus on the capturing of accurate blast loading histories in highly complex and enclosed environments [22]. Human bodies were modelled simply as cylinders within a much larger geometric space. The intention of this work was to develop a rapid model that could identify regions in an urban setting where blasts would be most dangerous. The model utilised predictions of injuries stemming from primary and secondary modes of injury, though opted to use simplified computationally efficient methods for injury determination. For primary mode of injuries this was based on empirically defined curves which defined the level of injury or a body part as an abbreviated injury score. The author discussed the possibility of integrating an Axelsson based SDOF model to be used in determining greater precision of injuries to specific body parts, but this model has not appeared in blast literature since, and it is unclear whether development on this model has continued. It is unknown whether it is being utilised in any research-based or commercial setting.

Other simulation works of note includes the work of Paolo del Linz et al. and their study of combined primary and secondary modes of damage to concrete [8]. This study's most important development was the investigation of both bast wave and fragment related damage which was investigated computationally and experimentally. The study used CONWEP defined bast loads applied to the surface and smooth particle hydrodynamic modelling of fragments to successfully replicate the damage observed in experimental testing for a specific explosive charge. It was found that the combined response led to greater overall damage than modelling of the individual contributions, and that the impacts provided the greatest contribution to the damage observed. It was also concluded that the impacts caused localised shock loading that increased the damage formed through action usually associated with primary blast loading. However, the author notes that further work is required to study

how the individual contributions to damage of each mode varies with ratio of loadings and varying loading magnitudes. The concept of this study is yet to be applied to injuries which would entail significant challenges due to the lack of well-established computational 3D models of injury for primary and secondary injury in isolation, the increased complexities related to loading of soft tissues compared to rigid structures, and the increased difficulty of attaining valid experimental data. The key result from this study in relation to injuries should be that the possibility that impacts can create localised shockwaves that can affect the primary loading dynamics and resulting damage.

2.5   Experimental Prediction of Primary Blast Lung Injury

Experimental testing of small mammals has been key to furthering understanding of injury mechanics and benchmarking most studies of PBLI modelling. This is most prevalent in the Bowen (1968), Bass (2013), Axelsson (1996), and Fung (1986) blast studies, however, research in this field continues primarily with the work of Johanna Boutillier et al. (2015-2021) who produce studies focussing on the blast testing of swine.

Fung's greatest contribution to the field was in characterisation of lung tissue under water jet loading. This was designed to mimic the high strain rate of blast/impact loading and findings focused on determining the physical and wave speed properties of the bulk organ with comparisons to theoretical estimations [45, 46]. Results indicated that wave-speeds associated with the lungs were on the order of tens of metres-per-second. More recent characterisation focuses on the smaller scale parenchyma specifically, such as in the work of Andrikakou et al [47]. Methods used in these studies are closer to typical characterisation techniques such as tensive and compressive loading of samples driven by uniaxial machines. The data from these studies will be discussed in much greater detail in chapter 4.

The experiments carried out by Johanna Boutilier et al. typically involve a charge suspended above a swine cadaver [5, 48-51]. This set-up is best related to the Bowen scenarios of loading as a body in an open field with a reflecting wall positioned behind it. These studies tend to focus on the recording of chest displacement, velocity, and acceleration using accelerometers attached to ribs to determine the viscous criterion (a measure of injury regularly used in automative crash studies) due to its relevance to high strain rate deformation. The swine are exposed to a variety of blast loads and injury risk level is discussed in terms of the peak pressure and impulse acting on the body. One study introduced a hydrophone mounted internally in the swine and presented injury predictions as intervals of pressure loading and chest wall velocity, much like Axelsson's model, but continued focusing on utilising the viscous criterion as a metric for injury prediction [50].

In addition to the testing of mammalian biological tissues, within the field there are several physical models that can be used as a surrogate of a human thorax, dubbed Anthropomorphic Test Devices (ATDs), one of which already discussed being the Axelsson BTD. This model has seen the greatest

attention by far, with other models such as Hybrid-III, WIAMAN, and MABIL featuring much less prominently in blast literature [26, 48, 52-55]. Unlike the BTD which primarily records pressure histories for numerical modelling, these latter models aim to capture the dynamics of the human thorax through replication of the constituent material behaviour. These models sacrifice the accuracy of biological responses in favour of ease-of-use, having fewer ethical ramifications, improved ability to run repeat/multiple tests, and no need to consider the transport and preservation of tissues that can easily become necrotic (compromising their physical properties).

The Hybrid-III model is colloquially known as a typical crash-test dummy and has been found to offer poor representation of the human thorax to blast loads [48, 52]. WIAMAN aims to provide a more accurate response of the human body for blast scenarios, with current focus on vertical loading such as from underside blasting of vehicles (e.g., from mines) [53-54]. Neither currently integrates specialised modelling of the lungs, making them generally unsuitable for PBLI studies. Early studies by Boutillier et. al also included rigid surrogates but these seem to have been replaced in favour of testing with biological tissues as discussed in the previous section [49].

Only MABIL was specifically designed for the study of PBLI and with the intention of replicating the motion of a human chest wall. It is constructed of a singular material, shore A70 (PU70) polyurethane. This means it does not have a material representative solely of the lungs and instead was designed to replicate the bulk response of the thorax. A study comparing the response of the MABIL chest wall velocity (experimental and computational values) to Bowen's lethality curves was inconclusive. Peak chest wall velocities recorded in testing and computational modelling were imprecise but produced consistent errors. However, comparison of short duration and long duration loading derived from Bowen predicted equal probability of lethality showed that the peak chest wall velocity of the MABIL ATD was not consistent and therefore not suitable as a metric for injury prediction in its current form. Final recommendations highlighted the need for further study of the model to resolve contradictory observations and fully establish whether the model can be successfully used for PBLI prediction [48, 55].

Except for the discussed studies, modern work on these ATD models is either unauthorised for public viewing or they have simply not been utilised in further research on PBLI. There are few publications discussing them besides the original presentations of the models or review articles discussing the modern state of blast testing. It is presumed that these models are either still works-in-progress or are not utilised in PBLI studies. This is not a surprise considering the breadth of the field of blast studies where modern blast related research can focus on TBI, alternative modes of injury (secondary, tertiary, etc.), post-injury care/treatment, injuries to specific groups (such as paediatrics), or other adjacent fields.

2.6 Prediction of Alternative Blast Related Injuries

In a limited exploration of these alternative fields of study, it was noted that the progress of each field is seemingly reminiscent of each other yet only tangentially cross-over. For example, Breeze et al. (and other researchers) have developed models for analytically predicting depth of penetration of fragment simulation projectiles (and establishing a threshold velocity for penetration) [56] whilst experimental work examines penetration into various tissues and surrogates [9, 10]. This is much like the path of progress of PBLI research shown by the Bowen and Axelsson models, experimental work of Fung and Johanna Boutillier, and the development of ATDs. Similarly, FE studies are carried out though tend to be focused on non-penetrating impacts [57-58], though some studies can be found on penetration into ballistic gelatine [59]. Diversifying this field from that of PBLI is the consideration of fragment motion (including yawing, tumbling, and fragmentation) and the cavitation of tissues (temporary and permanent) [7, 60]. These diversifying elements demonstrate the depth of understanding required to model both primary and secondary injury simultaneously and why there are seemingly no studies attempting it currently (besides the already discussed del Linz et. al study which examined a rigid target, removing the complexity introduced with soft biological tissues [8]).

A field very close to the study of PBLI is that of traumatic brain injury resulting from primary blast effects. Such studies include 3D finite element models, experimental studies of small mammals, and the development of ATDs [11, 61-64]. The FE studies are very similar to those discussed in previous sections, utilising the ALE methodology to model the shock front and the subject simultaneously, discussing the correlation of injury with peak pressure and impulse/duration, presenting 2D and 3D modelling, investigating stresses and strains within the model as threshold values for injury, and noting the effects of stress concentration at boundaries between soft and hard tissues. The injury mechanisms examined by these studies include cavitation of the cerebrospinal fluid [62, 64] and the acceleration of the head causing injurious collisions of the brain tissue with the harder skull [63]. All studies examined intercranial pressure as a metric of injury prediction.

An ATD model of a human head produced by Awad et al. underwent shock tube loading [61]. Analysis included discussion of the peak intercranial pressure, effects of orientation towards a blast source, the motion of the brain after loading, and comparison to experimental data from small mammal testing. These are all topics discussed in the FE studies, showing the ATD models the same phenomena. This highlights the lack of ATDs in the field of PBLI that can say the same with the only equivalent of MABIL being generally poorly explored, seemingly insufficient in its role of assessing chest wall dynamics, and offering no insight into internal stresses and strains (which are explored by both PBLI and brain injury studies). This specificity of design can also be seen in the WIAMAN model which offers little opportunity for PBLI study but has significantly more developed leg models for use in assessing injury due to vehicular underside loading (such as from mines) [54].

Finally, whilst many computational PBLI studies discuss the concept of being used in conjunction with personnel armour, no computational studies seem to have progressed this far. Despite this, studies are ongoing on how armour systems can mitigate (or possibly amplify) blast injuries such as in the work of Wood et al. who experimentally studied the attenuation of a shock tube produced load by various armours. This testing used a rigid thorax model and assessed the pressure recorded externally and internally by sensors mounted to the armour [33]. Such studies do not consider the thorax interaction with the armour and the vital ramifications of this (stress wave interactions at boundaries and the deflection of a chest wall) but do demonstrate the attenuation potential of an armour system.

2.7 Aims for Predicting Injury

Existing PBLI prediction methods have two key aspects which can be improved: the specificity of location of injury, and the metric indicating the presence of damaged tissue(s). Finite element models already provide a useful insight into the mechanical loading of lung tissue, but further study is required of which phenomena are most important to predicting injury, which parameters are greatest indicators of injury, whether injury mechanisms differ depending on the loading profiles, and improved methods for validating injury prediction metrics/thresholds.

To investigate these issues a 3D finite element model will be constructed of the human thorax accounting for the most significant tissues with the intention of assessing the internal mechanical behaviour through the internal stresses, strains, displacements, velocities, etc. with comparison to expected injury patterns and thresholds. This model will focus on capturing the wave propagation within the thorax with validation to be performed via comparison to existing studies, prediction of wave behaviour based on analytical methods, and experimentation using a custom designed physical model representative of the computational model. Whilst the purpose of the physical model is to validate the simulation work, it also represents a step towards development of a new ATD for PBLI. Analysis of results will also focus on the metrics used for predicting injury. This study hopes to provide a step towards a comprehensive simulation platform for optimisation of protection systems. It is expected that this investigation will contribute to knowledge of:

1) a parameter/metric by which lung tissue rupture can be expected.
2) the specific location of injury for prescribed loading conditions.
3) the effect that variations in loading produce on the prediction of location, magnitude, and the mechanisms of injury.
4) investigation of a method of experimental validation of internal loading of a model to corroborate estimates of mechanical magnitudes (i.e., peak stresses) used as indicators of injury.

3. Computational Modelling of Blast Propagation

3.1   Simulation Strategies for Blast Propagation

To fully capture all dynamics of blast propagation, a comprehensive platform for injury prediction should be able to produce an accurate loading profile acting on a subject. This should be based on a known threat, adjust the loading to account for environmental factors such as reflections, and adjust the loading to account for clearing due to the subject's geometry. To produce accurate loading, the shock front modelled should decay with increasing offset from the charge considering suitable decay characteristics. For more information on loading characteristics, see section 1.4 in chapter one.

Simulation of FE models has been used to achieve this in existing studies. The most complex models, such Greer's, Josey's, and Yang's incorporate a fluid domain for modelling blast wave propagation and a solid domain representing a subject to be loaded or environmental objects [6, 13, 38]. In these cases, the solid domain is a thorax model (human, sheep, or rat). Simplified models focus on accurate modelling of one part of these comprehensive simulations. For example, the blast wave can be simulated with results passed to a separate injury model, such as in Pope's study of injuries in a complex environment [22] or Teland's investigation of single point methods [36]. Alternatively, surface loading representative of blast loading can be applied directly to a subject model (such as Lahiri's loading of sandwich panels using CONWEP [18]). For an overview of these studies refer to chapter 2. Using fluid and solid domains together requires the use of specific meshing methodologies (i.e., either Arbitrary Lagrangian-Eulerian (ALE) or Coupled Eulerian Lagrangian (CEL)) and the modelling of fluid-surface interactions.

The subject model behaviour under the load is implemented using material models capable of capturing the necessary physics. A model is required for each distinct material of the subject. Modelling of biological tissues will be discussed in greater depth in chapter 4. Structural subjects and environmental objects that are expected to undergo negligible deformation in this study will be modelled using a Johnson-Cook plasticity model of steel [65, 66]. The parameters for this model are included in table G. This material model is utilised in studies of blast loading of steel plates [65]. Blasts that inflict injury are expected to be of significantly lower magnitudes than those that damage structures, therefore this material model should also serve as a suitable approximate for infinite rigidity.

Finite element packages commonly used for blast simulations include Ansys, LS-Dyna, and Abaqus. Of these packages, Abaqus was selected due to familiarity with the software, readily available access to the CONWEP methodology in the form of a built-in surface loading tool, potential to implement

custom material behaviour models, and a robust library of existing material behaviour models (with a high degree of customisability). Abaqus also utilises a powerful contact tool that can identify contact surfaces and apply prescribed contact conditions with ease. Within Abaqus, the Explicit Dynamics solver is used because a blast event features high magnitude and rapidly changing pressures and stresses that can only be captured with a high sampling rate characteristic of the small timesteps used in explicit solvers.

Table G – Parameters for Material Model of Steel [65, 66]

Parameter	Symbol	Value
Density (kg/m³)	ρ	7976
Elastic Modulus (GPa)	E	161
Poisson Ratio	υ	0.35
Johnson Cook Plasticity Parameters	A_{cook}	400E6
	B_{cook}	1500E6
	n_{cook}	0.4
	m_{cook}	1.2
Melting Temperature (K)	$Temp_{melt}$	1800
Reference Temperature (K)	$Temp_{ref}$	283
Johnson Cook Rate Dependent Parameters	C_{cook}	0.045
	$d\varepsilon/dt$	0.001
Expansion Coefficient	C_{exp}	445
Reference Temperature (K)	$Temp_{ref}$	273

The approach to simulation adopted for the studies contained in this thesis was to utilise the CONWEP methodology as a benchmark for producing accurate blast loading using a CEL model. This will be discussed in the following sections, with chapter 4 focusing on the development of a computational human thorax subject model to be loaded.

3.2   CONWEP Loading Implemented in Abaqus CAE

Abaqus CAE has a built-in tool included for easy use of the CONWEP methodology for blast loading. This tool operates via definition of a charge weight, definition of a burst type (air or ground), definition of an origin location for the detonation, and selection of a surface on which the load will act. A Friedlander profile load is calculated using the Kingery-Bulmash data to be applied to the surface following equations 14 and 15 (below and overleaf respectively) [18, 20, 67].

$$p_{CONWEP}(t) = p_s(t)[1 + cos\theta - 2\cos^2\theta] + p_r(t)\cos^2\theta \quad for\ cos\theta \geq 0 \qquad (14)$$

$$p_{CONWEP}(t) = p_s(t) \quad for \; cos\theta < 0 \qquad (15)$$

In equations 14 and 15 p_{CONWEP} is the pressure history applied to the surface, p_s is the static pressure history, p_r is the reflected pressure history, and θ is the angle of incidence. Static and reflected pressure histories are determined from the Kingery-Bulmash data.

This methodology does not require a fluid domain for the blast wave to propagate in, the load is directly applied to the surface. This means only material models and a meshed geometry of a subject is required to set up the simulation. CONWEP has several limitations that prevent it modelling several key aspects of blast loading. It can only apply loads to surfaces that are at an angle between perpendicular and parallel to the direction of blast propagation (i.e., cannot apply drag loads to the rear of a subject). The loading produced only accounts for two idealised scenarios of loading, spherical and hemi-spherical expansion of a shock front in an open field. This also means that it does not account for reflections from any surface, including environmental objects and the subject itself. Additionally, CONWEP does not account for the clearing phenomenon, instead assuming all surfaces are infinite. This means that CONWEP does not have the necessary functionality for providing the blast loading in this study, but it can be used as a comparison to blast loads produced using a more comprehensive method such as the CEL methodology [20, 67].

3.3   CEL Simulation in Abaqus CAE

Existing FE studies utilise a combination of fluid and structural domains to capture the entire process of blast wave propagation and loading of a subject. This methodology can include multiple subjects (of interest for loading or as environmental objects that will generate reflections) and account for pressure clearing.

A Eulerian domain refers to a mesh which remains stationery and material flow through it is calculated. A Lagrangian mesh is fixed to a material associated with it and deforms with the material. Eulerian meshes are used to model fluids expected to undergo large deflections, while Lagrangian meshes are used to model solids which are expected to experience smaller deflections. Eulerian elements retain their dimensions for the duration of the simulation while Lagrangian element dimensions can be reduced or expanded (i.e., deformed). The time step must be sufficiently small to maintain stable calculation over the entire simulation accounting for such deformation. A sufficient time step can be calculated using the Courant-Friedrichs-Lewy condition shown in equation 16 where Δt is the time step and Δx is the shortest element length in the mesh [6, 20, 67].

$$c \frac{\Delta t}{\Delta x} \leq 1 \qquad\qquad (16)$$

There are two methods by which these meshes can be utilised together Arbitrary Lagrangian Eulerian (ALE) and Coupled Eulerian Lagrangian (CEL). The ALE method uses a single mesh with individual elements assigned their behaviour (fluid or solid) and corresponding properties. At a boundary between materials, there needs to be a step in which the mesh is recalculated and adjusted to account for the deformation of the Lagrangian mesh. The CEL method is constructed from independent meshes that overlap. The advantage of the CEL method is that it can account for larger deflections and transportation of a subject, but difficulty is obtained in determining the precise boundary between the fluid and solid materials [6, 20, 67].

In the CEL method, interaction between meshes is handled by contact conditions between the materials. The surface of the Lagrangian domain is defined as the surface of the mesh, but the surfaces of materials in the Eulerian domain must be defined in Abaqus using the volume ratio tool. This tool calculates a ratio for every element of the Eulerian mesh representative of the volume that is not overlapped by a Lagrangian mesh. This is used to define the presence of a material within the Eulerian mesh. For example, a value of 1 would indicate that the element is entirely filled with a specified material, while a value of 0 implies the element is comprised of a material model representing a vacuum defined by Abaqus. For elements with an intermediate ratio, Abaqus defines a material model for that element representative of a combination of the stiffness of the user-defined material model and its own vacuum material model [6, 20, 67]. Within Abaqus, the air can be modelled with an ideal gas equation of state model. Parameters for this material model are contained in table H below [13, 20, 68]. The volume ratio tool creates a discrete field that can be applied with the air material model to the Eulerian domain using a prescribed field initial condition.

Table H – Ideal Gas Material Model for Air

Parameter	Symbol	Value
Density	ρ	1.29
Gas Constant	R_{gas}	287.05
Atmospheric Pressure	P_0	101325
Viscosity	μ	1.725E-5
Isochoric Specific Heat	C_p	716.7

The contact conditions define the behaviour at the boundary between materials. In Abaqus, contact between surfaces can be designated using the general contact algorithm which automatically detects surfaces to apply user-prescribed conditions. For this study, contact was defined as frictionless and

'hard' contact. Frictionless tangential behaviour allows surfaces to slide freely, whilst the 'hard' normal behaviour prevents overclosure of nodes through a penalty method. Alternative to the general contact function, surfaces can be defined with specific contact conditions applied between them. This method must be used when defining a contact algorithm that prevents separation between surfaces. The no separation condition is only applied between the air and external surfaces of a Lagrangian model [20, 67].

To capture the expansion of the shock front, the air domain is modelled as a wedge with symmetry boundary conditions applied normal to all 4 planar sides in a spherical coordinate system (circumferential directions). The concave and convex faces are both defined as a non-reflecting Eulerian inlet and outlet, allowing material to enter and leave the system through these faces. This process should prevent reflections being generated at these faces; however, this was not observed to be the case as some reflections did propagate back into the domain. This phenomenon was noted by Dassault too and remains unexplained [20]. This effect is not unexpected as numerical implementations of boundary conditions can have imperfections where small amplitude reflections are generated. It is difficult to investigate the cause of these reflections further as Abaqus as a commercial software does not provide direct access to the exact form of the solver. It would be expected to take the form of a Neumann boundary condition. As reflections from any edge of the domain is a concern, the wedge must be sufficiently large to prevent reflections propagating back to the model within the timeframe of interest. All boundary conditions are defined in spherical coordinates.

Additionally, initial conditions must be set for the temperature (273K) and initial gauge pressure (0Pa). These are both defined using the predefined field function in Abaqus CAE for the initialisation timestep. An illustrated summary of the initial and boundary conditions of the Eulerian domain for the CEL simulation can be found in figure 14.

A velocity history in the form of tabulated data is applied to the concave face as a boundary condition to initiate the blast wave. This can be done using a pressure history instead, however Dassualt concluded in their assessment of this workflow that a velocity boundary condition should be more stable [20]. To generate an inflow velocity history, a blast load expected to form injury is required. Table I overleaf contains data taken from the Bass injury curves to represent specific injuries at a short duration (2ms) and long duration (10ms). These two points are taken as they are representative of different regimes where impulse and peak pressure are respectively expected to dominate the injury prediction metric [34].

Using the Kingery-Bulmash data conversion discussed in chapter 1 and equation 9, a TNT charge weight and offset position are generated representative of this loading. From this data the short duration can be seen to be equivalent to a subject in the near field while the long duration is achieved in the far field. This is how this study will refer to these two regimes with wedges created in

Solidworks representative of the two regimes (0.5m - 3.5m and 8.5m – 14.5m). The angles of the wedges are determined by the distance of the edges from the thorax model within it. In all cases it was ensured that at least three times the height of the thorax model was provided across the plane where the thorax would be placed.

To acquire the boundary condition needed to produce these loads, the Kingery-Bulmash methodology was used to produce a prediction of peak static pressure at a known inlet position (0.5m or 8.5m) and converted to a Friedlander pressure history using equations 9 and 3. This can be adjusted to a particle velocity history for use in the simulation using the relationship shown in equations 1 and 2.

Entire Part Volume
- Initial Temperature of 273K
- Initial Stress of 0kPa in All Directions
- Assignment of Material Model(s) to All Elements

Wedge Inlet Face
- Free Eulerian Inflow
- Non-Reflecting Eulerian Outflow
- Tabular Ampliude Velocity History
(Defined in Spherical Coordinates)

Wedge Side Faces
- Symmetry Normal to Respective Faces
(Defined in Spherical Coordinates)

Wedge Outlet Face
- Free Eulerian Inflow
- Non-Reflecting Eulerian Outflow

Figure 14: Summary of boundary conditions used for the Eulerian domain of the CEL simulation for blast propagation.

Table I – Blast Loads Representative of Injury Levels Derived from Bass Lethality Curves

Bass Lethality Probability (%)	Static Pressure (kPa)	Duration (ms)	Reflected Pressure (kPa)	Equivalent Air Blast TNT Charge Weight (kg)	Equivalent Air Blast Offset Distance (m)
99	350	10	1385	212.58	9.21
50	180	10	584	143.11	10.84
1	95	10	260	59.20	10.87
Threshold	85	10	227	53.52	11.08
99	800	2	4088	1.32	1.18
50	410	2	1704	1.67	1.71
1	220	2	757	1.43	2.14
Threshold	200	2	669	1.31	2.16

3.4   Analytical Validation of Simulated Blast Loading

The CEL simulation was run for various uniform mesh sizes and biasing was introduced to allow for more computationally efficient meshes for loads at the threshold of injury in the near and far field. Biasing of the mesh is vital for large models as the air domain must fully encompass the model and allow clearance around the model to prevent unwanted reflections being generated at the edges of the domain and propagating back to the subject model. The threshold of injury is used as the reference for loading as this is the injury level of greatest interest for identifying and exploring the mechanism by which injury is inflicted.

Additionally, data was recorded in Abaqus using the in-built CONWEP tool. For more information on this tool refer to section 3.2. Cubic elements of 1mm element length were defined in space at 1m intervals from an origin covering the same spatial region as the CEL simulations. The origin was defined as the source of detonation and the size of TNT charge was defined in kg based on the same Kingery-Bulmash data as the CEL simulation (see table I). The elements were assigned the steel material model shown in table G (which made them effectively rigid). The surfaces from which stress would be extracted were set parallel to the direction of blast propagation to record static pressure histories.

The purpose of the CONWEP simulations is to further verify the CEL simulation accuracy/precision. The CONWEP methodology is well established and the Abaqus implementation is assumed to be suitable. Static pressure was assessed for both spatial and temporal decay (figures 15 and 16). Figure 17 shows a visualisation of the pressure propagating in the CEL method air domain.

Results show that mesh insensitivity is achieved at element lengths greater than 3.175mm and that ensuring a fine mesh in regions of interest is required for accurate modelling of the pressure history. The fine elements are necessary for capturing the near instantaneous rise to peak pressure associated with the arrival of the shock front. Coarse elements of 100mm can be used in regions where only blast propagation occurs while finer elements of 3.175mm can be used around the subject and at the inlet (to insure accurate initiation of the shock front). As expected, the near field shows greater variability as this is a region associated with much less stability and poorly formed shock fronts where ideal gas behaviour may not be suitable. Nonetheless, negligible variation is still found at 3.175mm element length. Agreement with CONWEP measurements assures the methodology is operating correctly.
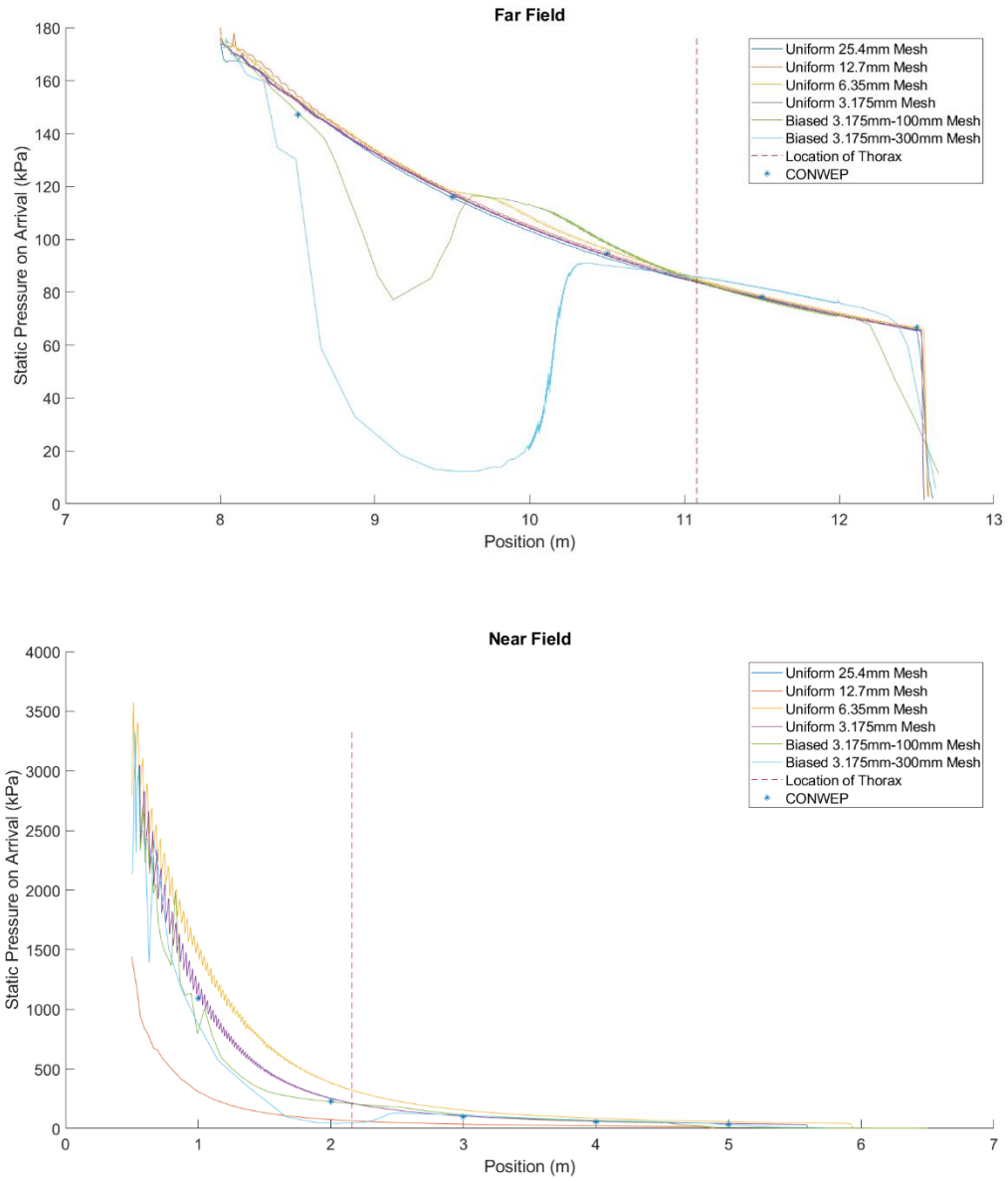
Figure 15: Spatial decay of static pressure for the far field (above) and near field (below) data sets with varying mesh sizes. CONWEP data is shown as data points which represent a benchmark. Grading the meshes allows for improved computational efficiency whilst maintaining accurate pressure measurements within a region of interest.
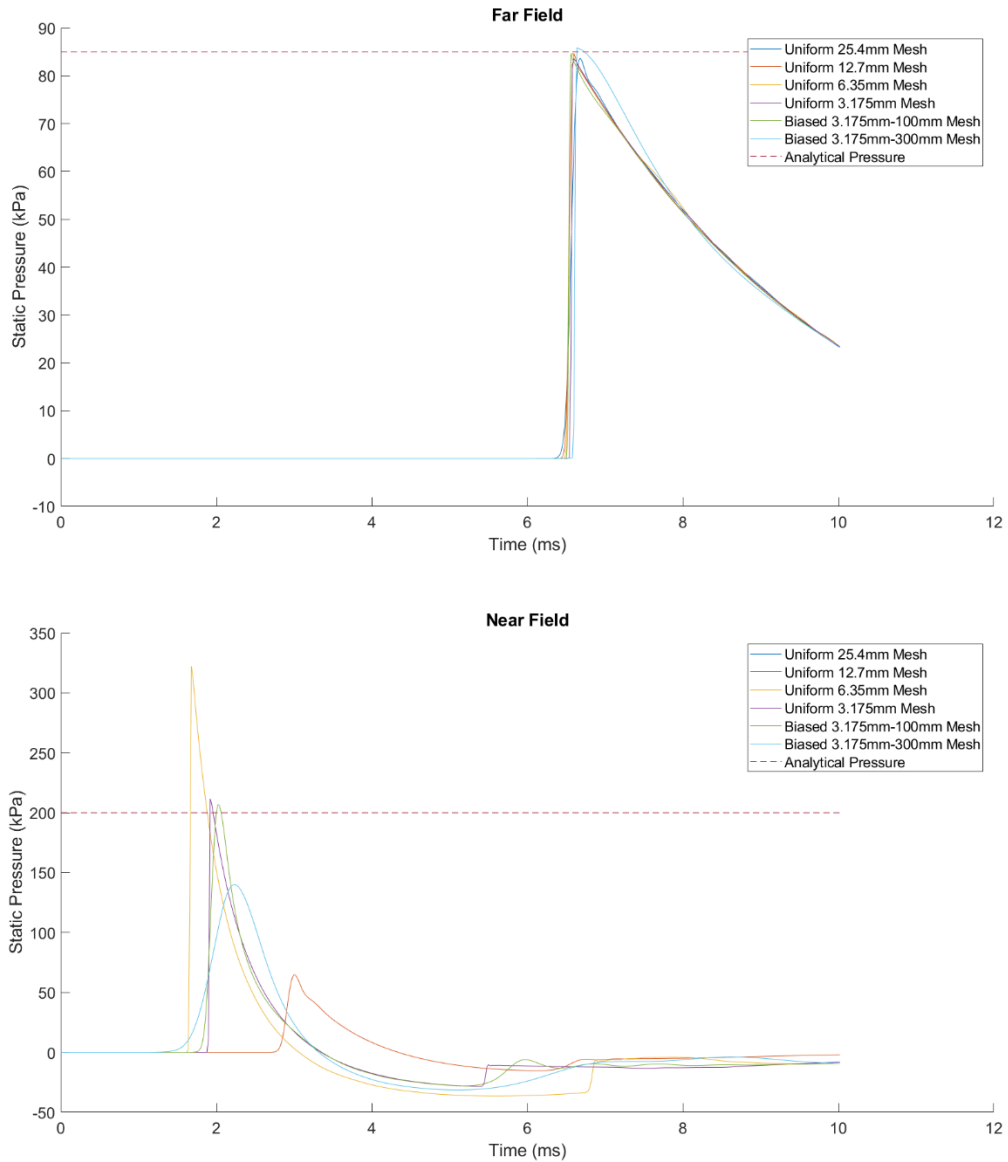
Figure 16: Temporal decay of static pressure for the far field (above) and near field (below) data sets with varying mesh sizes. Analytical pressure is the targeted static pressure representing a benchmark. It is important to capture both the rapid rise time and the corresponding decay. Grading the meshes allows for improved computational efficiency whilst maintaining accurate pressure measurements within a region of interest.
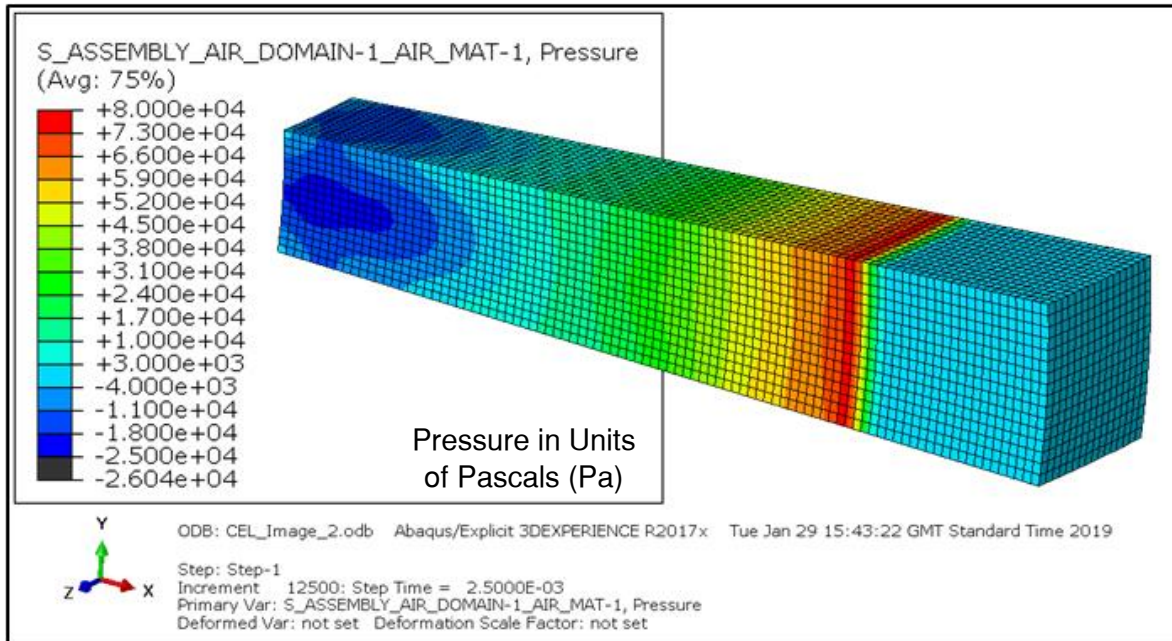
Figure 17: Example image of simulated blast wave propagating in the Eulerian domain of a CEL simulation. Example wedge domain shown is significantly smaller than the domains used in full simulations. The contours are formed from the "Pressure" output variable in Abaqus CAE for Eulerian elements in units of Pascals, however, values presented here are illustrative only. When extracting data for analysis, the nodes along the centreline of wedges were utilised.

4. Computational Model of the Human Thorax

4.1 Thorax Model Segmentation

A 3D geometry of the human thorax is required to create a FE model. An anatomically accurate model can be acquired via segmentation of CT images, a process by which voxels are assigned labels to associate them with a mask which can be reconstructed as a volumetric object.

CT images of the human thorax were acquired from the ELCAP Public Lung Image Database hosted by Cornell University [31]. This is a database of open-source CT images readily available for use in research. Selection of the CT series to use for modelling was based on the clarity of the image (including the visibility of different tissues) and measurements of average expected tissue thicknesses found in the literature. The key aspects identified were the ribcage sagittal and coronal plane diameters, the chest wall thickness (distance from the external surface of the thorax to the lungs), and the diameter of the ribs. These provide information on the chest size and the expected geometry of the most important structures of the thorax.

Anatomical measurement selection aimed to be as close to an average human male as possible. The decision to focus on male geometries was due to clinical CTs of blast injured lungs available for validation purposes being male. The methodology presented here can be replicated to create a general geometry for any demographic or highly personalised models as required. The purpose for this study is to establish mechanisms of wave propagation for which a generalised male geometry will suffice.

Chest wall thickness was expected between 42.79mm and 34.33mm based on needle thoracostomy studies with an average of approximately 40.8mm [69, 70]. Ribcage dimensions were checked against the averages found by Abrams et al [71] and Bellemare et al [72]. Abram's study showed how rib diameter can vary by location and orientation. It was assumed that approximately 9.42mm would be representative of a suitable diameter for the ribs (the mean of the reported heights and widths of ribs). Bellemare found that the average male ribcage would have a sagittal plane diameter of approximately 104.6mm/m and a coronal plane diameter of approximately 152.6mm/m, both normalised by height. Average height was taken as 1710mm for a male from the same study, leading to respective diameters of 178.9mm and 260.9mm.

The most important structures in the thorax defined for this study were soft tissues, bones, and the lungs. This was based on the acoustic impedances of these tissues as similar acoustic impedances implies there will be minor boundary interactions while the more significant differences imply greater reflective behaviour. This selection follows the same convention as Yang's rat model [38]. Typical ranges of acoustic impedances in the thorax can be found in table J based on ultrasound

measurements. Ultrasound involves recording the flight time of ultrasonic waves passed into a body by a probe which detects the returning reflected waves. This type of loading has a high frequency (MHz range) and low amplitude; therefore, such data may not be representative of the high amplitude single pulse loading which is present in blast loading. These values alone were deemed insufficient and so several FE studies which present material models, particularly those used for high loading rate studies, were used to calculate additional data points using equation 4 and shown in table K.

Table J – Reported Acoustic Impedances of Human Thorax Tissues

Material	Acoustic Impedances (MRayl)				
Skin	1.99 [73]	1.71 – 1.83 [74]	1.53 – 1.68 [75]		
Bone	5.32 / 7.75 [73]	6.47 [76]	5.3 [77]	3.75 – 7.38 [78]	3.2 – 7.4 [75]
Fat	1.38 [73]	1.33 [76]	0.138 [75]	1.35 [78]	
Lung	0.17 – 1.4 [79]	0.26 [78]			
Muscle	1.68 / 1.69 [73]	1.65 – 1.74 [75]	1.65 – 1.74 [78]		
Air	0.00043 [76]	0.00043 [77]	0.000429 [75]		
Water	1.48 [73]	1.48 [75]	1.48 [76]		
Soft Tissue	1.5 [77]	1.42 – 1.66 [74]			
Heart	1.64 [73]				
Blood	1.66 [73]	1.67 [76]	1.62 [75]	1.62 [78]	

A comparison of the reported and calculated values shows strong agreement. As would be expected, the high water-content of the softer tissues such as the skin, blood, heart, fat, and muscles lead to very similar impedances. These are lumped together as soft tissues, comprising the skin and connecting tissues within the thorax. The bones are shown to have significantly higher acoustic impedance due to their increased stiffness. The variation in value is also greater, however all are consistently several times larger than soft tissue acoustic impedances. The organ with the greatest variability is the lungs,

with values ranging from near identical to soft tissues down to values nearing the magnitude of air acoustic impedance. This variation is possibly due to the inflation level of the lungs, as shown in Oelze's analysis [79]. This summary is logical as the lung parenchyma would be expected to behave as a general soft tissue if examined in isolation, with the air content providing the property change causing reflections.

Table K – Calculated Acoustic Impedances of Human Thorax Tissues

Material	Source	Density (kg/m^3)	Wave Speed (m/s)	Acoustic Impedance (MRayl)
Bone	[6]	1762	2360	4.158
	[77]	1650	3200	5.280
	[78]	1380 – 1810	4080	5.630 – 7.385
Rib	[6]	1561	3073	4.797
Sternum	[6]	1354	2248	3.044
Vertebrae	[6]	1644	3282	5.396
Cortical Bone	[6]	1907	3730	7.113
Cancellous Bone	[6]	1216	971	1.181
Costal Cartilage	[6]	1281	286	0.366
Fat	[79]	952	1450	1.380
	[78]	920	1450	1.334
Lung	[6]	200	30.1	0.00602
	[78]	400	650	0.260
Muscle	[79]	1060	1550	1.643
	[78]	1070	1584	1.695
Air	[77]	1.29	330	0.000426
Water	[79]	1000	1500	1.500
	[78]	1000	1480	1.480
Soft Tissue	[6]	1000	1500	1.500
	[77]	1000	1540	1.540
Heart	[6]	1030 - 1100	1540 - 1580	1.586 – 1.738
Blood	[6]	1040	1560	1.622
	[78]	1060	1570	1.664
	[80]	998	1480	1.477

For segmentation of the model, several software packages are available including Avizo, Mimics, and 3DSlicer. Most of these software packages share similar segmentation tools so 3DSlicer was selected for segmentation purposes due to ready availability and familiarity with the software.

Thresholding can be applied to differentiate tissues and create masks/segments based on the pixel intensity of the CT images. This can then be adjusted using a suite of tools including smoothing functions, closing/opening functions, Boolean operations, and manual edits. Figure 18 shows the 3DSlicer interface along with an example of the thorax model created.
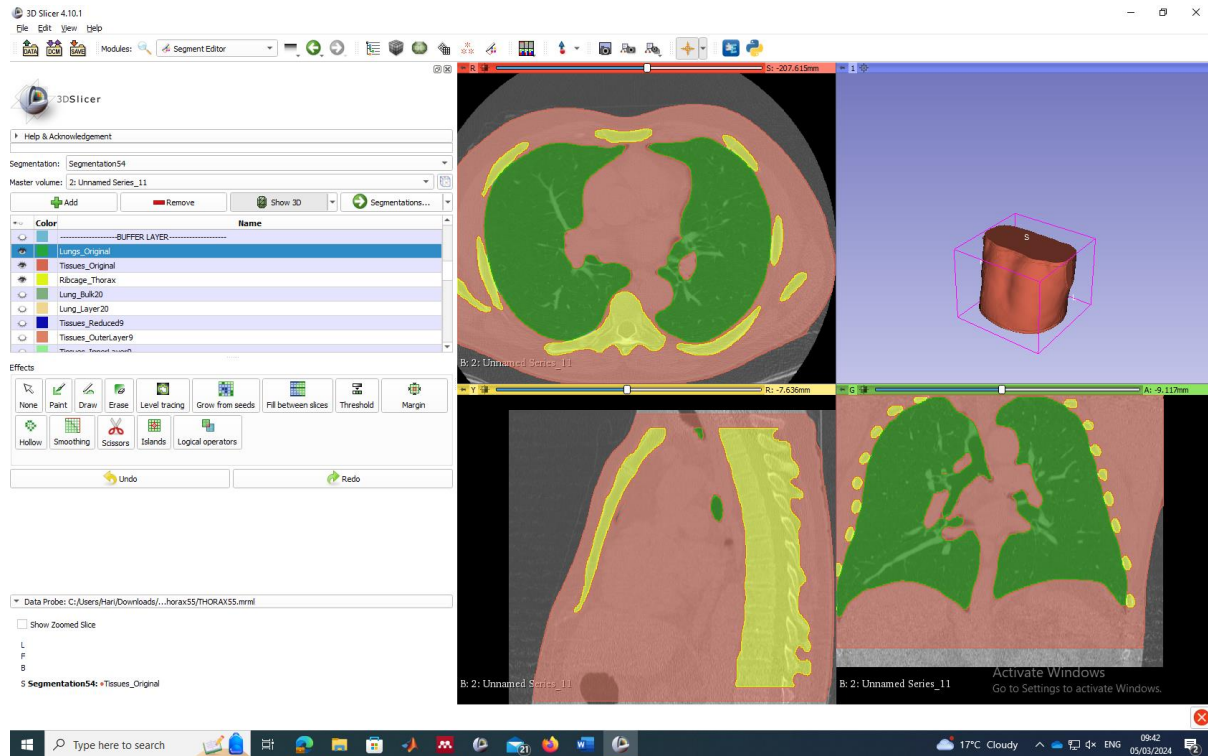
Figure 18: Screenshot of the 3DSlicer interface for segmentation and the thorax model generated. Various models were created and explored however the only one utilised fully was a significantly smoothed model comprised of four masks: external air, lung, bone, and soft tissues.

Thresholding was used to create three initial masks sequentially, bone/ribcage (highest intensity), soft tissue (medium intensity), and lung (lowest intensity). When creating the lung mask, the external air was also captured. Whilst the masks had some poorly defined boundaries at this point (i.e., significant scattering of soft tissue existing within the lungs and ribcage), the boundary between the external surface of the thorax and air was very well defined. Therefore, because the mask was divided into two unconnected geometries, the "Island" tool (which identifies regions that are disconnected) could be used to separate the external air into a fourth mask (alongside the use of Boolean operations). This is an important step for use of another tool, "Grow from Seeds."

Larger airways within the lungs and some regions of cartilage (i.e., around the sternum or spine) were captured as soft tissues. In the interest of increasing the uniformity of the geometry and removing thin features that would be computationally expensive to model, these regions were manually adjusted using the "Erase" (removes pixels from a mask manually) and "Paint" tools (adds pixels to a mask manually) to replace them with lung/bone masking. Whilst this improved the definition of the masks, further refinement was required.

45

The "Smoothing" tool includes algorithms for performing fine adjustments based on the assignment of neighbouring pixels. For example, "closing" can be used to fill openings in a mask based on a user determined kernel size, whilst "opening" will do the opposite and remove small extrusions. A mask can also be "Grown from Seeds" with other masks used as boundary conditions. For example, one mask can have its boundaries smoothed using the "opening" tool (or the Median or Gaussian smoothing functions), and the masks bounding it can be grown to fill the void(s) created. It was important to have the external air modelled as a mask to use this tool to prevent growth of a mask into this well-defined region. The "opening" tool can also be used to remove isolated pixels created during the thresholding stage.

This process of smoothing was iterated on the selected CT series along with Boolean operations and manual "Paint" tool edits until a suitable thorax geometry was acquired and exported as a surface geometry file (.stl) for meshing. The thorax was deemed suitable for export when there were no fine/sharp features visible and boundaries between the masks were judged to be consistent smooth contours without compromising the original anatomical shape of the tissues (i.e., no pixel was left unassigned to a mask, no mask shared pixels, no significant deviations were observable from the initial thresholding, and no features less than 3 pixels in width were observable). The only significant change that was required was to create a layer of soft tissue at the neck and abdomen to ensure the internal organs were fully encapsulated and would not be directly exposed to air during the blast simulations/testing.

Various additional models were created using the smoothing functions and Boolean operators to create a quasi-2D slice model (mimicking the Waterloo University model [6,13]), interstitial layers between masks for creating graded meshes, and additional masks separating the spine, sternum, and cartilage. These were ultimately not required.

4.2   Thorax Model Meshing

To use the model in a FE simulation, it must be re-meshed. This process was performed in Materialise 3-Matic, a software package for meshing of geometry that can output a mesh optimised for use in Abaqus. The initial surface mesh is defined by the size of the voxels used in the segmentation stage, but these increments are far too small for use in an FE study where number of elements and element size defines the potential efficiency and accuracy of the simulation. A re-meshing step was performed on the surface of the geometry to achieve the desired element size. This surface mesh was then converted to a volumetric mesh comprised of first order tetrahedral elements using the same sizing limitations. Maximum element length was set as 3.175mm, with allowance for refinement to preserve small features/sharp contours. This is necessary to prevent significant overclosure of nodes between the individual meshes (soft tissues, ribcage, and lungs) which were processed separately.

An element size target of 3.175mm was set for the model to match the elements used in the Eulerian domain. This should promote stable and accurate function of the contact condition as it minimises discontinuities. Following the two-step process outlined, 3-Matic successfully produced a surface mesh and then a volumetric mesh with minimal variation in element length (<1mm) from this target. Elements and their corresponding nodes created in this process were output into an Abaqus optimised input file which can be directly imported into Abaqus CAE. Each mesh was created separately so nodes are not placed consistently, and minor overlap of parts is expected. This is resolved in the pre-processing stage of an Abaqus analysis which resolves overclosures by applying nodal forces to reduce/remove the overclosure prior to running the solver. Any unresolved overclosures are reported as warnings. Figure 19 below shows the individual meshes imported into Abaqus CAE. Overall dimensions of the model produced were approximately 410mm in width, 308mm in height, 187mm in depth at the top of the model, and 306mm in depth at the bottom of the model.
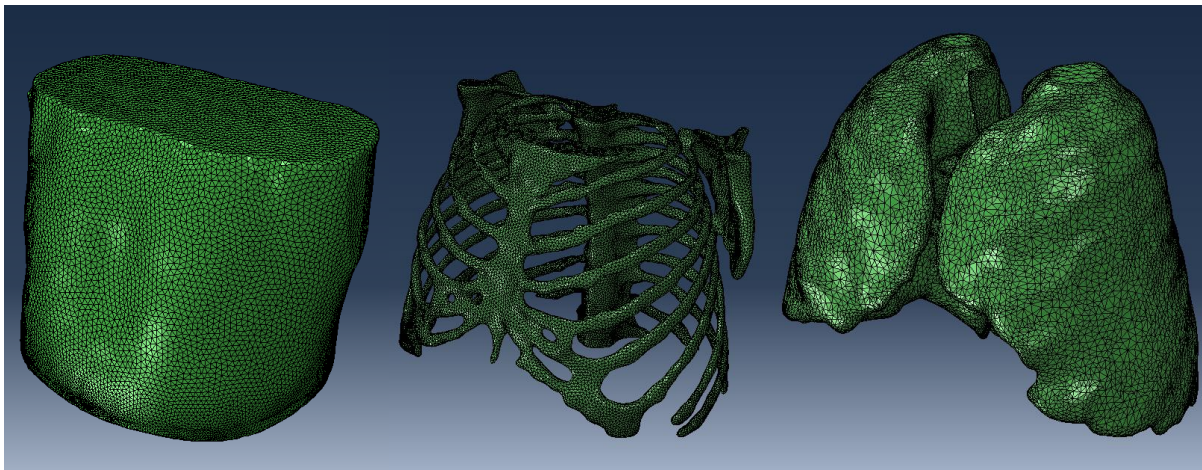
Figure 19: Screenshot of the thorax model meshes imported into Abaqus CAE. Each mesh was created individually so nodes do not align between models, however, target tetrahedral element size is consistent (3.175mm) with minimal variation (<1mm). Any overlap between models is resolved in a pre-processing step in Abaqus CAE which removes overclosures but applying small forces to move nodes towards the boundary between models. Excessive overclosures cannot be resolved and would require either re-meshing of the model or increased smoothing during segmentation. This step was not required.

4.3   Material Modelling of Soft Tissues for Blast Loading

Biological tissues are often described as anisotropic, exhibiting stress-strain relationships dependent on the direction of loading. This is due to the alignment of constituent fibres creating increased tensile/compressive strength in the fibre axial direction. Despite this, when considering bulk tissues macroscopically (i.e., at the organ level) it is appropriate to assume isotropic behaviour as it is assumed the varying orientations of microscopic behaviour is averaged over larger distances [82, 83]. For this study all materials will be treated as homogeneous solids behaving isotopically. It has been acknowledged that biological materials have local differences in properties however this study focuses on macroscopic observations.

Biological tissues are often described as behaving as hyperelastic and/or viscoelastic materials. Hyperelastic materials are defined as materials that undergo non-linear elastic deformation which can be modelled based on a strain-energy function, while viscoelasticity is defined as a material that exhibits a loading rate dependent stress-strain relationship (either strain-hardening or strain-softening). The strain stiffening behaviour of hyperelastic behaviour is usually observed more strongly at large strains. In small strain regions elastic behaviour may be assumed to be applicable. Skin can be assumed to be deforming in the small strain region as damage to the skin is not expected to occur at the threshold of injury (strain < 25%) [84].

It could be assumed that the lung parenchymal tissue (specifically the alveoli) is sufficiently thin and delicate that a small strain will cause rupture, however, experimental evidence does not seem to support this. Studies of lung under compression and tensile testing have found that the tissue fails at strains greater than 60% [47]. It should be noted that these tests use relatively low strain rates of testing, samples are not constrained as they would be within the thorax, and samples do not necessarily represent the macroscopic behaviour of the entire organ. Although the high rate of loading experienced in blasts will cause an effective increase in elastic modulus (evident on stress-strain curves [47]), this is expected to only cause an increase in ultimate tensile stress, not on the strain associated with failure. This is evidenced by testing of muscles which found that strain rate variation had no effect on the strain associated with failure [85], with the same conclusion evident in a collection of skin testing results [47,113].

Despite this, at the threshold of injury, only the most egregious regions would be expected to exhibit injury inducing large strains with smaller strains exhibited more prominently. Furthermore, this study is focusing on investigating the wave propagation properties which occur significantly more rapidly than the global motion of loaded bodies (based on the associated wave-speeds of biological tissues). The mechanisms of alveoli overdistension and cavitation may not require strains that are this large due to the increased confinement of the tissue, the potential for air-filled cavity implosion, and the mechanism of spallation [3, 6, 13, 14].

For modelling viscous components of materials, a Maxwell, Voight (used in Axelsson's methodology), bespoke spring and dashpot configuration, or the Prony series are commonly used to define the stress-strain behaviour. Such testing remains a topic of contention with varying models proposed for specific studies under specific conditions/loads. Accurate data is difficult to determine and varies across the available literature as dynamic testing at high strain rates is difficult to complete, particularly as biological tissue properties are also sensitive to additional factors such as temperature and hydration. Furthermore, for this model the lungs are treated as a homogeneous solid, further limiting data available as studies often examine small samples of tissue representative of microscopic

behaviour as opposed to the bulk behaviour of organs. This assumption of isotropic behaviour has been experimentally evidenced in testing of porcine lung [83].

In blasts high strain rates are expected ($>100s^{-1}$) so viscous effects are surely in effect. However, due to the limitations of data available for modelling tissues as viscoelastic materials and the success of linear elastic material models used in Yang's study, the materials will be modelled as linear elastic homogeneous materials using data from dynamic and high strain rate testing where available.

The greatest wealth of data available is for the soft tissues with literature data available for numerous studies of mammalian tissue at varying load rates. The elastic model adopted in this study is heavily grounded in this literature data. Table L contains data from a comparison of tensile and indentation testing used to determine elastic modulus of soft tissues [86]. Yang's FE rat model uses the tensile testing value for muscle from this dataset to represent soft tissue [38].

Further data from FE models include one developed by Toyota Motor Company to assess organ injury in crash scenarios [87] uses elastic modulus values ranging from 1MPa to 100MPa. Notable specific values include for skin (31.5 MPa), Aorta (4 MPa), intercostal muscle (1 MPa), mediastinum (13.5 MPa), and ligaments (9 – 100 MPa). These values are taken from the works of Shah [88], Yamada [89], Abe [90], and Lee and Yang [91] and are consistent with the tensile testing values shown in table L. This is further confirmed by elastic modulus values for biological tissues reported in Blast Injury and Science Engineering. These include ligaments in tension at low strain rates (0.01/s, 40MPa) and high strain rates (130/s, 77MPa), cartilage in compression at low strain rates (0.005/s, 2.5MPa) and high strain rates (1000/s, 25MPa), trachea in high strain rate compression (6000/s, 10.6MPa), and skin in low strain rate compression (<0.01/s, 0.3-1MPa) [4].

Table L – Summary of Tensile vs. Indentation Soft Tissue Testing (replicated from McKee et al [86])

Soft Tissue Investigated	Indentation Elastic Modulus (MPa)	Tensile Testing Elastic Modulus (MPa)
Skin	0.085	30.0
Liver / Kidney	0.190	10.0
Spinal Cord / Grey Matter	0.003	2.0
Muscle	0.007	480.0
Tendon	N/A	560.0
Breast Tissue	0.008	N/A
Artery / Vein	0.125	2.0
Sclera	N/A	2.7
Cornea	0.029	3.0

It has already been expressed how soft tissues have high water content which leads to a density close to water (1000kg/m³), as shown by the values reported in table K. It should also be noted that a common assumption of biological tissues is that they behave as incompressible solids and therefore have a Poisson's ratio approaching 0.5 (as no realistic material will be perfectly incompressible). Definition of the Poisson's ratio is also relative to the expected speed of sound. Pressure waves in a material will propagate in all directions as longitudinal and shear waves. Calculation of the wave speed is dependent on the density, elastic modulus, and confinement of the medium. In an effectively infinite material, longitudinal propagation of a pressure wave is described as the dilatational wave speed which is defined by equation 17. In this configuration, the confinement of an infinite domain prevents lateral deformation leading to an effectively greater elastic modulus and thus a greater wave propagation speed. For a laterally finite material, the wave is free to expand/contract laterally. This reduces the wave speed calculation to the typical expression shown in equation 18. Dilatational wave speed is the expression utilised within Abaqus CAE according to the documentation [67].

$$c_d = \sqrt{\frac{E(1-v)}{(1+v)(1-2v)\rho}} \qquad (17)$$

$$c = \sqrt{\frac{E}{\rho}} \qquad (18)$$

In equations 17 and 18 c_d is the dilatational wave speed, c is the speed of sound in the material (referred to as the thin-wire wave speed), E is the elastic modulus, and v is Poisson's ratio.

Soft tissue elastic modulus was set as 30MPa based on a tensile testing value for skin [86], the value used for skin in Toyota's FE model [87], and similarity to various other reported values [84, 86]. Skin is used as a reference as it is the interface through which the blast wave will enter the body and so its properties are used to define the transmissivity at this interface. This elastic modulus value is much higher than typically reported values for low strain rate testing, but the viscous effects are expected to effectively stiffen the tissue during blast loading. An upper limit can be predicted using the classical expression of wave-speed (equation 18). Taking the known density of 1000kg/m³ and the expected wave speed of 1500m/s, elastic modulus under these conditions is implied to be 2250MPa. The closest value identified to this in the literature was 480MPa in tensile testing of muscle. Instead, 1500m/s was taken as a target dilatational wave speed, 30MPa was set as the elastic modulus, and Poisson's ratio was calculated and rounded to suitable significant figures. Poisson's ratio was set as 0.4978 (near incompressible) such that the dilatational wave speed is equal to 1512m/s.

For this study, the structure of bones has been equated to a foam core composite panel, with porous trabecular bone acting as the foam and the cortical bone acting as the solid skin. A model for calculating an effective material model is shown in equations 19 and 20 while table M contains a summary of data for the constituent parts. This model of a foam core composite panel was taken from Blast and Ballistic Loading of Structures [92].

$$\rho_b = \rho_1 \varphi_1 + \rho_2 \varphi_2 \qquad (19)$$

$$E_b = \frac{2E_c r_c^3}{(2r_c + r_t)h^2} + \frac{E_t r_t^3}{(2r_c + r_t)h^2} + \frac{6E_c r_c (2r_c + r_t)}{h^2} \qquad (20)$$

In equations 19 and 20 ρ is the density, φ is the volume ratio of materials, r is the material thickness (transverse plane), h is rib height (coronal plane), and subscripts 1, 2, c, t, and b represent first, second, cortical, trabecular, and bulk material respectively. The first and second materials in this case is cortical and trabecular bone.

Table M – Summary of Literature Bone Properties

Source	Material Classification	Density (kg/m³)	Elastic Modulus (MPa)	Poisson's Ratio
[93]	Cortical (Rib)	2000	10000	0.3
	Trabecular (Rib)	1000	40	0.45
	Cortical (Vertebrae)	2500	11000	0.4
	Trabecular (Vertebrae)	1000	1000	0.3
	Cortical (Sternum)	2000	10000	0.3
	Trabecular (Sternum)	1000	40	0.45
[6]	Ribs	1561	7920	0.379
	Cortical	1907	15260	0.367
	Vertebrae	1644	9680	0.376
	Sternum	1354	3510	0.387
[87]	Cortical (Vertebrae)	2000	12000	0.3
	Trabecular (Vertebrae)	1000	1000	0.3
	Cortical (Sternum/Rib)	2000	9860	0.3
	Trabecular (Sternum/Rib)	1000	40	0.45
[11]	Cortical	1800 - 3000	15000	0.22
	Trabecular	1000 - 1750	560 - 4600	0.24
[94]	Cortical	1800 - 2000	17000	0.41

This model produced effective constants within the range expected within literature. A summary of literature values for bone density, elastic modulus, and Poisson's ratio can be found in table M. Most values have been used in computational models. The extracted parameters representing cortical and trabecular bone and the resulting calculated model used in this study are contained in table N.

Lungs have a highly porous structure of branching airways terminating in alveoli [28]. One such bulk acoustic model that accounts for this structure is application of bubbly water theory [95-97]. This is an effective medium model based on the compressibility of air and soft tissue. It predicts a significant decrease in wave speed through the medium due to the scattering of the waves. This aligns with measurements of simulated blast loading wave speeds in lungs by Fung who experimentally recorded wave speeds on the magnitude of tens of m/s in water jet loading representative of the of the loading experienced during blasts [45, 46]. Equation 19 is used to calculate the bulk density using material parameters for air and soft tissue. Equations 21, 22, and 23 describe the calculation of effective elastic modulus for the bulk lung material [95-97].

$$\frac{1}{K_p} = \frac{\dfrac{3v_p}{1 + v_p} + \dfrac{3(1 - 2v_p)}{1 + v_p}}{c_p^2 \rho_p} \qquad (21)$$

$$\frac{1}{K_b} = \varphi_a \left(\frac{1}{K_a}\right) + (1 - \varphi_a)\left(\frac{1}{K_p}\right) \qquad (22)$$

$$E = 3K(1 - 2v) \qquad (23)$$

In equations 21, 22, and 23 K is bulk modulus, φ is volume ratio of air to lung parenchyma, and subscript p refers to properties of lung parenchyma. A volume ratio of air can be calculated based on the inflation level of the lungs, parenchyma volume (843ml) [98], and maximum lung volume (5000ml) [99]. The density and Poisson's ratio of lung parenchyma is defined using the derived soft tissues material model. Wave speed in lung parenchyma is assumed to be equal to 1500m/s, equal to soft tissues. Adiabatic air bulk modulus is taken as 142kPa [23]. Poisson's ratio of bulk lung is taken from Yang et al [38] as 0.32.

The effective wave speed of 33m/s is similar to the values reported in Fung's testing which presented a range of 31.4 – 61.7 m/s for goats, 16.5 – 36.9 m/s for rabbits, and 25 – 70 m/s for horses dependent on inflation level [45, 46]. The effective density of the organ is also representative of values reported in the wider literature (between 200 and 720 kg/m³ [6, 80]). This results in an acoustic impedance that is within the wide range of reported values, tending towards a value close to air, which is consistent

with the difficulty encountered in ultrasound imaging of the lungs due to their air content. Lung model values are presented in table N below.

Table N - Biological Tissue Derived Material Models

Material	Density (kg/m^3)	Elastic Modulus (MPa)	Poisson's Ratio	Wave Speed (m/s)	Acoustic Impedance (MRayl)
Model Tissues	1000	30	0.4978	1512	1.512
Model Bone	1679	4679	0.361	2169	3.643
Model Lung	289.5	0.2156	0.32	33	0.009
Cortical Bone	2178	15000	N/A	N/A	N/A
Trabecular Bone	1433	2542	N/A	N/A	N/A

4.4   1D Wave Propagation Modelling

To assess the behaviour of 3D wave propagation throughout the thorax, the 1D wave equation was adapted into a MATLAB code for analysis of the interactions of waves at the boundaries. This investigation into 1D wave propagation is intended to inform expectations for the 3D simulations and evaluate the two approaches. This code was based on the work of Jason Carson at Swansea University who provided the first iteration of the code ready for minor modifications. This code was used as a teaching tool as part of Swansea University's Multivariable Calculus for Medical Engineers module [100]. Study of the waves in 1D is important to assess whether the 3D geometry is significant in determining the internal stresses in the lungs and is useful for validating that boundary interactions are behaving as expected.

The wave equation is shown in equation 24. In the MATLAB code, the wave equation is solved numerically using the implicit Galerkin method with second order backward difference in time.

$$\frac{\partial^2 u}{\partial x^2} = \frac{1}{c^2} \frac{\partial^2 u}{dt^2}$$

(24)

Elements defined along the 1D path have the same material properties defined in the previous section. This creates boundaries at which reflections can be generated and propagate back through the domain. The inlet behaviour is defined using a pressure history informed Neumann condition while the outlet condition is defined as a non-reflecting free end.

Simple simulations were run in Abaqus CAE using a series of sequential cube elements to create an effectively 1D simulation for comparison to the Wave equation code. Two configurations were created using the same material models, a thin-wire model and a larger cross-section model. Both

were constructed of sequential tissue, bone, and lung materials of 500mm length. Table O contains the calculated wave speeds for the Abaqus simulations (based on the arrival time of the wave) and the corresponding cross-sectional dimensions of each model. Whilst the percentage error is high for the lung material, it does show the correct order of magnitude for wave speed in both cases.

Table O – Abaqus 1D Wave Propagation Assessment

Material	Thin-Wire Wave Speed (m/s)	Abaqus (10x10 mm) Wave Speed (m/s)	Percentage Error (%)
Tissue	173	196	13.3
Bone	1669	1515	9.2
Lung	27	93	244.4
Material	Dilatational Wave Speed (m/s)	Abaqus (500x500 mm) Wave Speed (m/s)	Percentage Error (%)
Tissue	1512	1667	10.3
Bone	2169	1923	11.3
Lung	33	65	97.0

For evaluation of the 1D wave equation, the code was run using the elastic moduli and densities presented in table N and with adjusted elastic moduli values to adjust the expected wave speed. This was done as the 1D wave equation uses the thin-wire representation of wave speed and cannot account for the dilatational wave speed expected to be observed. The adjusted elastic moduli values were 2286MPa, 7902MPa, and 0.326MPa for tissue, bone, and lung respectively. A comparison of stress at the centre of each material is shown overleaf in figure 20.

Results show that Abaqus CAE is reasonably capturing the wave propagation speed for the three material models and producing suitable stress magnitudes at the boundaries. This has also successfully demonstrated that the dilatational wave speed is expected to apply in the Abaqus thorax model, not the thin-wire wave speed (based on arrival time of the wave at boundaries). Adjustment of the elastic modulus of the wave equation material models was successful in replicating this change in wave speed. For all comparisons between the wave equation and the Abaqus simulations the material models replicating the dilatational wave speed will be used for the wave equation.
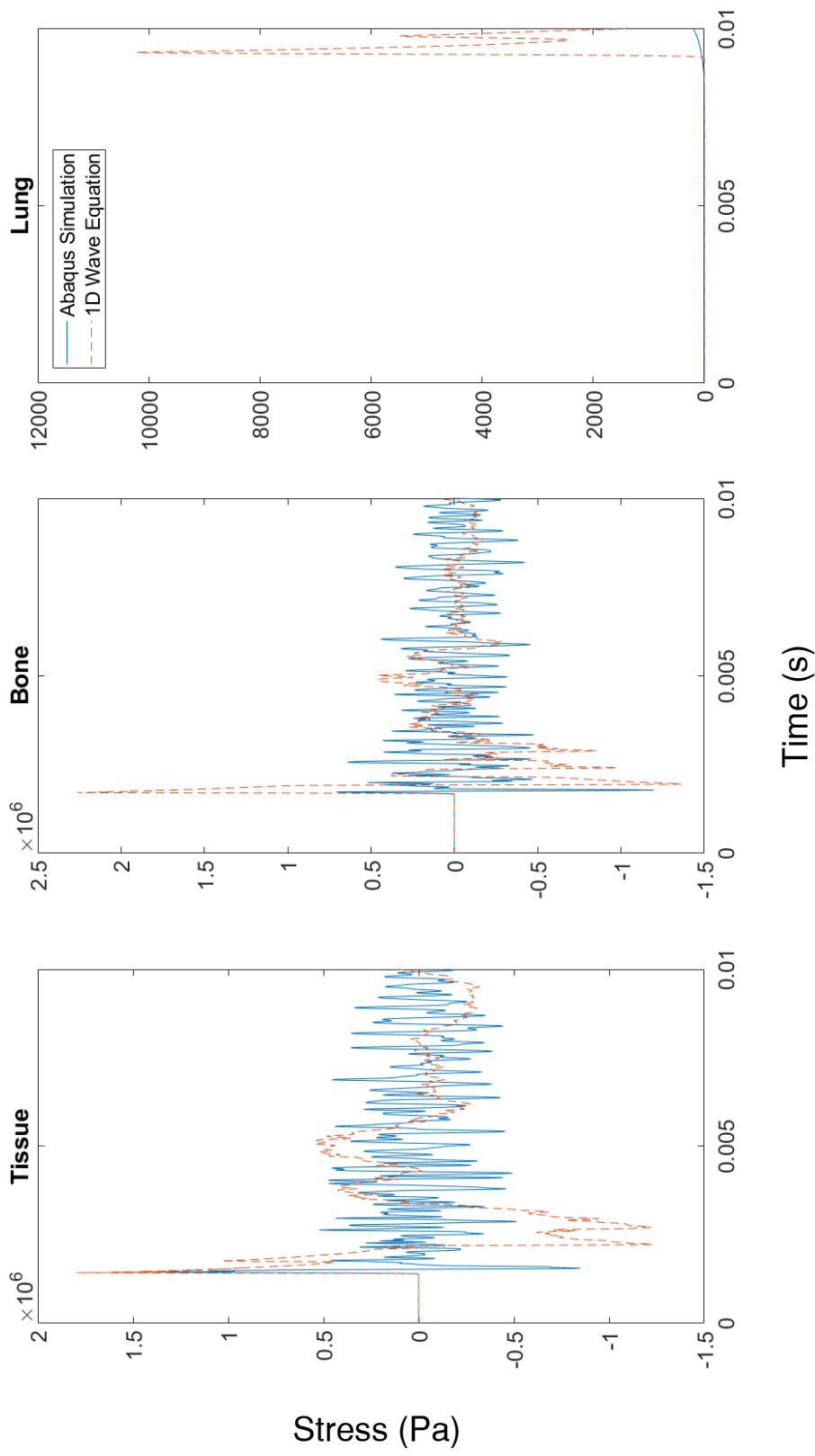
Figure 20: *Comparison of Abaqus FE pseudo-1D simulations and the 1D wave equation for midpoints of the materials. Results show reasonable magnitudes stemming from the reflections at boundaries. Wave equation materials' elastic modulus was adjusted to mimic the dilatational wave speeds (see equation 17, 18, and 24).*

5. Blast Loading Simulations
of Open Field Scenarios

5.1   Determining Loads Representing Injury Severity

To investigate the thorax's response to a blast load, the expected injury severity must first be established. As outlined in chapter 2, the lethality curves are an accepted standard for predicting injury severity in open field scenarios. These studies have also discussed the dominance of peak pressure versus impulse as dominating factors in producing injury and the concept of long and short duration loading.

For this study short duration loading was taken as 2ms while long duration loading was taken as 10ms. This was used as the upper limit as it represents a point on the Bowen and Bass lethality curves where the curves become approximately continuous horizontal lines, representing that peak pressure is the dominating factor in lethality probability. The lower limit of duration was selected to be well within the range where impulse is a significant factor yet still produce a suitably stable pressure wave form (i.e., produce pressure waveforms within the range of validity for the Kingery-Bulmash scaled distance for TNT).

Using the data taken from the lethality curves through the Kingery-Bulmash methodology returned a clear difference in offset distance of subject from a TNT charge between the short and long duration loading. Short duration loading was expected in the near field while long duration loading was expected in the far field. For this reason, the simulations will be referred to as near field and far field respectively. Data extracted and converted using the Kingery-Bulmash methodology is shown in table I in chapter three, including peak reflected pressure, TNT charge size, and offset distance.

It should be noted that these pressures are lower than those used by Greer [6] who investigated the same durations but at much higher pressures. For example, Greer's injury threshold for the short duration loading is also 200kPa, but the 50% probability of injury used by Greer was 700kPa, as opposed to 410kPa identified here. For the far field: Greer investigated 100kPa and 400kPa for threshold of injury and 50% probability of lethality. Once again, this study opts for lower pressures of 85kPa and 180kPa respectively. This is due to the differences in the Bowen and Bass curves. Using Bass' data (lower pressures) should provide more conservative results.

Simulations were run for the threshold of injury cases for both the near and far fields as stresses produced in these scenarios are expected to be representative of the allowable limits before tissue damage will occur. Simulation results at increased loading would be unrealistic to evaluate as a

damage model would need to be implemented to achieve accurate results. Investigations into the threshold of injury in this study could be used to inform the development of a damage model for future use or further development of this model.

5.2   1D Wave Propagation in the Thorax

To investigate the pressure within the thorax for the simulations, several pathways were defined for which the 1D wave equation code could be applied as a comparison to the Abaqus produced data. Pathways are orientated along the direction of blast propagation when acting on the chest. These pathways were selected to correspond with regions of the lungs where different concentration of injuries would be expected based on the batwing pattern observed in CTs. Pathways in the thorax were equally separated horizontally such that they are distal to, proximal to, or intercepted by the mediastinum. Pathways were also equally separated vertically to be upper, central, and lower. Upper and lower pathways are in regions of greater confinement (i.e., closer to the apex/bottom of the lungs, reduced thickness of lung on pathways). Location and identification of the pathways is shown in figure 21 while the constituent material lengths used in the 1D wave equation code for each pathway is shown in table P.

Principal stress acting in the direction of blast propagation was extracted from the Abaqus simulation for comparison to the 1D wave equation. To compare the two methods, the stress histories at the midpoint of each lung material instance on the pathway were compared. Simulations were run for a duration that allowed loading to begin and the initial wave to propagate twice through the lungs (i.e., once from the front to the rear as the incident wave, and once from the rear to the front as a reflected wave). This was the duration in which stresses were expected to be greatest and damage was expected to occur. Results for lung midpoint stress histories on central plane pathways are shown in figure 22 overleaf (page 59).

Figure 21: Thorax pathway locations. Note that pathway 4 is located at the centre of the right lung. All pathways are located on planes relative to this central axis such that they are on an upper, central, or lower plane, and are proximal to, distal to, or intercepted by the mediastinum. For example, pathway 4 is proximal to the mediastinum, while pathway 3 is distal, and pathway 7 is intercepted by the heart.

Table P – Thorax Pathway Material Lengths

Pathway	Tissue (mm)	Bone (mm)	Lung (mm)	Tissue (mm)	Lung (mm)	Bone (mm)	Tissue (mm)
1	39.70	10.80	124.55	7.38	N/A	27.96	27.21
2	39.02	N/A	164.62	N/A	N/A	9.87	37.39
3	22.60	13.26	163.65	N/A	N/A	20.38	27.31
4	18.40	13.1	204.02	34.18	N/A	N/A	N/A
5	34.50	N/A	198.27	28.33	N/A	N/A	N/A
6	48.90	N/A	23.1	34.53	136.79	23.78	16.10
7	13.60	19.50	28.01	89.03	73.88	N/A	49.76
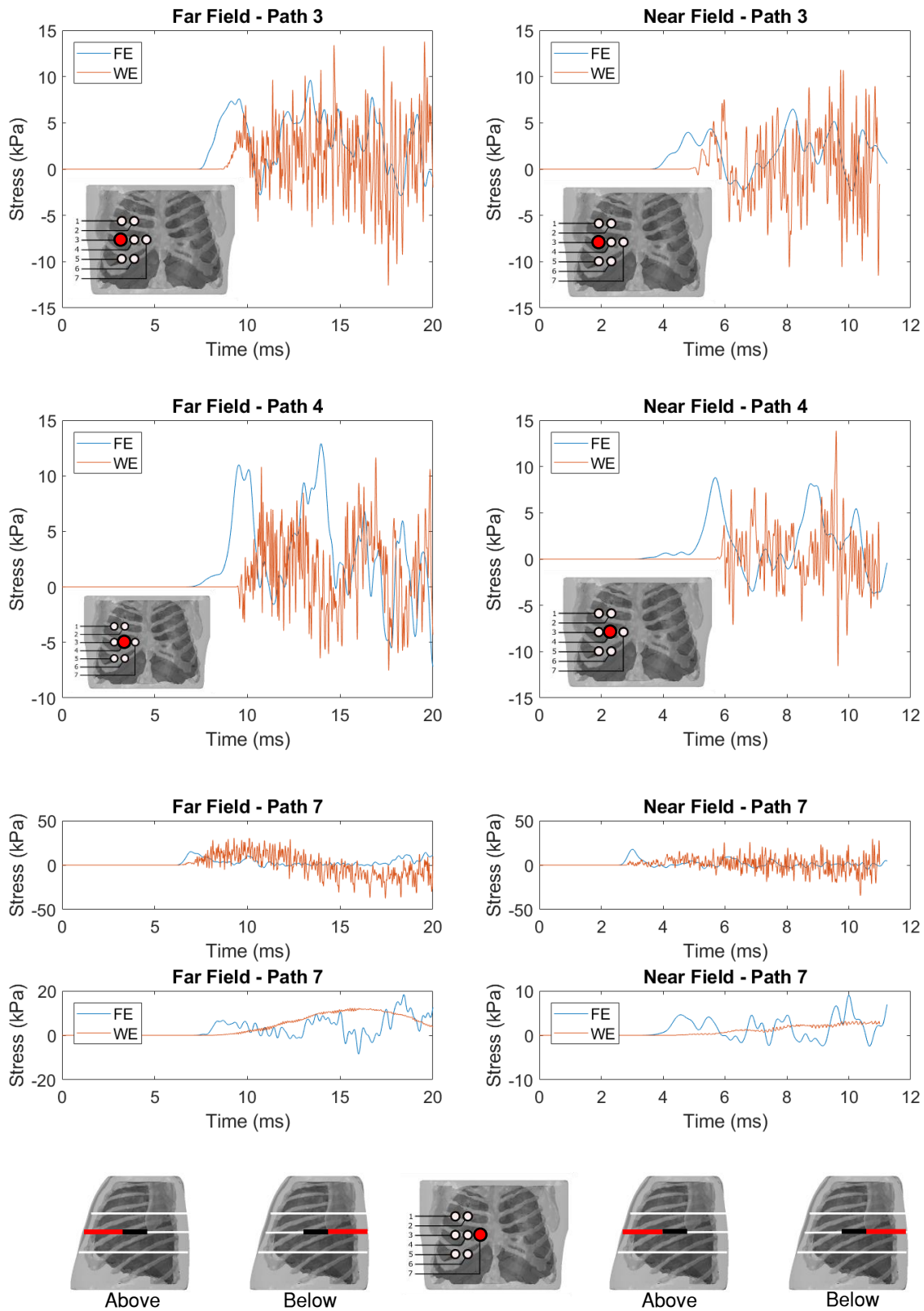
Figure 22: Predicted stress histories from the mid-point of each lung material instance on pathways 3, 4, and 7 for the far field (left) and near field (right). Pathway 7 has two instances of lung separated by the mediastinum, which are shown sequentially vertically (see in-set diagrams defining paths). Stress histories are produced in Abaqus (FE) and using the 1D wave equation MATLAB code with adjusted material parameters (WE). For the wave equation analysis, bone was modelled as tissue and elastic moduli were adjusted to produce dilatational wave speeds which are observed in the FE.

It should be noted that Abaqus simulations use the previously derived material models with dilatational wave-speed observed to be governing the wave propagation (based on the known thickness of the tissues and the arrival time of the stress wave). To maintain consistency between the methods, the wave equation uses adjusted values of elastic modulus to achieve equal wave speeds. This was necessary as the wave equation is only valid for the thin-wire expression of wave speed. A comparison of these values is shown in table Q.

The wave equation (WE) results feature significant oscillations compared to the finite element (FE) results. This was due to reflections generated in the first tissue/bone instances where the reflected waves rapidly propagated between boundaries causing high frequency loading of the lung instance. Despite this, the peak stresses produced are within reasonable agreement between the FE and WE, and stress histories even appear to be similar in duration of positive phase loading if out of phase. It should be emphasised that the results shown are for loading that was initiated at the same time, meaning that the later arrival of the wave equation waveforms is due to a physical aspect of the wave propagation. This could be due to the 3D nature of the FE allowing waves to propagate to the region of interest via an alternative, shorter, route. Alternatively, it may represent a failure to match the wave speeds between the simulations exactly. Further analysis is required to assess the peak stresses more precisely and track them spatially. This data can be found in figures 23 and 24, in which peak stresses are plotted in terms of magnitude (x-axis) and timepoint at which they occur (y-axis) with colour bands indicating the percentage depth in the thorax (blue indicating the front surface of the thorax as 0% and red indicating the rear surface as 100%). As only the lung peak stresses are assessed, 0% and 100% depth will not occur on the graphs as these regions are comprised of skin.

Table Q – Comparison of Adjusted Elastic Modulus for Wave Equation

Material	Abaqus Elastic Modulus (MPa)	Thin Wire Wave Speed (m/s)	Dilatational Wave Speed (m/s)	Wave Equation Elastic Modulus (MPa)
Soft Tissues	30	173	1512	2286
Bone	4679	1669	2169	7902
Lungs	0.2156	27	33	0.3263
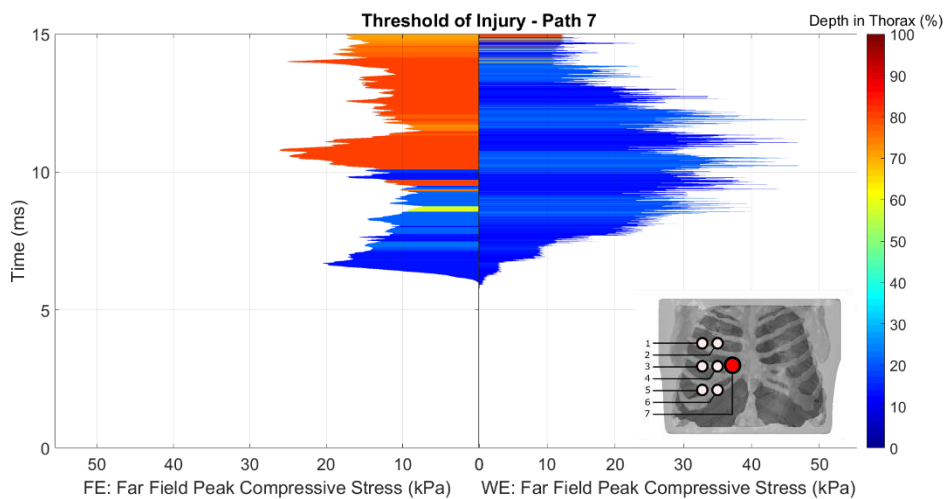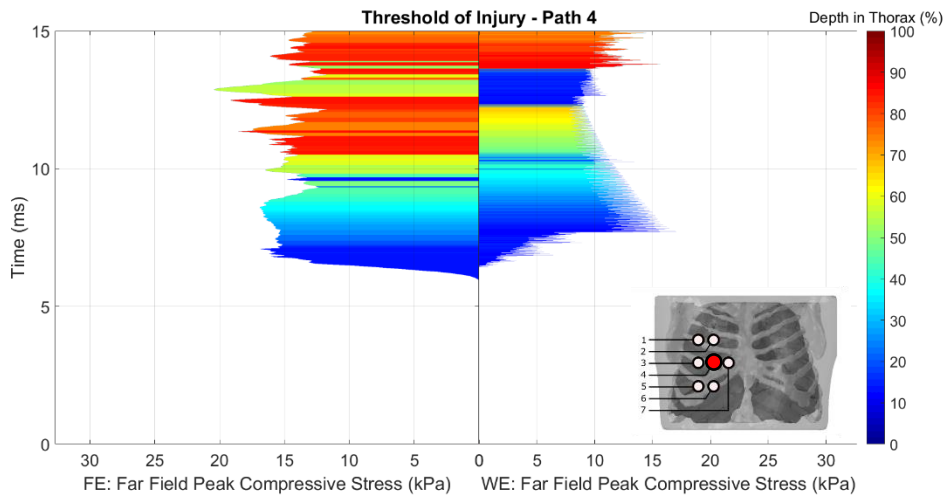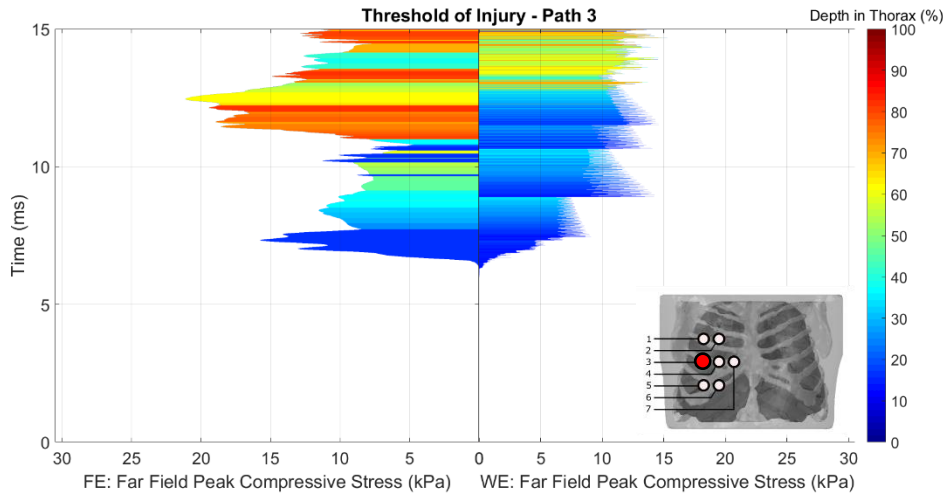
Figure 23: Peak compressive stress magnitude tracking comparison of the finite element (FE) and wave equation (WE) models in the far field. Lack of agreement between the results could be due to the limitations of 1D modelling. There are notable differences in the location and magnitude of peaks, which is not representative agreement seen in previous analysis of figure 22. Only compressive stresses are shown, but tensive stresses displayed similar disagreement between methods with the 1D results remaining focused in front of the thorax and displaying greater magnitudes of stress.
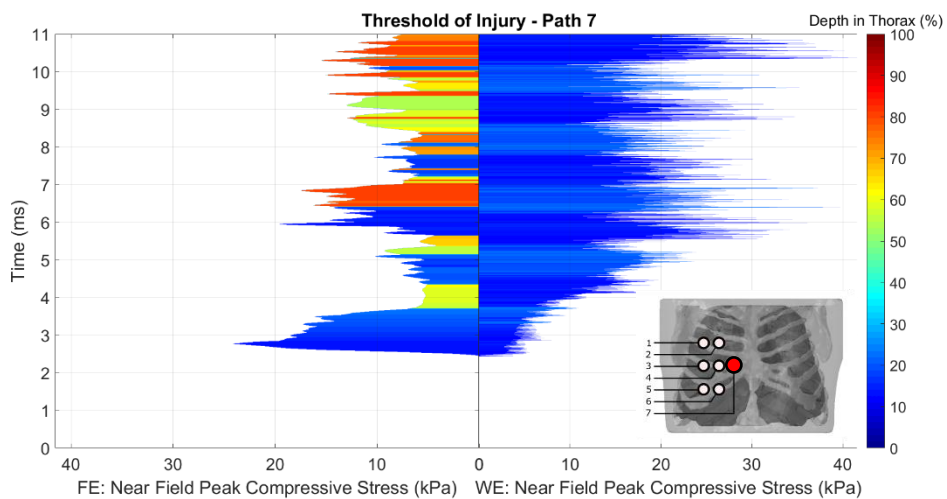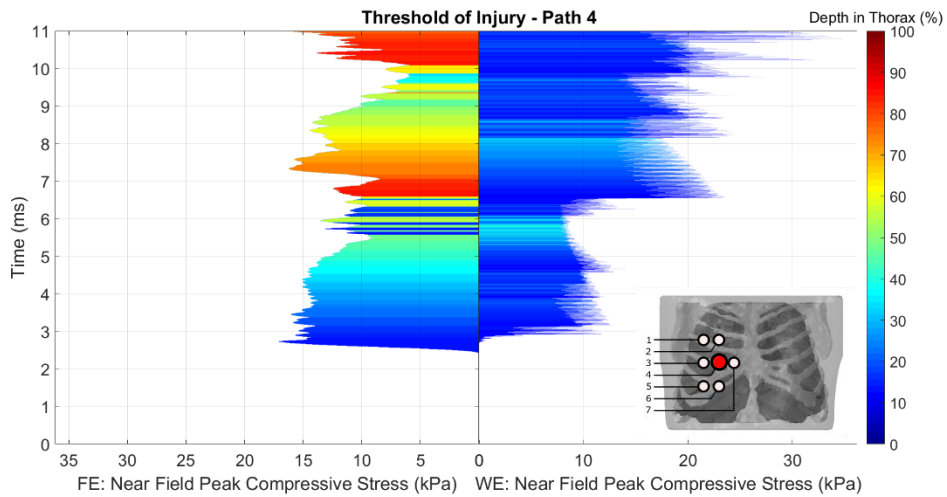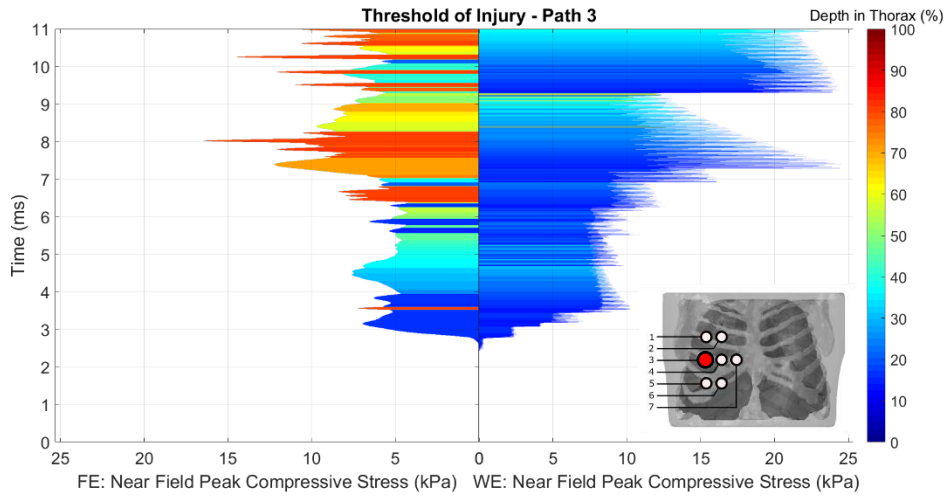
Figure 24: Peak compressive stress magnitude tracking comparison of the finite element (FE) and wave equation (WE) models in the near field. Lack of agreement between the results could be due to the limitations of 1D modelling. There are notable differences in the location and magnitude of peaks, which is not representative agreement seen in previous analysis of figure 22. Only compressive stresses are shown, but tensive stresses displayed similar disagreement between methods with the 1D results remaining focused in front of the thorax and displaying greater magnitudes of stress.

Comparison of the WE and FE data in figures 23 and 24 corroborates that the peak stresses are within the correct magnitude, but the wave equation predicts that the peak stress remains at the first tissue-lung interface for a longer duration, never leaving this location in the near field scenario. This is possibly due to the constraints of the 1D simulation as elements do not experience deformation due to strain, do not account for stresses scattered within the FE, and do not experience loading from multiple directions as in the FE (from the blast wrapping around the target and rapid propagation in soft tissues and bone carrying stresses to the rear of the model). Nonetheless, this shows that the computational model is operating within acceptable limits but also highlights that 1D analysis may be insufficient in analysing the bodies response to blast loading.

5.3   Identifying Injury Predictors

The data from the near and far field threshold of injury simulations was evaluated to identify whether a singular metric could be identified as consistently representative of injury in both scenarios. Firstly, the stress contours at equal time steps after loading began were overlaid onto a transparent CT image of blast injured lung. Results are shown for principal stress in the direction of blast propagation in figure 25.

It can be seen in figure 25 that the peak compressive stress remains close to the mediastinum for most of the loading duration, only spreading distally after reflection from the rear of the lungs in the far field scenario. Matching of these stress distributions implies that the simulation methodology is suitably capturing the primary physics by which lung injury is being induced.

Both the near and far field scenarios show that the wave propagates through the lungs at a similar speed. This is expected due to this behaviour being governed by the lung material model. However, the stress magnitudes produced by both simulations are also very similar, implying that despite the differences in loading, a similar stress distribution and magnitude is produced in the lungs leading to a theoretically similar probability of lethality.

Examining the peak stresses more closely, table R contains a summary of the peak stresses reached for each defined pathway with maxima defined as the greatest magnitude of tensive stress and minima defined as the greatest magnitude of compressive stress. Although not shown via a figure, it should be noted that the principal stresses in alternative directions reach reduced peaks but presented similar agreement with the injury pattern shown in the CT image.
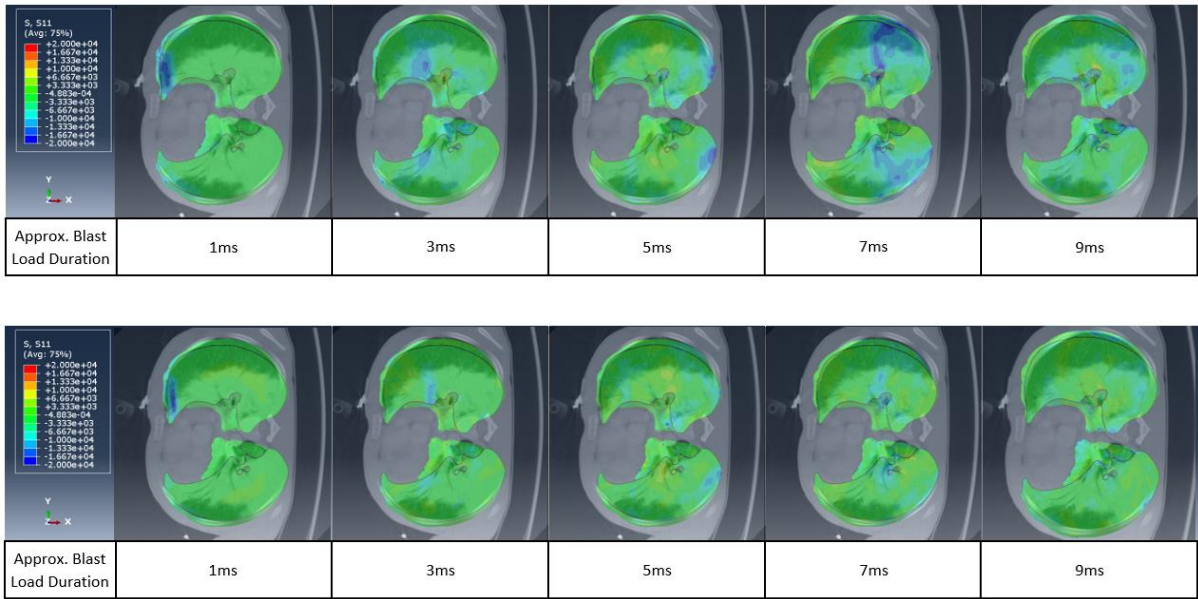
Figure 25: Principal stress contours within the lungs for threshold of injury scenario loading in the far (top) and near (bottom) fields. Contours are overlaid onto a transparent CT image of blast injured lung. In the CT, injured regions appear as a higher image intensity (lighter) and are focused on the mediastinum. The simulation results shows that the principal stress in the direction of blast propagation is greatest in magnitude within the same region, implying correlation with tissue damage. Note that the convention is that positive stress is tensive while negative stress is compressive. Animated versions of this figure can be found on figshare.com using the following DOI for far field and near field results respectively: 10.6084/m9.figshare.25631856   10.6084/m9.figshare.25631874

Table R – Peak Stresses in the Lungs for Simulation of the Threshold of Injury

Pathway	Far Field Scenario		Near Field Scenario	
	Minima Stress (kPa)	Maxima Stress (kPa)	Minima Stress (kPa)	Maxima Stress (kPa)
1	20.267	7.496	16.020	10.003
2	33.841	14.118	19.981	11.173
3	21.125	7.675	16.477	14.850
4	20.446	10.576	17.161	8.763
5	22.174	6.677	22.687	10.855
6	25.577	9.088	21.959	12.245
7	26.151	9.060	24.168	10.381

The minima stresses are consistently higher in the far field scenario, ranging up to 13kPa difference. However, the maxima are slightly more consistent between scenarios with stresses differing up to ±7kPa. As this is the threshold of injury case, the maxima and minima would be expected to be representative of the stress representative of tissue rupture. For this model, injury would be estimated to begin at 24-34kPa compressive stress or 14-15kPa tensive stress.

In comparison, Greer's analysis concluded that a value of 60kPa dynamic pressure was representative of the threshold of injury. The far field and near field simulations found peak pressures on the designated pathways of 37.3kPa and 16.6kPa respectively. Reduced pressure is expected as this study used reduced loads compared to Greer [6], however it should be noted that the near field lungs experienced a significantly reduced peak pressure compared to the far field despite experiencing a greater peak pressure of loading. As these loading scenarios should be representative of equal subject outcome (threshold of injury), this implies that pressure within the lungs may be unsuitable as a metric for injury prediction.

However, although some of the data shows a trend of greater maxima/minima on pathways proximal to the mediastinum, it is not consistent. For example: the smallest maximum in the near field occurs on pathway 4, approximately 8.7kPa, which should be proximal to the heart with an expectation of higher stresses than distal pathways 1, 3, and 5 to be representative of injury. This data is insufficient for determining whether these variables are suitable as injury predictors so information on how the peak stresses develop with time and location must be considered next.

Examining the FE data for individual pathways on the central plane more closely (figures 26 and 27), after the initial pass of the wave the greatest peak stresses occur at the centre and rear of the pathway, as shown in figure 25's contours. Compressive stress does not appear to be a good predictor of injury as the peak stresses reached are very similar on all pathways, and relatively similar magnitude peaks occur throughout the depth (see table R for approximate values for each pathway). This does not agree with the expectation that greater peaks would be expected closer to the interfaces between materials.

As previously identified, the tensive peak stresses offer a better predictor of injury. They occur mainly at the front and rear of pathway 3 (distal), at the centre of pathway 4 (proximal), and at the centre and front of pathway 7, which intersects the mediastinum so higher peaks at the front of the thorax are expected. These all correspond to regions where injury is most likely to occur. The peak tensive stresses occur at these regions for several milliseconds with varying magnitude around 8.7kPa (as identified in the maxima/minima analysis). This implies that 8.7kPa tensive stress may be a suitable indicator of the stress required for lung tissue rupture in this model, with higher peaks occurring for brief durations at the interfaces of materials.

Finally, to clarify whether the peaks are occurring simultaneously in multiple elements and validify the specification of the location of peak stress, it was examined how many elements failed a criterion of 8.7kPa tensive stress at each time point and cumulatively throughout the simulation. It was found that across all pathways less than 0.5% elements failed, and only up to 2 simultaneously. This implies that although a higher maximum is obtained, 8.7kPa is likely a better indicator of injury, and that the peaks shown in figures 26 and 27 are suitable for representing unique elements experiencing the peak stress (unlikely data is being obscured by only examining the peak stresses).
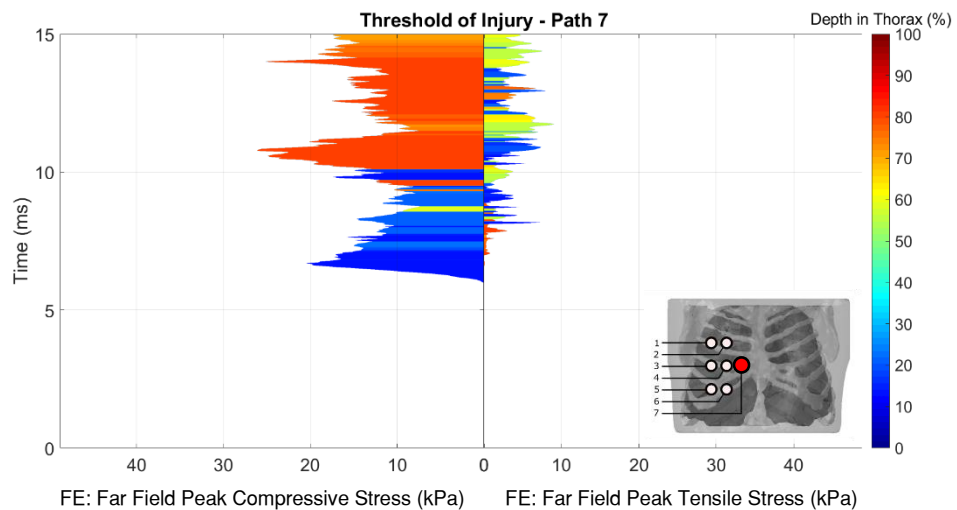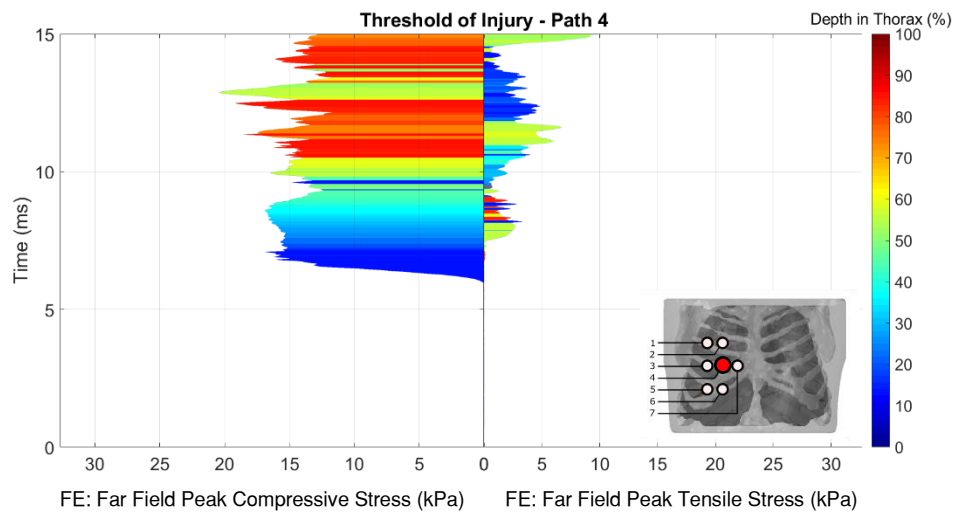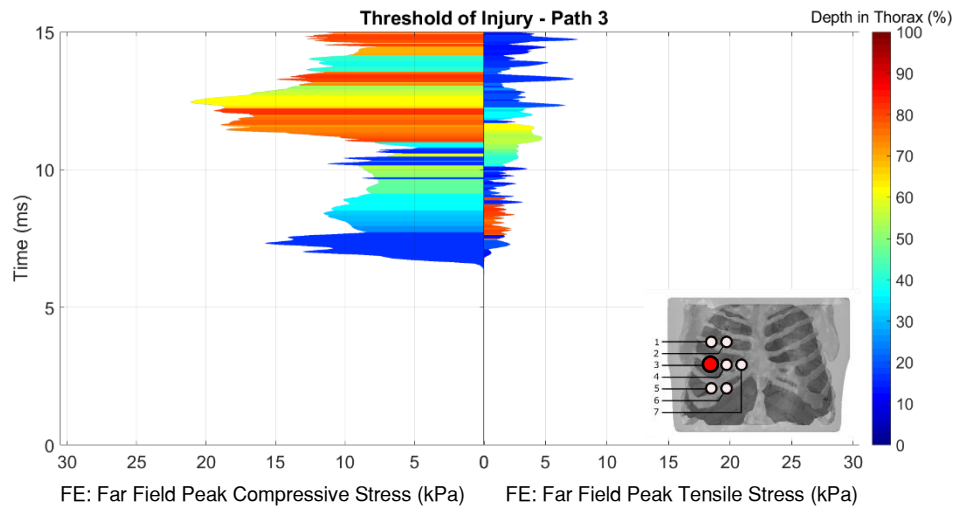
Figure 26: Comparison of stress peaks varying with time in the far field. Location of the peaks informs where injury is likely to occur whilst the magnitude provides an estimate of the stress required to rupture the lung tissue specific to this model. As simple material models are used, this is not necessarily representative of the peak stresses observed in realistic scenarios however it provides an estimate of which parameters are suitable as injury predictors.

Figure 27: Comparison of stress peaks varying with time in the near field. Location of the peaks informs where injury is likely to occur whilst the magnitude provides an estimate of the stress required to rupture the lung tissue specific to this model. As simple material models are used, this is not necessarily representative of the peak stresses observed in realistic scenarios however it provides an estimate of which parameters are suitable as injury predictors.
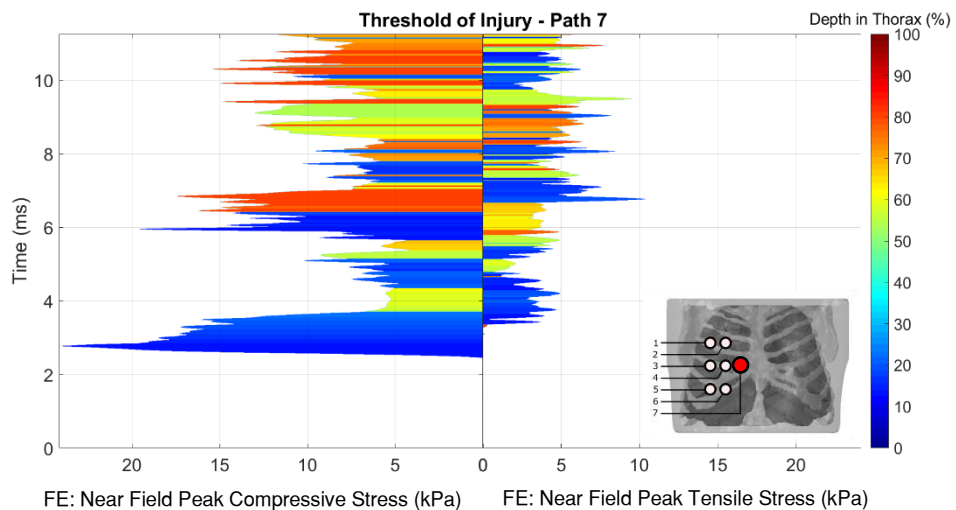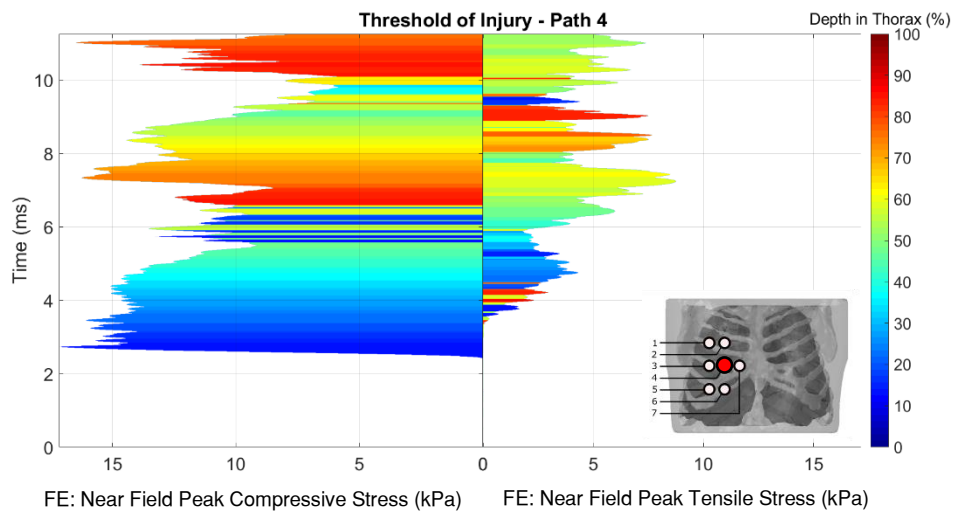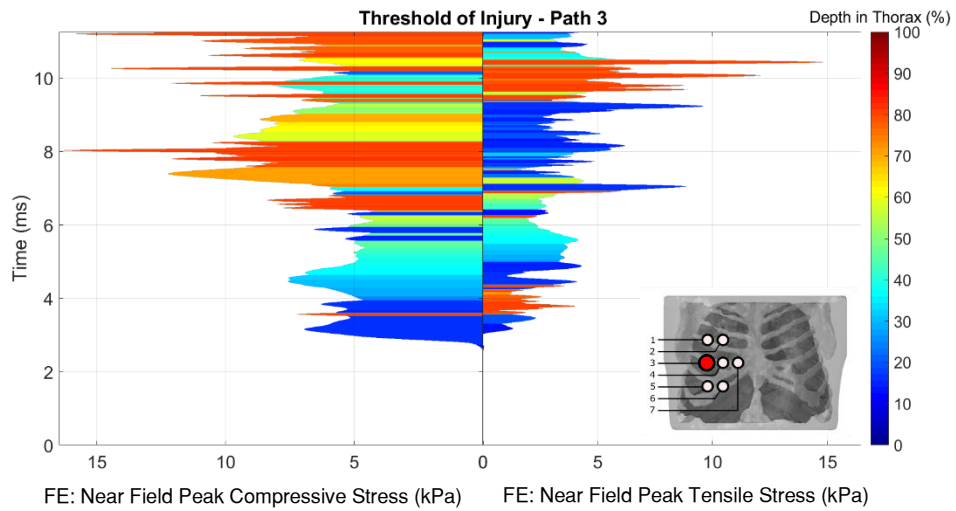
6. Additive Manufactured Model of the Human Thorax

6.1 Material Characterisation in Literature

To validate the simulations and investigate the internal stresses experimentally, an additive manufactured (AM) model representing the human thorax was designed. This model was manufactured by 3DLifePrints Ltd using a PolyJet printer and underwent blast loading produced via a shock tube in partnership with Aber Shock and Detonation Research Ltd. Ideally the model would utilise the same material models as used in the computational study, but this was dependent on the printable materials available. Literature data was gathered on the mechanical behaviour of several common PolyJet compatible materials before compression, tensile, ultrasound, and relaxation testing was carried out on selected materials to characterise their properties. The materials researched included Agilus-30, various Vero materials, Tango Gray, Tango Black, Tango Black Plus, and Ecoflex materials. It should be noted that the Vero materials are categorised by their colours but typically have very similar mechanical properties (usually identical) according to the manufacturer data sheets [101].

Data sheets from the material manufacturer indicate that Vero materials are expected to have elastic moduli in the range of 2000 to 3000 MPa with a density of approximately 1175kg/m^3 [101]. The softer materials instead have reports on the expected shore hardness values. Formulas presented by Gent allow approximate prediction of elastic modulus values [102]. These conversions are shown in table S overleaf. These values do not necessarily provide accurate information on the mechanical behaviour of the materials (in terms of elastic modulus) but serves as a guide for further research/testing. It can be seen immediately from these results that the Vero materials are expected to behave like bone and the softer materials are possibly good for representing soft tissues and the lungs. Large differences in the elastic moduli imply differences in wave speed and acoustic impedances, which should effectively mimic the expected reflection/transmission behaviour of waves at the interfaces of biological tissues.

Experimental testing of the Vero materials indicates strong agreement with the manufacturer data sheet with elastic modulus reported as lying between 2000 and 3000 MPa [103-106]. Tests to determine Poisson's ratio also indicated that Vero materials had values like those used for bone biological material models (0.33) [107] and the soft materials would be expected to behave close to incompressible assumption based on results of Tango Black Plus (0.49 [107], 0.49, and 0.48 [108]).

Table S – Data Sheet Derived Shore Hardness and Elastic Modulus Values for PolyJet Materials

PolyJet Material	Manufacturer Reported Density (kg/m^3)	Manufacturer Reported Shore Hardness Value	Calculated Prediction of Elastic Modulus (MPa)
Tango Black Plus	1125	A26 – A28	0.965 - 1.051
Tango Black	1145	A60 – A62	3.605 - 3.908
Tango Grey	1165	A73 – A77	6.372 - 7.852
Agilus-30	1145	A30 – A35	1.142 - 1.395
Ecoflex 5	N/A	A5	0.278

Stress relaxation testing of Agilus-30 in tension completed by Dykstra has identified strong viscous components to its mechanical response. The behaviour was fitted to a linear Maxwell-Wiechert viscous model expressed as a neo-Hookean material model. In this experiment, the instantaneous elastic modulus was determined as ranging from 2.58 – 3.25 MPa depending on the number of terms used for the model [109]. The results of the testing included hysteresis loops of the material force-strain response under various strain rates. These graphs show how increasing the strain rate iteratively can lead to hysteresis loop becoming progressively more akin to linear elastic behaviour. The greatest strain rate of the results presented in this experiment was $3.09E\text{-}3s^{-1}$, which is still significantly less than strain rates expected in blast scenarios ($1000s^{-1}$). This contributes to the assumption that linear elastic behaviour could serve as a suitable description of material behaviour under blast loading.

Testing of a Vero material and Tango Black Plus indicates that both are strain rate sensitive. The Vero material produced an elastic modulus of 2504MPa at 1mm/min of loading, and 1618MPa at 300mm/min. The Tango Black Plus material produced an elastic modulus of 1.55MPa at 1 mm/min of loading, and 15.46MPa at 300mm/min. This shows that the softer material has a significantly more prominent viscous response, with an almost 10x increase in elastic modulus within the parameters of the testing. The Vero material displayed significantly less strain rate dependency, but also showed a reduction in elastic modulus instead of an increase [110].

An additional material was considered of Agilus-706B. This is a material typically used to support structures during printing and intended to be discarded during washing after printing. However, 3DLifePrints had previously utilised this material within a model by encasing it in a thin shell (0.5 – 2mm thick) of Agilus-30. This model was intended to be used as a physical analogue of the variation of how tissues felt to touch when compared to other PolyJet materials. The precise mechanical properties were not relevant for that model and so no material characterisation studies had been previously carried out. No reliable literature data could be sourced on this material. Several samples were requested from 3DLifePrints as part of this study's material characterisation testing as a possible surrogate for lung tissue.

6.2   Experimental Material Characterisation

Samples of Agilus-30, Vero White, and Agilus-706B (encased in 0.5mm thick Agilus-30 shell) were acquired from 3DLifePrints for compression, tensile, and ultrasound testing. Compression samples were 50mm diameter cylinders of 25mm height, which could also be used in ultrasound testing. Tensile samples were dog-bone samples with 50mm gauge length, 13mm width, and 3.3mm thickness. Samples are shown in figure 28. Dimensions of the compression samples were selected such they could be used in conjunction with the compression testing platens and the ultrasound probes within the Swansea University laboratory. Cylindrical compression sample geometry is compliant with ASTM standard D1621-16 [111]. Dog bone sample geometry was designed to adhere to ASTM standard D638-22 [112]. Loading specifications were not adopted from these standards.

Samples were tested using suitable platens/clamps attached to a Tinius Olsen testing machine. Prior to testing, the compression samples were weighed using a digital scale and measured using a digital calliper. From these measurements density was calculated for each material. Agilus-30 had a density of 1165kg/m^3, Vero White had a density of 1180kg/m^3, and Agilus-706B (excluding the shell) had a density of 1153kg/m^3. Unfortunately, in the printing process the compression samples developed corresponding convex and concave faces for the Agilus-30 and Agilus-706B samples. This meant the faces were non-planar which would likely affect the results of the material characterisation.
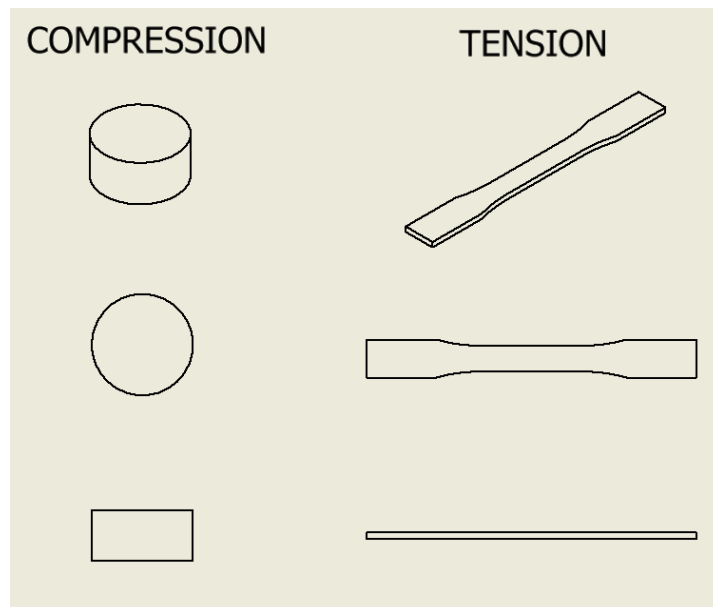
Figure 28: Diagram of cylindrical compression (left) and dog-bone tensile (right) material characterisation samples.

The cylindrical samples were loaded via a stationary lower platen and a variable position upper platen. The variable platen was driven at a velocity of 2mm/min downwards until a maximum force of 0.1N was reached. This was defined as contact occurring and the start of loading. The platen was then driven at 100mm/min downwards until a displacement of 6mm was reached (to achieve >20% strain)

or a force of 750N (to ensure safety of the equipment while operating at relatively high strain rate for this testing machine). Greater strain was not explored to prevent damage to the samples and because excessive strains were not expected in the blast testing. Both platen surfaces were coated with vegetable oil to facilitate slipping of the sample surface, but barrelling was observed in all samples regardless (see figure 29). Displacement was controlled while stress was measured using a 1kN load cell. Stress-strain curves were produced for all samples and an estimate of elastic modulus was taken from them. A high degree of varying non-linearity was observed in the low-strain region, which was assumed to be due to the concave and convex faces. Mean elastic modulus was calculated as 1.607MPa for Agilus-30, and 0.246MPa for Agilus-706B by taking measurements between 15-25% strain, and 10-15% strain respectively (where a linear relationship was evident for both).

Figure 29: Compression testing of the cylindrical samples of Agilus-30 (left) and Ailus-706B (right). Despite applying lubrication using vegetable oil, significant barrelling can be observed when testing both samples.

The Vero material could not be meaningfully tested with the current load cells available (greater than 1kN would be required). To acquire data for these samples, all materials were tested again at a reduced strain rate with adjusted end conditions based on the first round of high strain rate testing. These were 250N for the Agilus-706B samples and 850N for all other samples. The displacement rate was set as 10mm/min for the Agilus materials and 0.1mm/min for the Vero material.

Significant difference in the response in this round of testing would also serve as an indicator that the material is strain rate sensitive. Mean elastic modulus was calculated as 0.945MPa for Agilus-30, and 0.229MPa for Agilus-706B by taking measurements between 15-25% strain, and 10-15% strain respectively (where a linear relationship was evident for both). These results show that Agilus-30 is certainly sensitive to strain rate, but the Agilus-706B has near negligible sensitivity. For the Vero data a mean elastic modulus of 22.128MPa was calculated between 0.5-1.2% strain. Figure 30 contains the stress-strain curves produced for all compression tests. This is significantly less than the expected value from the manufacturers data sheet.

Dog-bone samples were secured using a fixed lower clamp and a variable position upper clamp. The upper clamp was driven at 100mm/min upwards until the sample failed. Samples that slipped from the clamps did not undergo significant deformation and were retested. Some samples exhibited failure

outside the gauge length and were discounted from the testing. Figure 31 contains the stress-strain results of the tensile testing. The most notable result was for the Agilus-706B samples, which exhibited failure of the internal material prior to failure of the Agilus-30 shell. An example of this can be seen in figure 32 overleaf.

In tension, both materials behaved with approximately linear elastic behaviour up to 50% strain. Both materials then began to behave non-linearly, however less than 50% strain would be expected in the blast loads to be performed in the blast testing. This will be discussed in greater detail in the following chapter. For the Agilus-30 material, the mean elastic modulus as calculated as 0.239MPa, while the Agilus-706B elastic modulus was calculated as 0.119MPa (using data up to 50% strain for both). This shows that the tensive and compressive behaviours differ, but the same trend of Agilus-30 having the higher elastic modulus is present. It should be noted that the dominant mode of loading in blasts is compression, and the cylindrical samples have significantly greater mass compared to the dog-bone samples. This means the compression testing is more significant as it is closer to the conditions expected in the blast testing to be performed.
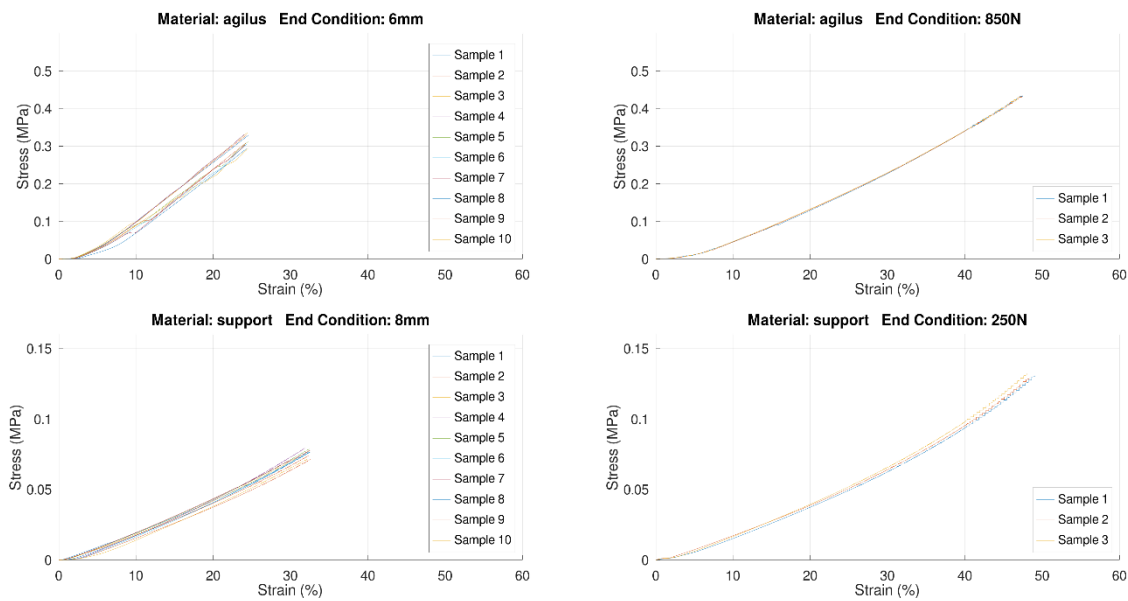
Figure 30: Stress-strain curves of compression testing of two soft PolyJet materials using end conditions of platen displacement (left) and force recorded (right). It was noted that both materials exhibited a sharp change in response at very low strain which was potentially due to insufficient contact definition and the concave/convex defects on the faces of the samples. Although a non-linear response is observed, at low strain a linear elastic response can be assumed.
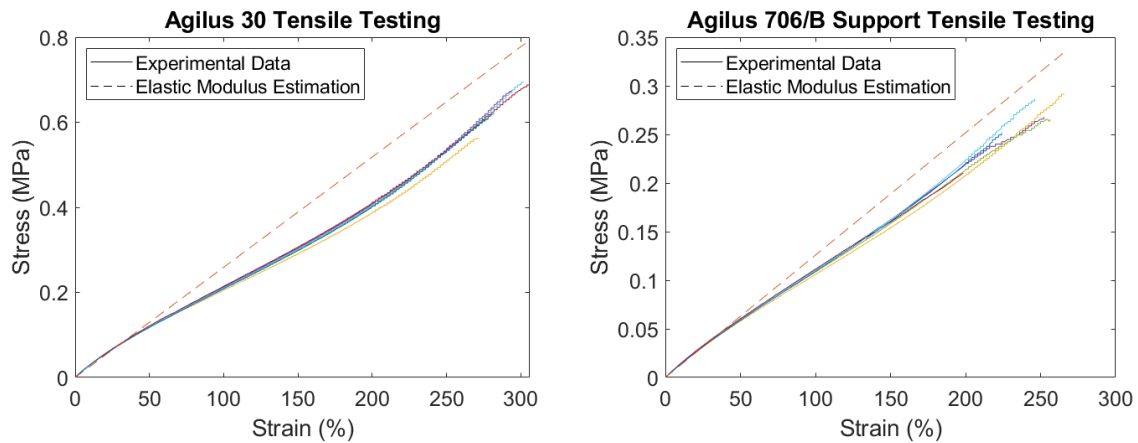
Figure 31: Results of tensile testing of PolyJet soft materials. Both materials show linear elastic behaviour up to 50% strain, which is greater than expected in a blast scenario. All samples were tested until tensile failure, though it should be noted that Agilus-706B clearly failed internally in several steps which were not recorded. Complete failure of the specimen occurred when the outer Agilus-30 shell failed. This means the data is not representative of the ultimate tensile stress. See figure 23 for more information/visualisation.
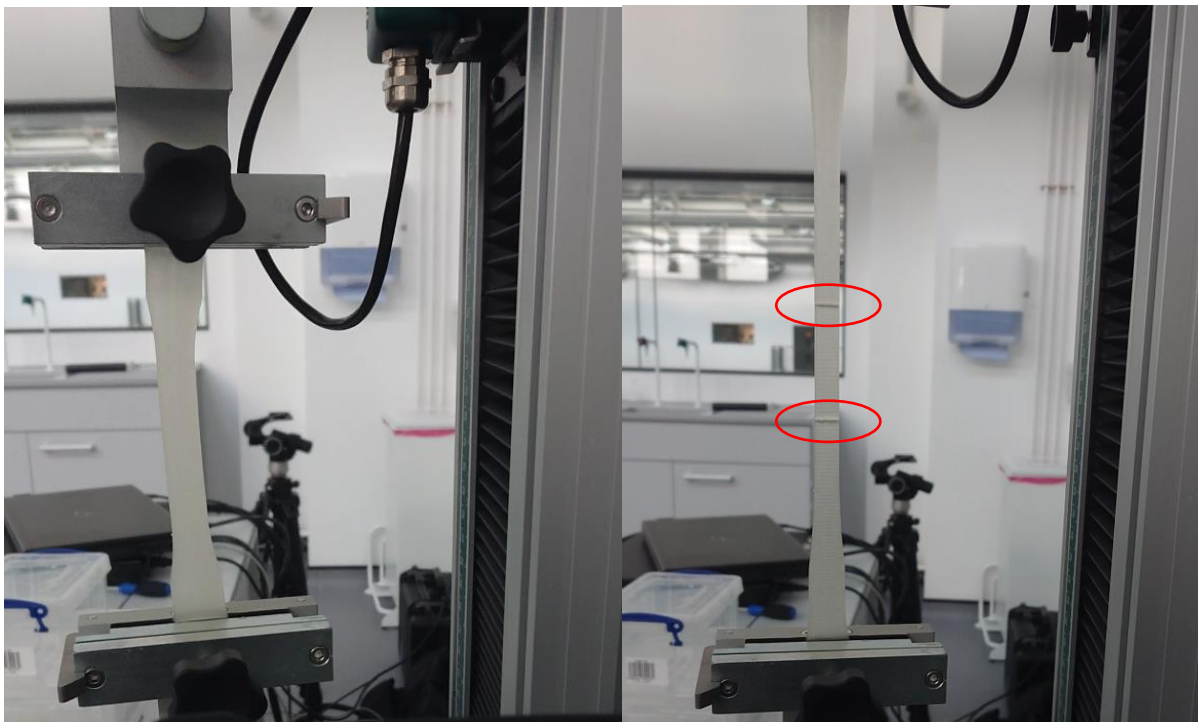
Figure 32: Tensile failure of internal Agilus-706B material during testing whilst Agilus30 shell remains intact. Pre-testing image shown on left and two points of failure are indicated on image on the right taken during testing. Failure appears as bands across the sample where Agilus-706B is no longer present. These instances of material failure were separated by several seconds of testing and preceded complete failure of the sample several seconds after the second instance of failure. Final failure of the Agilus-30 shell occurred at the first failure site to develop in the Agilus-706B material where weakness would now be expected in the sample.

The compression samples also underwent ultrasound testing in A-scan mode to investigate the time of flight of the wave. With the known thickness of material, this allowed calculation of the wave speed characteristic of that material. Ultrasound probes of 1MHz, 2MHz and 4MHz frequencies were applied to a planar surface of the samples coated with ultrasound coupling gel. Ultrasound gel is required to allow the transfer of ultrasound between the probe and sample without encountering any highly reflecting air that would prevent the transmission. The greatest magnitude signal representing the returned pulses were obtained with the 2MHz probe. Samples were tested in two configurations: 1) with the sample on a table surface and the ultrasound probe applied by hand to the top surface, and 2) with the sample resting on the probe held vertically such that the wave would reflect from the opposing material from an air interface. The second configuration was done to ensure the sample wasn't being accidentally compressed in the first configuration but relied on the weight of the sample to ensure contact at the initial probe-sample interface. No meaningful differences were recorded in the results between configurations.

Mean wave speeds of 2338m/s and 1586m/s were calculated for the Vero White and Agilus-706B materials respectively. The mean wave speed for the Agilus-30 could not be determined as a suitably clear signal could not be achieved with any probe despite adjustments in gain. This was assumed to be due to the material damping the low-amplitude wave before it could return to the probe, which was presumed would be a non-issue for high-amplitude blast testing.

From this data, approximate material behaviour can be determined for the tested materials using the most reliable data from across the various tests. For the Vero material, the acoustic impedance can be calculated directly using equation 4. This determined a value of 2.76MRayl. Repeating this analysis for Agilus-706B determined an acoustic impedance of 1.83MRayl. Agilus-30 wave speed could not be determined from testing, though based on the compressive modulus the wave speed and acoustic impedance would be expected to lie between the two other materials. Furthermore, the elastic moduli values determined (and reported by the manufacturer data sheet) align reasonably well with the elastic moduli for biological tissues discussed in chapter four. The wave speeds are also reasonably similar, except for the Agilus-706B similarity to lung. A homogeneous material with a wave speed in tens of m/s is unfeasible, so this material was deemed suitable for initial testing. Future reproduction of this model could likely improve this material selection, possibly by adapting a foam material.

6.3   Model Production for Experimental Blast Testing

The printing process for the thorax model utilised a PolyJet printer at 3DLifePrints with three nozzles. This meant that all model parts could be printed simultaneously, encasing the lung and ribcage parts entirely. The geometry used for the AM model was the same as used for the computational model of the thorax with some modifications. Firstly, the model needed to be significantly smaller to be printable and be relative to the size of the shock tube used for the testing. Reducing the size of the model to fit within the 50mm inner diameter shock tube available was unfeasible, so it was concluded that the sample would have to be mounted externally (open-ended shock tube experiment). Alternative options were explored but the advantages of shock tube experiments include the fast turn-over between tests, high degree of repeatability, reduced cost of performing such experiments compared to detonation of charges, and the confidence in this type of testing due to its widespread use. The methodology of the shock tube testing will be discussed in greater depth in the following chapter.

It was deemed suitable to scale the model to quarter scale, which would allow up to three sensors to be included on the model simultaneously without interfering with each other. Ports were included on the segmentation to allow mounting of PCB piezoelectric pressure sensors (model 113B22) to the thorax model. The sensor is shown in figure 33, with the most notable feature being a lip around the head of the sensor to be clamped between two surfaces (i.e., a surface on the sample and the surface of an externally threaded sleeve provided with the sensor). The sensor has a diameter of approximately 7mm, meaning two sensors could be aligned in parallel to take readings from the same lung for the quarter scale model. For this experiment, the left lung was taken as the region of interest.

Two models were produced. Both included a port on the side of the left lung. This sensor was intended to detect waves scattered by the heart and serve as a consistent reference between the two models. The first model had two sensor ports at the rear such that sensors could be mounted to the back surface of the lung material. This was designed to mimic the pathway analysis carried out in the previous chapter with one sensor being proximal to the mediastinum and the other sensor being distal. All sensors discussed so far were set to be on the transverse mid-plane of the lungs. The second model had one port in the back, and one port on the right side. These ports were significantly deeper and allowed sensors to be mounted to the lung surface through the mediastinum. It was necessary to offset the ports to allow them to cross each other but these were also centred on the transverse mid-plane of the lungs.

Sensors were originally intended to be secured to the thorax models using a sleeve of Agilus-30 to improve the interference fit. This proved insufficient in securing the sensor, so several hollow cylinders with an external thread were printed at Swansea University using FormLabs Rigid 10k to act

as bolts. This material was utilised for its high durability and the capabilities of Swansea University to implement threads in the printing process. Both the ports and the printed bolts varied in internal diameter to provide secure fixing by butting against either side of the lip around the sensor head (see figure 33). This clamped the sensor in place, much like the manufacturer supplied sleeve was intended to. For mounting the model, the spine was extended vertically past the edges of the model as a hemi-circular pin. These pins could be secured with bolts to prevent rotation and translation of the model during testing. This mimics the pin condition that was applied to the spine in the computational simulation. Models produced can be seen in figure 34 overleaf along with overall dimensions. The physical model was approximately 100mm in width, 80mm in height, 45mm in depth at the top of the model, and 75mm in depth at the base of the model.

An additional model was produced to mimic the Axelsson BTD scaled to quarter size to fit within the expected testing field. This model was printed at Swansea University using the same material as used for the thorax bolts, FormLabs Rigid 10k. This material was utilised as the BTD is meant to be effectively infinitely rigid.
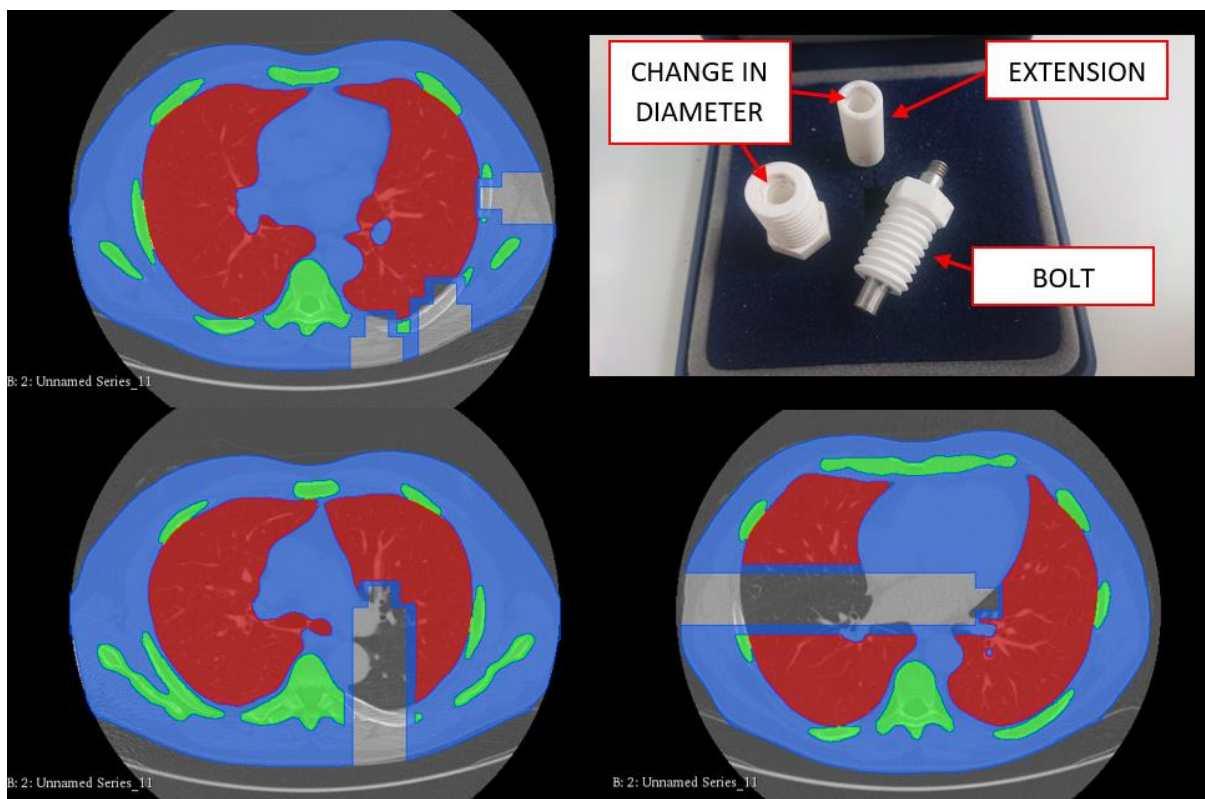
Figure 33: Segmentation used to create model with sensor mounting points and corresponding bolts for mounting sensors. The first thorax model has all three sensor ports shown (top-left), while ports for sensors P8 and P9 are shown for the second thorax model (bottom). Blue indicates tissues (Agilus-30), green indicates bone (Vero), and red indicates lung (Agilus-706B). 3D Printed hollow bolts and tubes (as extension for deep ports) are used to secure sensors (top-right) via interference fit. Note the change in diameters used to secure the sensors as prescribed by the manufacturer.
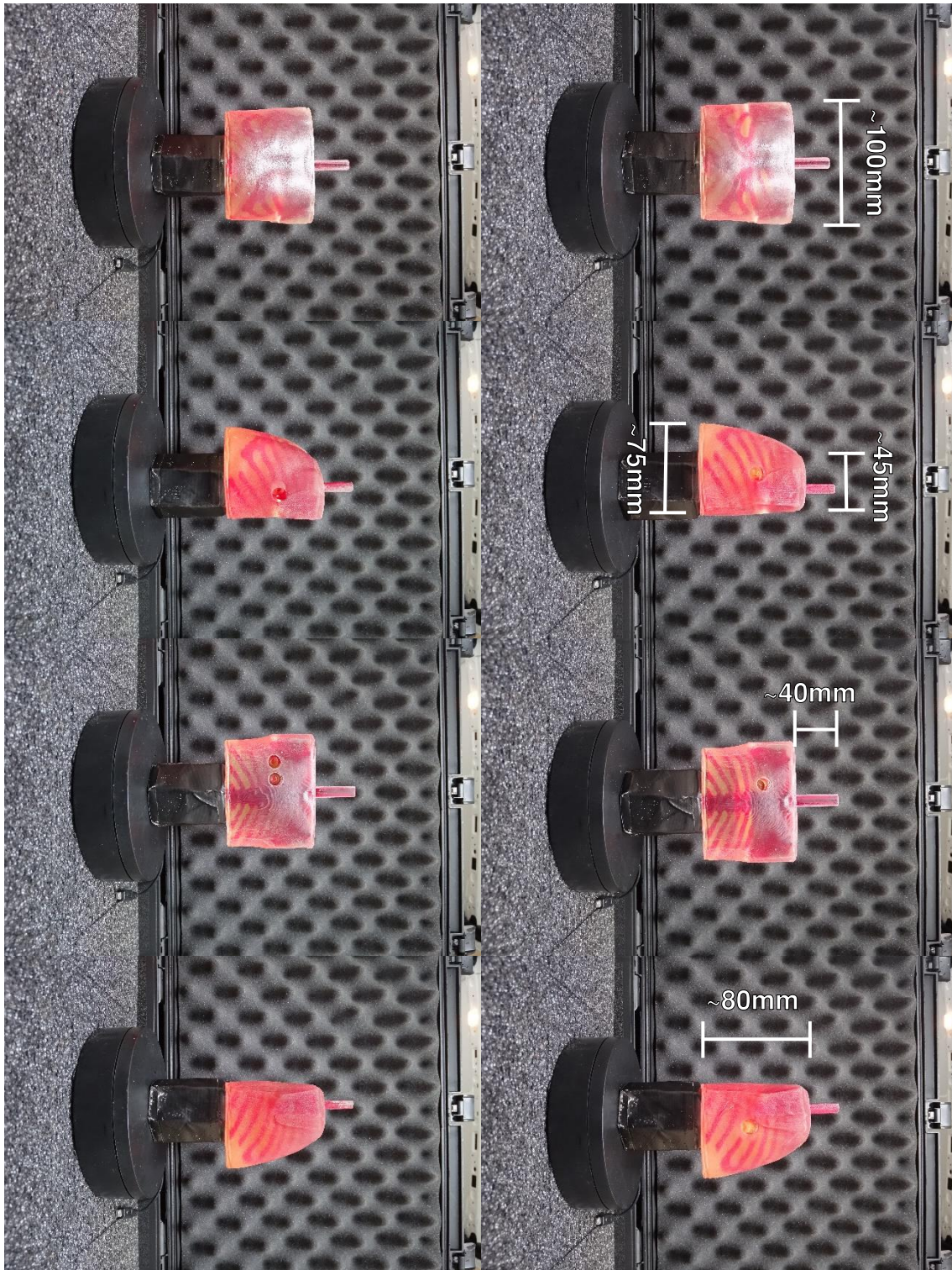
Figure 34: Additive manufactured models of the human thorax (with bottom mounting pin obscured by platform). Two models were designed. On the left is a model optimised for detecting wave propagation in 1D, on the right is a model optimised for detecting stress concentration around the mediastinum. Both models incorporate a sensor on the left side of the model for detecting scattering and as a consistent sensor between the models which can be directly compared. Models were constructed of Agilus-30, Vero, and Agilus-706B materials. All parts were printed simultaneously (i.e., lung part is entirely encased in the other parts). Both models are the same size, created from the computational model geometry and reduced to quarter scale (approximate dimensions shown).

Sensors were mounted to the BTD as specified in the installation instructions provided by PCB, using a manufacturer provided externally threaded sleeve to butt against the lip around the sensor head. These threads were printed with a 400 micron increase in thread pitch to allow for variations in geometry during the printing process due to material expansion. The value of 400 micron was found to be suitable after iteratively increasing the value over several sample prints until a good fit was found. This methodology was developed by Louis Giron at Swansea University who produced the required thread geometry and advised on all designs printed at Swansea University. A diagram of the model can be seen in figure 35.

Sensors needed to be offset to accommodate their length within the cylinder and provide space for wiring. To mount the BTD model using the same method as the thorax model, end caps were designed which would sit within the cylinder, be secured with bolts, and provide an identical pin as used for the thorax model. These end caps were manufactured in the Swansea University workshop and constructed from mild steel as part of a prototype model. The prototype caps were reused to reduce wastage of material printing new ones. End caps are shown in figure 35 with along with the main body of the cylindrical model, including instrumentation of the model and overall dimensions.
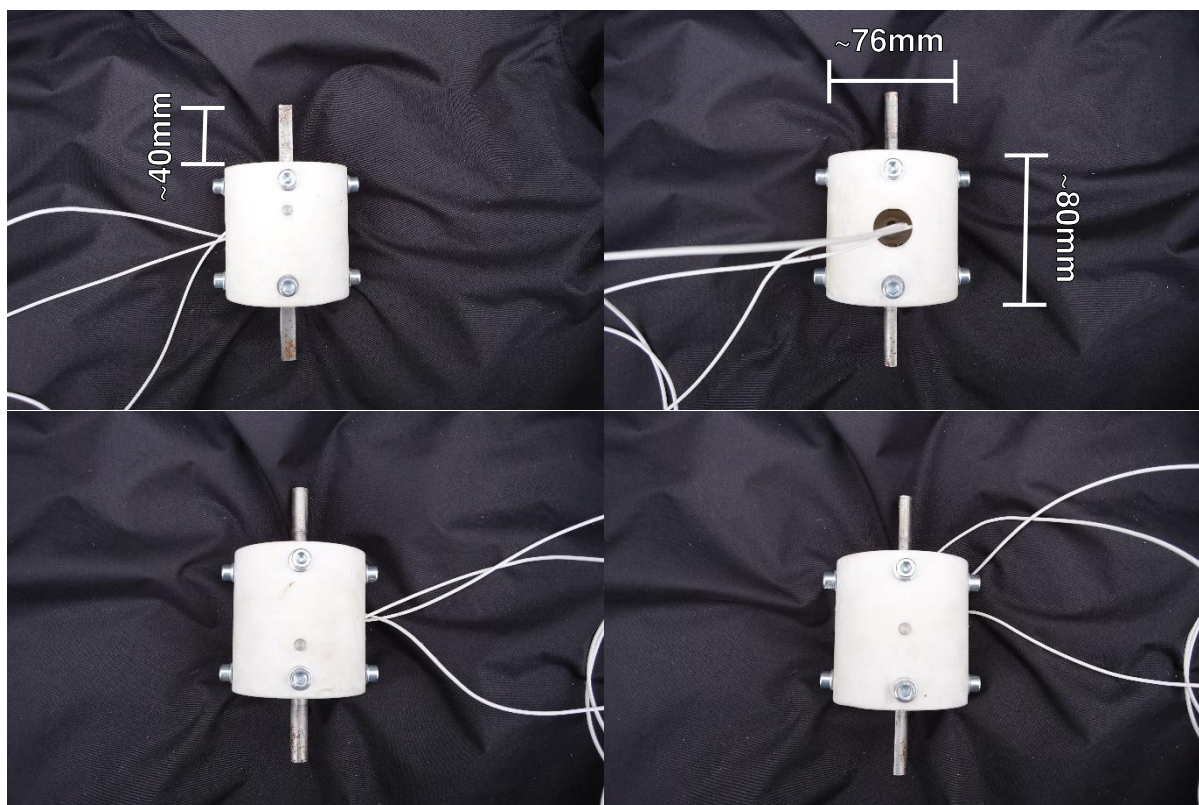
Figure 35: Hollow cylindrical model representing a scaled Axelsson BTD (diameter is quarter scale, height matches the thorax model to use the same mounting equipment). This model us instrumented using the same PCB sensors used for the thorax models. End caps with pins are secured with bolts. Sensors are secured with threaded sleeves provided by the manufacturer. Sensors are offset to accommodate their length and the attachment of the cabling within the hollow structure. Sensors are placed to record data at the front, side, and rear of the sample. Approximate dimensions shown.

7. Preliminary Testing of Shock Tube Loading

7.1   Open-Ended Shock Tube System

Experimental shock tube testing was performed at Aber Shock and Detonation Research Ltd who provided the shock tube equipment, site for testing, and invaluable advice on the experimental methodology. The site used was a farm located in mid-Wales as the experiment required the sample to mounted to the open end of the shock tube and so could not be fired indoors at the required pressures. Experimental testing took place over four non-consecutive days in March 2022 including time spent setting up equipment, performing calibrations, and commencing preliminary and final tests. On the initial days of testing the weather conditions were poor (including rain, snow, and cold temperatures <5°C). The final day of testing included significantly improved weather including higher temperatures (>10°C), though it became progressively wetter and windier as the day progressed. The difficulties encountered with these conditions will be discussed in greater depth later. All tests were recorded using several camera systems with additional periodic photographs taken for reporting on setup and sample integrity.

A shock tube can be divided into a driver section and a test section. The test section was constructed of several sections of 2" (50.2mm) internal diameter schedule 40 carbon steel pipe. When bolted together, the total length of these sections was approximately 3m. One end of the testing section was left open to the air such that a sample could be mounted to the end, whilst the other was capped by the driver section. The total length of the driver section was approximately 1.5m, leading to a total length of the shock tube system of around 4.5m.

The driver section of a shock tube is partly constructed of the same pipe as the test section, but also includes a transition section as the diameter is reduced to a 16mm internal diameter pipe. This smaller diameter pipe was of a length of approximately 0.85m, while the transition section was approximately 67mm in length. Sensors were included along the length of the driver at the following approximate offsets from the driven end of the tube: 297mm (P1), 811mm (P2), and 1297mm (P3). Two additional sensors were located at the mouth of the testing section at offsets of 100mm (P5) and 350mm (P4). Sensors used were PCB 113B22 pressure sensors in the larger diameter tube, and PCB H113A22 and PCB H113A34 in the smaller diameter tube. The shock tube at the test site is shown overleaf in figure 36, whilst dimensions and sensor positions can be seen in figure 37.

Figure 36: Shock tube mounted at farm test site (smaller tube secured with ratchet straps, larger tube was not part of the experiment). Left image shows the shock tube driver section, whilst right image shows the test section and sample mounting region. The shock tube was designed by Aber Shock and Detonation Research Ltd. who also provided the test site and consumables and operated the equipment. Preparation and transportation of the tube and related equipment for testing was aided by a team of post-graduate students from Swansea University. The mounting system for the tube and sample is a custom integrated design.
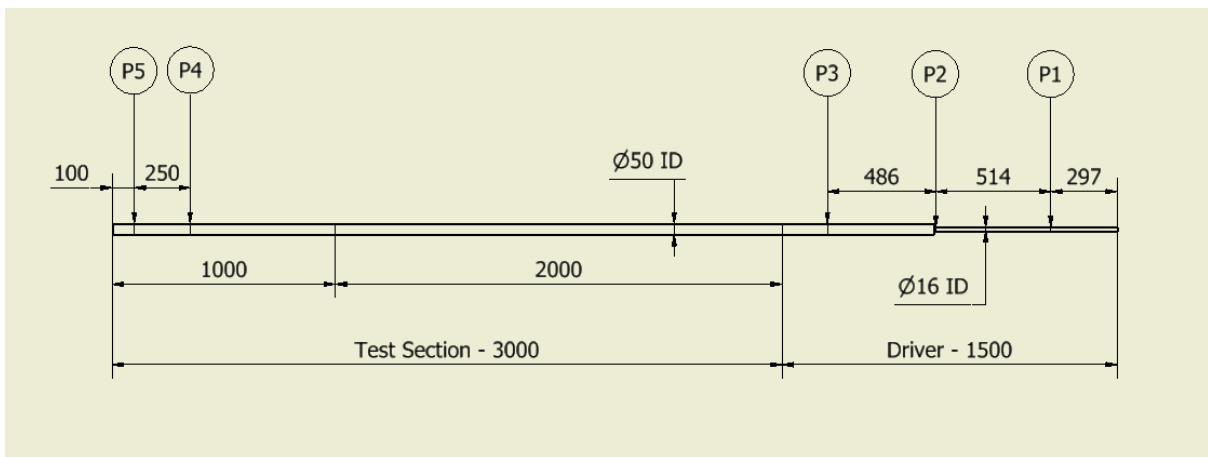
Figure 37: Diagram of the shock tube dimensions and sensor locations. Internal diameter (ID) of the shock tube is noted along with approximate lengths and positions of sensors (transition section of approx. 67mm length at pipe diameter change not shown on diagram).

The purpose of the driver section is to generate the pressure required to simulate a blast wave. This is done by filling the driver section with a gas mixture to a required volume which is ignited to cause a rapid expansion of product gases. The driver section is separated from the test section by a diaphragm, in this case Melinex polyester film of 0.5µm thickness, which ruptures when the pressure exceeds a specific magnitude. This system confines the gas mixture to the driver section until a suitable pressure is reached after ignition and the product gases are allowed to propagate through the test section as a simulated blast wave. The gas mixture used for this experiment was propane oxygen using N1.5 (95%) purity propane. Filling of the system was controlled via a MKS mass flow controller (model 1179A24CS1BV).

Data was recorded using a Fylde amplifier, Spectrum data recorder, and SBENCH software for all sensors. Data was exported to ASCII format for processing in MATLAB. Sensors used in samples

were PCB 113B22 piezoelectric pressure sensors, as specified in the previous chapter. These are the same model of sensor used in the larger diameter tube. These sensors have a high upper limit for testing of 34475 kPa with a sensitivity of approximately 0.145 mV/kPa. This makes them highly suitable for blast testing. Preliminary tests were completed by Aber Shock with these sensors in the P1 and P2 positions shown in figure 37 to confirm their functionality. Samples to be tested included a PCB pencil probe to take measurements of the static pressure produced at the end of the tube, the cylindrical model, and the additive manufactured thorax models discussed in the previous chapter.

7.2   Mounting Systems of Experimental Components

To ensure a suitable environment for the blast loading of the sample, a mounting system needed to be designed for the shock tube and he samples to be tested. Previous chapters have discussed how the physical models produced incorporated pins that could be used to secure the model to a larger structure. This was incorporated into the mounting system designed for the shock tube. The mounting system with shock tube attached can be observed in figure 36 above.

To mount the shock tube, the mouth of the tube needed to be suitably far enough away from any surface to prevent reflections being generated by the environment and causing additional loading of the sample. This meant that the shock tube needed to be a raised away from the ground by a distance which was advised to be at least 0.75m.

The shock front magnitude was expected to decay with a cube root relationship to increasing distance from the mouth of the tube (evidenced by equation 9 in chapter 1). This meant that the sample would have to be positioned close enough to receive a desired blast load whilst being distant enough to limit reflections that may occur from waves propagating back and forth between the sample and the mouth of the tube. From preliminary simulations completed by Aber Shock, it was deemed appropriate to position the sample 0.5m away from the end of the tube. However, it was possible to have the capability to adjust this distance if required by utilising a rail system to mount the sample.

Threaded rods were incorporated into the design such that a pair of adjustable bridges could be used to position the sample at a desired offset and secured with nuts. The bridges included ports to receive the pins built into the thorax models and secure them with bolts. As previously discussed, the pins were semi-circular in cross section to prevent global rotation or translation of the model. An alternative bridge was created incorporating a pipe clamp to hold the pencil gauge. The system included two positions in which samples could be secured, the primary testing position axially aligned with the shock tube, and a secondary position normal to the axis of the shock tube. The intention of this second position was to secure the pencil probe here during testing of the main samples as a reference that all tests performed were equivalent.

Images of all bridges and the threaded rod rail system are shown in figure 38 below, including both sample positions. The arrangement of the threaded rods was chosen to minimise the number of rods within the region between the mouth of the tube and the sample to limit interference with the loading whilst still providing suitable rigidity.

The main structure of the mounting system was constructed of mild steel square hollow section. This was divided into several sections forming the horizontal 'spine' (100x100x6mm) on which the tube could be mounted and several legs (50x50x3mm). All these parts could be bolted together using threaded rod and nuts for ease of transport and interchangeability. The length of the mounting system could accommodate extension or reduction in the shock tube length if required. The shock tube was secured to this structure using ratchet straps connecting flanges on the tube to the legs and spine sections of the mounting system. The entire weight of the system was deemed suitable to ensure the free-standing structure would not be displaced by the force generated when firing the shock tube. An assortment of wood was used as packing material under legs due to non-uniformity of the ground level of the field test site. Some minor excavation work was completed to improve the uniformity of certain areas. Drawings of the complete system are shown in figure 38. The parts required were produced by the workshop at MM Engineering from these design drawings.
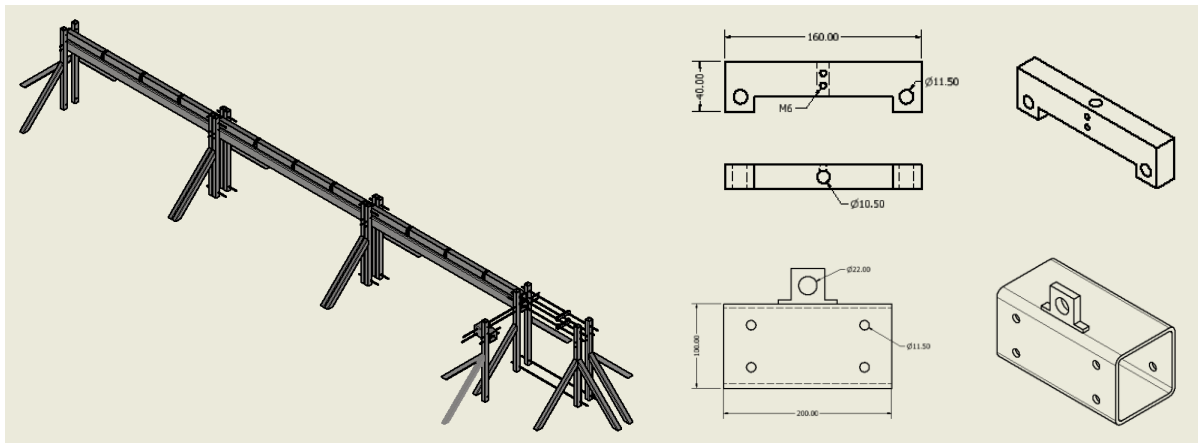
Figure 38: Diagram of the mounting system design. System was intended to be free-standing, be divisible into sections if required to extend/reduce the overall length, be constructed of interchangeable parts which require few/no specialised tools, be transportable via commercial van hire, include integrated mounting solutions for the samples to be tested, and be of a sufficient weight to withstand firing of the shock tube. The complete system is shown on the left, whilst the mounting systems are shown in greater detail on the right.

7.3   Blast Loading of a Pencil Probe

The first sample tested was the pencil gauge, referred to as sensor P6. This was secured in the axial testing position and exposed to several blast tests on each test day. Figure 39 shows the pencil gauge in position. This testing was focused on assessing the blast loading that was being produced at the end of the tube based on the data from sensors P2, P3, P5 and P6.

Figure 39: Experimental arrangement of pencil probe in the primary position. Pencil probe is secured with a pipe clamp with grease applied to the sensor to mitigate thermal effects.

Pencil probe used was a PCB 137B21B free field pressure sensor. This had an upper range of 6895 kPa and an approximate sensitivity of 14.02 mV/kPa. This sensor was ideal for the pressures expected in this experiment. The diameter of the probe was 22.1mm and fit snugly within a 22mm diameter pipe clamp.

Initial tests returned poor results as the low temperatures meant that gas compression was insufficient and detonation velocity (based on the time of arrival and known separation between sensors P2 and P3) was not reached in the driver section of the tube. On the final days of testing the weather conditions were significantly improved and successful detonation was achieved (>1800m/s detonation velocity).

Further difficulties were encountered as readings from the pencil gauge indicated significant unrealistic under-pressures occurring several seconds after the initial peak(s). This was determined to be due to thermal effects generated by a fireball produced during testing. To mitigate this issue, the pencil probe (and all sample sensors exposed to the fireball) were coated in grease. An example of the under-pressure and the images of the fireball are shown in figure 40. Data shown in this figure shows progressive reduction of the under-pressure magnitude as grease was increasingly applied to the sensor. It should be noted that this section of the waveform occurs many seconds after arrival, long after the region of interest of the initial few milliseconds after wave arrival. Data in the region of interest appears to be unaffected by any significant errors.

The data recorded from the pencil probe for the final day of testing is shown overleaf. All following data presented is from the final day of testing when the best environmental conditions were available. For the pencil probe, two consecutive tests were completed successfully. As the samples to be tested will be held in the same position as the pencil probe, this measurement is representative of the static loading that is expected for the samples to be exposed to. Additionally, sensor P5 is shown overleaf as comparison of the pressure just before the shock front exited the tube. This data is shown in figure 41.
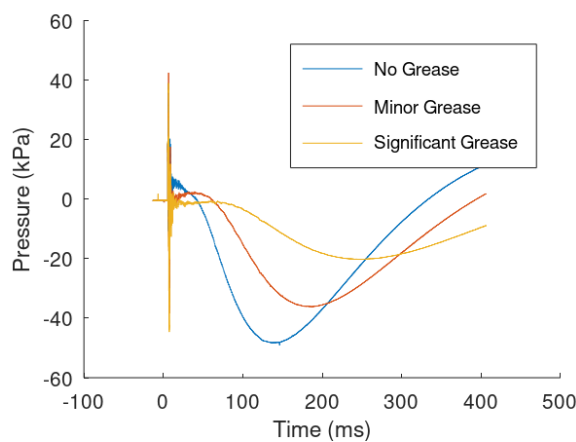
Figure 40: Frame of a recording of the test exemplifying the fire ball produced during testing (above) and corresponding recorded data from the tests. Data shown indicates that increasing the amount of grease applied to the sensor reduced the significant under-pressure observed several seconds after loading of the sensor. Although this data is not part of the region of interest, it indicates loading continues to occur long beyond the scope of this analysis.

The data shown in figure 41 is that a peak pressure of approximately 82kPa was being recorded at the mouth of the tube, which rapidly decayed to approximately 20kPa on arrival at the pencil probe 1.3ms later. Significant decay occurs over approximately 0.6ms, followed by a second positive peak greater than the first (approximately 33kPa). The initial peak has a rise time on the order of microseconds, but this second peak is much slower, occurring over 100s of microseconds.

The cause of this second peak is uncertain but is possibly due to the box section used for mounting the pencil gauge presenting a surface that would cause increased reflected pressure by confining the air in this region. This surface area was required for using the same mounting bridge in both the primary and secondary testing position. This error should have been designed out of the system by using differing mounting bridges for each position. The second peak does not occur in the mouth of the tube so is not due to any effects occurring within the tube. This will be discussed further in analysis of the thorax models, or for further visualisation see figure 48 in chapter 8.2. The presence of the second peak leads to a total duration of overpressure of 1.3ms. From the Kingery Bulmash methodology,

reflected pressure corresponding to the initial peak is expected to be approximately 43kPa. For the second peak, reflected pressure would be expected to reach 74kPa.

Following the second peak there is a significant under-pressure roughly equalling the magnitude of the over pressure of the second peak (-33kPa). This also occurs over a similar duration to the second positive peak. This seems akin to the negative phase in idealised blast loading, in which air particles are pulled back towards the space they have been forced out of, but the negative magnitude is significantly greater compared to typically expected. Negative magnitude expected would be much less than the positive overpressure and occur over a longer duration.

Finally, pressure returns to atmospheric levels until a large under-pressure is observed (shown in figure 40). This occurs after several seconds of testing so is not part of the timeframe of interest (<10ms duration of loading). This under-pressure was proven to be at least partly caused by the thermal effects of the fireball produced by the tube. Other contributing errors could include displacement of the pencil probe or loading of the wires due to collisions with the mounting structures. These errors are unlikely to be present during arrival of the shock wave as they would be expected to occur over much longer durations and because the repeated test produces near identical waveforms. Results would be expected to differ significantly if effectively random errors such as these were dominating the response.
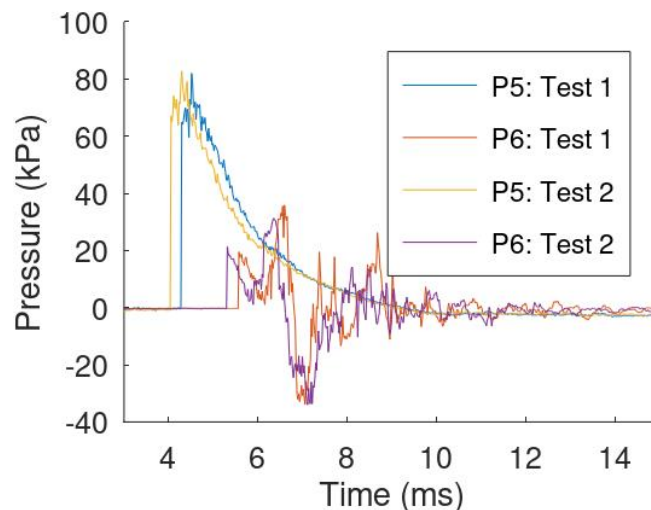
Figure 41: Static pressure histories recorded using sensors P5 (mouth of the shock tube) and P6 (pencil probe). Data shows that the test is highly repeatable with the most significant difference between tests being the time of arrival of the wave. This difference is likely due to slightly different detonation characteristics which could not be controlled more precisely (i.e., external temperature).

All data presented shows that the test is highly repeatable. Whilst the loads are significantly reduced compared to the expected threshold of injury loads, the wave propagation physics is expected to be consistent, and the rate of loading is accurately captured for a blast scenario. It should be noted that

the duration of the positive phase (1.3ms) is close to that of a near field blast as defined in chapter five (2ms). This means small strains and relatively high strain rates are expected as assumed in previous chapters.

It should be noted that recorded static pressure waveforms (33kPa peak, 1.3ms duration) are significantly reduced compared to values identified for the threshold of injury (200kPa peak, 2ms duration, or 85kPa peak, 10ms duration). Due to the pressure magnitude being far below the magnitude expected for the threshold of injury and the anticipation of small strains, damage to the models is not expected to occur. This means the models can undergo repeated testing.

Following these tests, the pencil probe was moved to the secondary position. Data recorded in this position is not expected to be equal to the axial position as the shock front is not expected to expand hemi-spherically immediately after leaving the tube. Instead, this position was used to show that all tests were producing external pressures that were equivalent to each other. Results taken in this secondary position were consistently and considerably reduced compared to the primary position, as expected. A similar comparison was performed using sensor P5 for pressure at the mouth of the tube. Results are shown in figure 42 for the tests completed using the cylindrical model and each thorax model.

Results show that there is no significant difference between the static loading produced in each test. The pressure at the mouth of the tube continues to reach a range between 75kPa and 83kPa, while the pencil probe records a peak of approximately 6kPa. The reduction in pressure is likely due to the pencil probe experiencing only the edge of the wave produced by the tube. The shock front is expected to develop into a planar wave within the shock tube which would exit the tube with velocity acting in the axial direction. Whilst expansion will occur, it will not be immediately hemispherical.
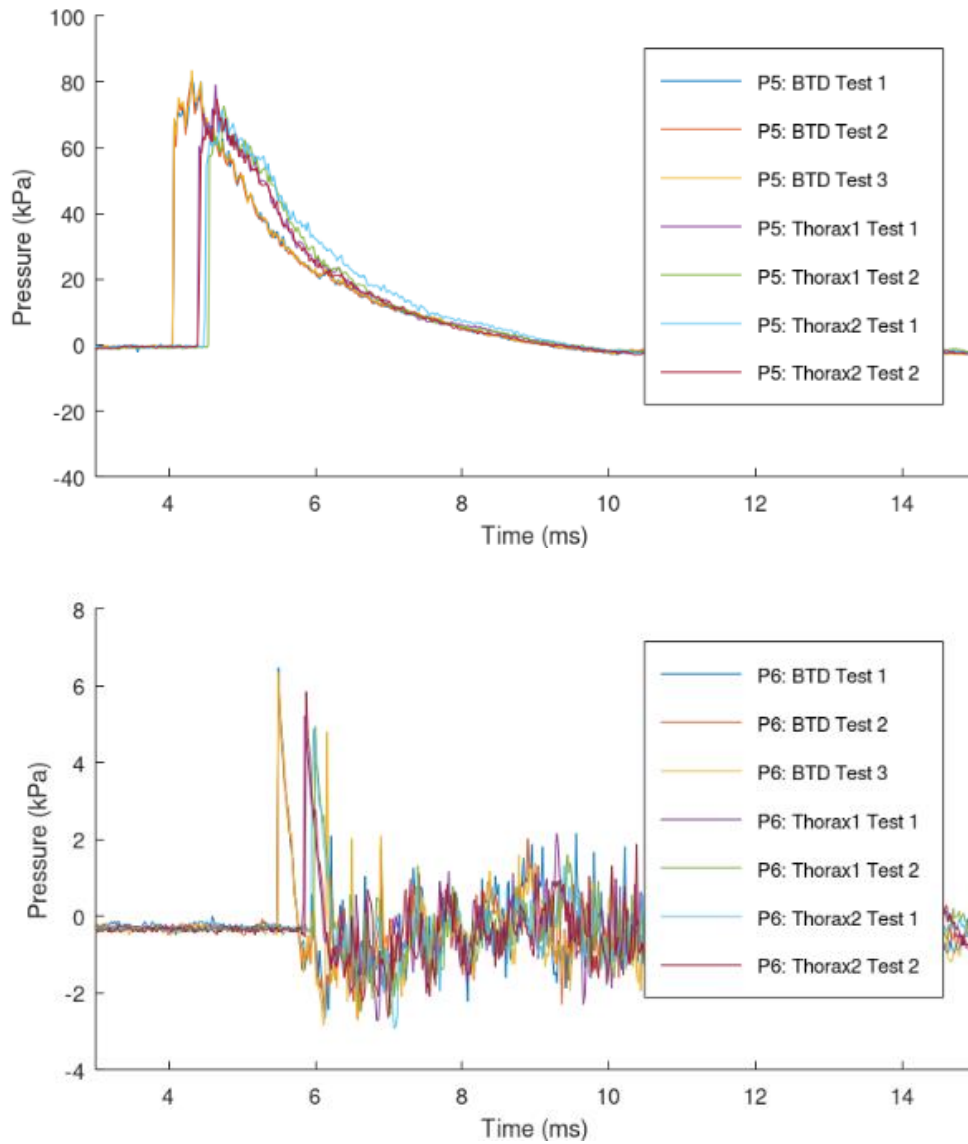
Figure 42: Comparison of static pressures measured in all tests. Sensor P5 is located at the mouth of the shock tube and P6 is the pencil probe in the secondary mounting position. Significantly reduced pencil probe readings are due to being in the secondary position and only being exposed to the edge of the wave produced by the shock tube. Consistent results show no significant deviation occurred in any test which was highly repeatable. Latter tests arrive later with a small reduction in peak pressure as the environment became colder and wetter, reducing the detonation velocity acquired.

8. Experimental Shock Tube Loading of BTDs

8.1   Blast Loading of a Cylindrical Model

The second sample to be placed in the primary axial position was the cylindrical model. This included three sensors labelled P7, P8, and P9. These sensors will also be used in the thorax models in the following section. Figure 43 below shows the arrangement of the sensors on an image of the sample secured in position. Sensor P9 was expected to return a value of reflected pressure, sensor P8 was expected to return a value close to that of the pencil gauge (i.e., a static pressure), and sensor P7 was expected to record the drag pressure generated at the rear of the model. These correspond to the Axelsson methodology sensor locations assuming that pressure on each side of the model is equal. Pressure waveforms recorded are shown in figure 44. Wires were secured using tape to reduce their movement during testing and the potential for collisions with the mounting structures.
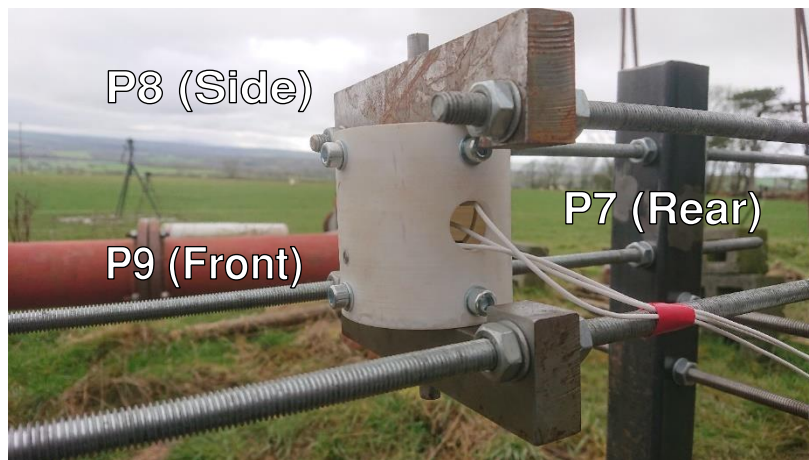
Figure 43: Experimental arrangement of the cylindrical model secured in the primary position. For this arrangement, the pencil probe was present in the secondary position. Wires were secured to the threaded bar to limit motion and collisions with structures which may interfere with the signal received. Sensor locations are labelled at the front, side, and rear of the cylinder, though only P9 is observable in the image. Sensors are flush with the curved surface and offset vertically to accommodate their length within the cylinder.
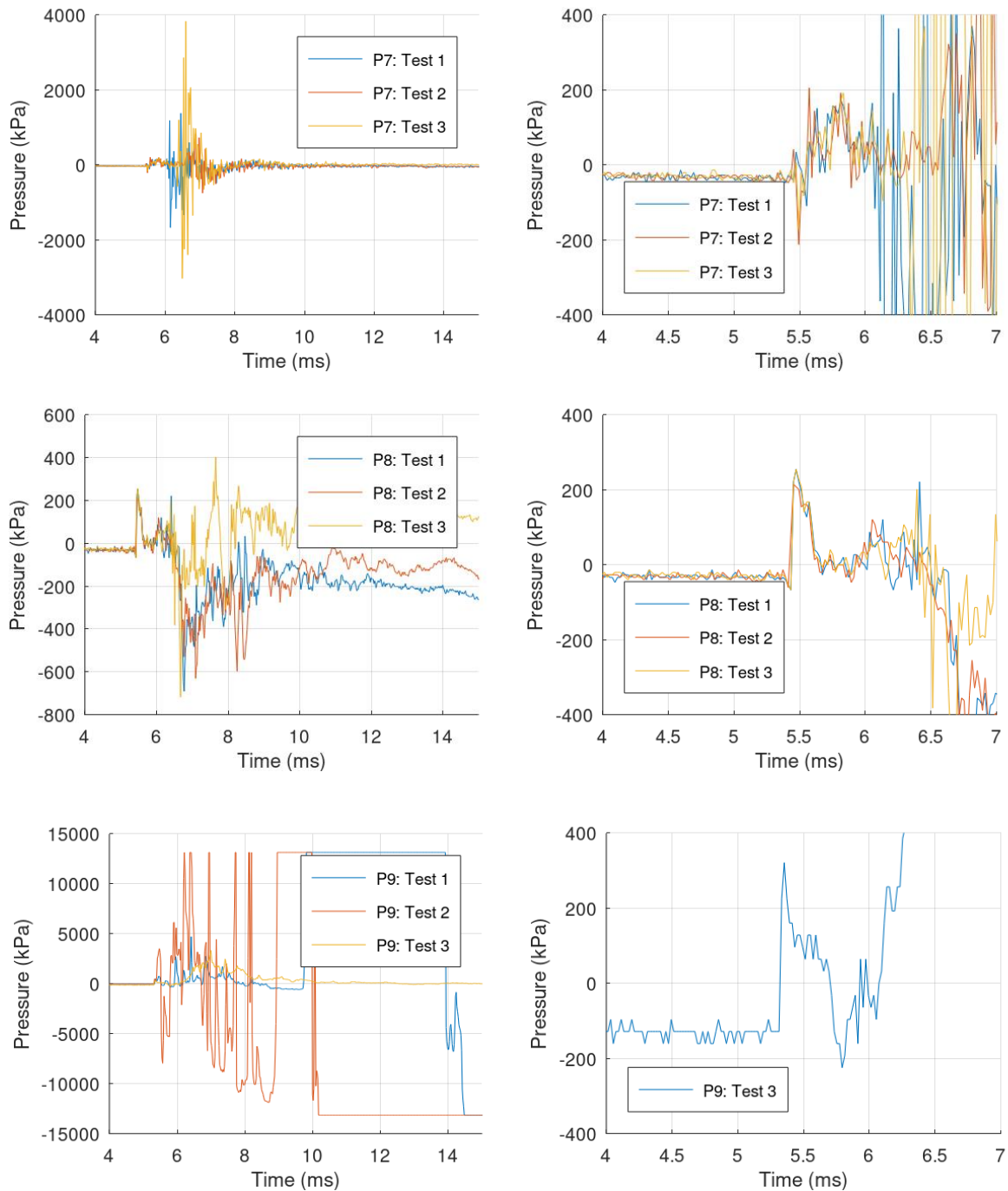
Figure 44: Data recorded from each sensor in the cylinder model over three tests. The full dataset is shown on the left and a region of interest is shown on the right. Most data recorded was realistic for approximately 1ms before unrealistic oscillating peaks with magnitudes greater than 1MPa were acquired (likely due to loading of the wires and reflections due to the mounting system). P9 recorded very poor data except for the final test. The cause of this error is uncertain, but the data is clearly unrealistic (supposedly exceeding 1MPa). Realistic data recorded before the 6ms timepoint shows suitable peak magnitudes relative to each other with overpressure durations of around 0.7ms. Where data reaches an extreme magnitude recording of data is limited by the software/hardware, leading to appearance of clipped data. This is an error in experimental data recording.

The data shows significant oscillations as the data was interfered with by noise after approximately 1ms of recording useful data. This is believed to be caused by loading of the wires, excessive vibrations, and possibly movement of the sensor. Regardless of the cause, the errors have obscured the data beyond the initial peaks, causing the raw reading to exceed allowable limits of the recording equipment and appear as though the data has been clipped. Peaks recorded were significantly higher than expected based on the pencil probe analysis. Static pressures of 33kPa would be expected to produce reflected pressures of approximately 74kPa. Instead, P7 recorded a peak pressure of 192kPa and P8 recorded a peak pressure of 255kPa. Data for P9 was particularly obscured by noise, however one clear waveform was obtained which showed a peak pressure of 321kPa.

Whilst these peaks show increased pressure at the front of the cylinder with reduction around the circumference as expected, it is notable that P8 is not recording a static pressure representative of the reflected pressure acting on the front of the cylinder (P9). All sensors are recording peaks differing by approximately only 50kPa. Furthermore, the duration is seemingly reduced to only 0.7ms of overpressure and the second peak observed in the pencil probe data does not seem to occur. Though the second peak would be difficult to detect due to the unrealistic oscillations following the initial peak, this could be confirmation that the second peak was caused by reflections from the mounting system. The removal of these reflections would also facilitate clearing of the pressure and potentially explain the reduced duration of overpressure.

Despite the errors and unexpectedly high magnitudes observed, these results provide knowledge of the loads expected to be acting on the exterior of the thorax models.

8.2   Blast Loading of Physical Thorax Models

Finally, the two thorax models were tested. Arrangement of sensors P7, P8, and P9 are shown in figure 45 along with images of the samples secured in position. Notably, sensor P7 is the same position for both models and should be directly comparable. It was noted that loading of the wires was a potential issue which may affect the pressure recordings. When securing the sensors, ultrasound gel was used to ensure suitable contact between the thorax model and the sensor head and accommodate effective wave transfer across this boundary. Results from the testing are shown in figure 46.

Figure 45: Experimental arrangement of the thorax models in the primary position (rear view). The left model is referred to as the propagation model, the right is referred to as the scatter model. Sensors are indicated on the images with sensor P7 notably being in a consistent position in both samples. In the second thorax model, there is significantly increases embedment depth of sensors P8 and P9, the latter of which can be faintly observed in the image. Wires were secured to the threaded bar to limit motion and collisions with structures which may interfere with the signal received.
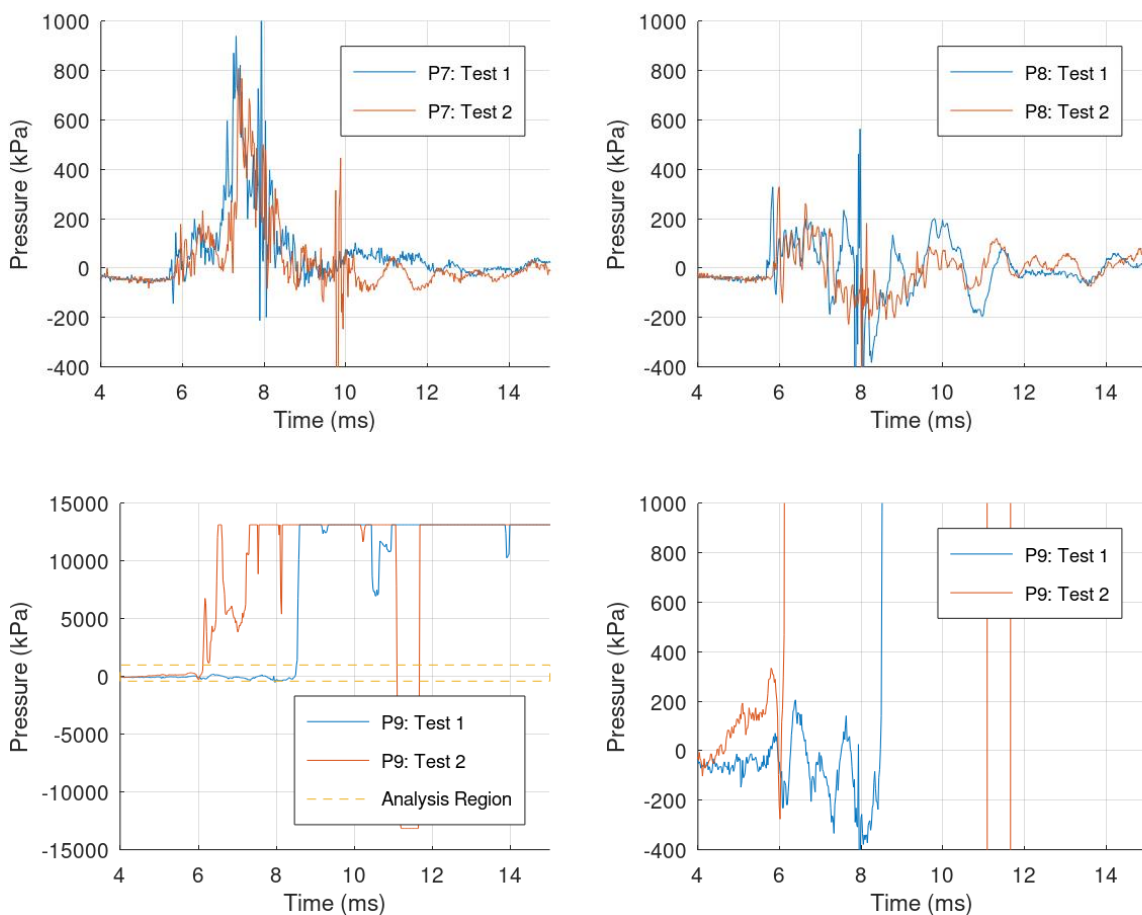
Figure 46: Experimental data recorded from the first thorax model. Whilst long duration data is unreliable, initial peaks seem accurate due to the high similarity between consecutive tests. Data is shown between 4ms and 15ms after detonation. Sensor P9 recorded unrealistic data (>1MPa) but did seem to record an accurate initial peak. Where data reaches extreme magnitudes and appears clipped is where data exceeded limits of recording systems (error likely due to sensor movement).

Sensor P7 recorded an initial peak of approximately 200kPa. This reading oscillated with increasing magnitude before a second rapid rise in pressure to a new peak of around 900kPa approximately 1.5ms after the initial peak. As the data between tests is consistent both peaks are likely realistic.

It was considered that the second peak could be due to loading of the sensor housing causing a rotation that increased the measured pressure. If this mechanism is present, it would be expected to be evident on both sensors P7 and P9 in analysis of the second thorax model. To minimise this mechanism shielding would be required to prevent the sensor presenting an unobstructed surface to the mouth of the tube.

However, this macroscopic motion would be expected to occur over a longer timescale than analysed. Within only a few milliseconds of loading beginning, only the wave propagation dynamics would be expected, particularly as the second peak then decays to a baseline value. This implies that sensor P7 is recording reflections scattered by the mediastinum. This remains in agreement with the analysis presented in figure 17 where stress concentration can occur in this region of the thorax to create the batwing pattern of injury.

Sensor P8 recorded a peak of approximately 330kPa. This then alternated between -200kPa and 200kPa with decreasing magnitude and durations. As near-identical waveforms are produced in both tests for sensors P7 and P8, this indicates that the data is reliable and permanent damage to the model is unlikely to be occurring.

Sensor P9 recorded erroneous data in both tests. Initial peaks of 200kPa and 300kPa can be identified, but then loading becomes unrealistic. Notably, the magnitudes differed substantially between the tests, making this data less reliable. The reasoning for these errors is uncertain, but it is possibly due to malfunction with the instrumentation which could be sensor or wire related, or due to extreme motion of the sensor (i.e., large vibrations). This is particularly feasible as the relatively soft Agilus-30 is far from a rigid surface which can be mounted to. Deformation of material is expected to correspond to sensor displacement and incur erroneous data readings. It is possible this could be mitigated by mounting the sensors to the ribcage material instead as a more rigid material.

Most interestingly, the initial peak pressures recorded inside the thorax were roughly equal to the peaks observed acting around the cylinder model (the external pressure expected to be acting on these models). This implies that the entirety of the external load was acting on the internal structures. This was not the expected result, which was to see a reduction in pressure acting internally.

From simulations of the biological material models of the human thorax (see chapter 5), a reduction of peak pressure of at least 85.0% was expected based on peak minima stress recorded in the lungs in the far field simulations (96.4% for the near field simulations). However, the material assessed for the physical thorax indicated that Agilus-30 and Agilus-706B may be very similar to each other, so a

transmissivity closer to unity would be expected. This means the equal internal and external pressure measurements do not necessarily discredit the original hypothesis of boundary interactions dominating the internal loading. Further testing with larger samples, alternative materials, and improved data recording would be required to form a suitable conclusion.

It was also expected that sensor P8 would return a reduced magnitude compared to sensor P9 as it was distal to the mediastinum. Problems with recording data with sensor P9 makes this difficult to determine, however, the initial peaks indicate both sensors experienced very similar loads. This could be due to the proximity of the sensors enforced by the reduced scale of the model.

Data recorded from the second thorax model was significantly poorer, with all sensors failing to record waveforms for a reasonable duration for analysis. Sensors P8 and P9 present significant drift from the baseline of 0kPa gauge pressure before arrival of the shock front (expected around 5.5ms). Sharp rises in pressure corresponding to the expected arrival time imply initial peak pressures of approximately 400kPa and 325kPa respectively (i.e., change in pressure in the second test), but this data is highly likely to be inaccurate. Despite this, it should be noted that these magnitudes are greater than those recorded at the rear of the thorax, and P8 displays the greatest magnitude as expected (aligned axially to the direction of blast propagation). This supports the concepts of stress concentration which were also shown in chapter five.

Only sensor P7 recorded a reliable initial peak pressure of approximately 300kPa, increasing to almost 500kPa. It is possible that the increase in peak pressure from 200kPa recorded in the first thorax model is due to the presence of sensors P8 and P9 within the heart causing increased stiffness of the model and increased reflections directed towards sensor P7. This would imply that oscillations are being caused by the confinement of waves within the model leading to increasing magnitudes, which may be more significant than explored in the simulations when considering the reduced scale of the physical model compared to the simulated human thorax (i.e., there is a reduced distance between stiffer structures in the physical model).

It should be noted that sensor P7 was expected to return similar results in both thorax tests, but this cannot be fully investigated due to the data recording errors. Furthermore, sensor P9 returned very poor data so it cannot be confirmed whether loading of the sensor body was causing rotations that would effectively increase the pressure measured. These topics unfortunately remain unconfirmed.

As sensors P7 and P9 were aligned normal to the direction of blast propagation, it is possible that loading of the sensor would have caused significant motion and errors in the recorded results. It is clear from all results that vibrations are a significant factor in obscuring the results. In the thorax model the soft material means the sensors cannot be assumed to be secured rigidly, which is likely causing the poor record of results beyond initial peaks. This issue would have been most prominent in sensors P7 and P9 of the second thorax model, which correspondingly exhibits the worst recording of

data (almost all data being unrealistic, magnitudes greater than 1MPa, or exceeding the limits of recording capabilities). As discussed earlier, this could be rectified by introducing shielding of the exposed sensors or mounting using a more rigid material (such as to the ribcage). Results for the second thorax model are shown in figure 47.
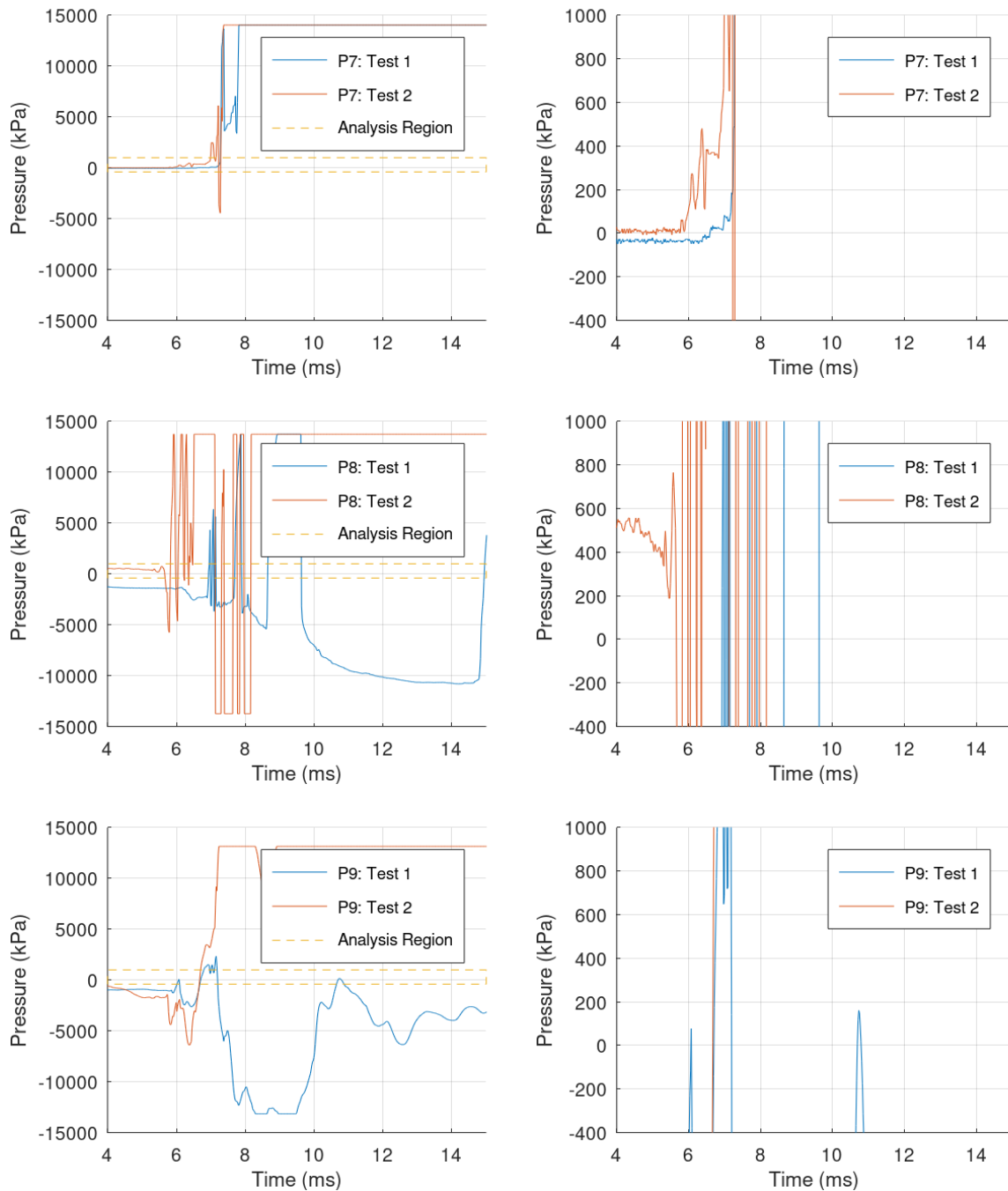
Figure 47: Experimental data recorded from the second thorax model. Data from these tests was consistently poor, with the only reliable data is the initial peak recorded by sensor P7. All other waveforms exhibit various errors, the most prominent being excessive magnitudes which stem from experimental errors. Data is shown between 4ms and 15ms after detonation. Full pressure ranges are shown on the left and regions of interest are shown on the right. Unrealistic data (>1MPa) is observed in all traces and most exhibit errors associated with sensor motion (magnitudes beyond recording limits).

Another interesting observation during experimental testing of the thorax was visual capturing of the loading because of the poor weather conditions. During the final tests falling snow allowed video recording to physically show the propagating wave, including the apparent repeated loading observed in figure 41. Stills from the video are shown below in figure 48, but this is better observed in the animated figure found with the following DOI: 10.6084/m9.figshare.25602057. No quantitative analysis can be completed with this data, but it serves an interesting visualisation of the physical phenomena of shock front propagation, reflections, and the testing carried out.
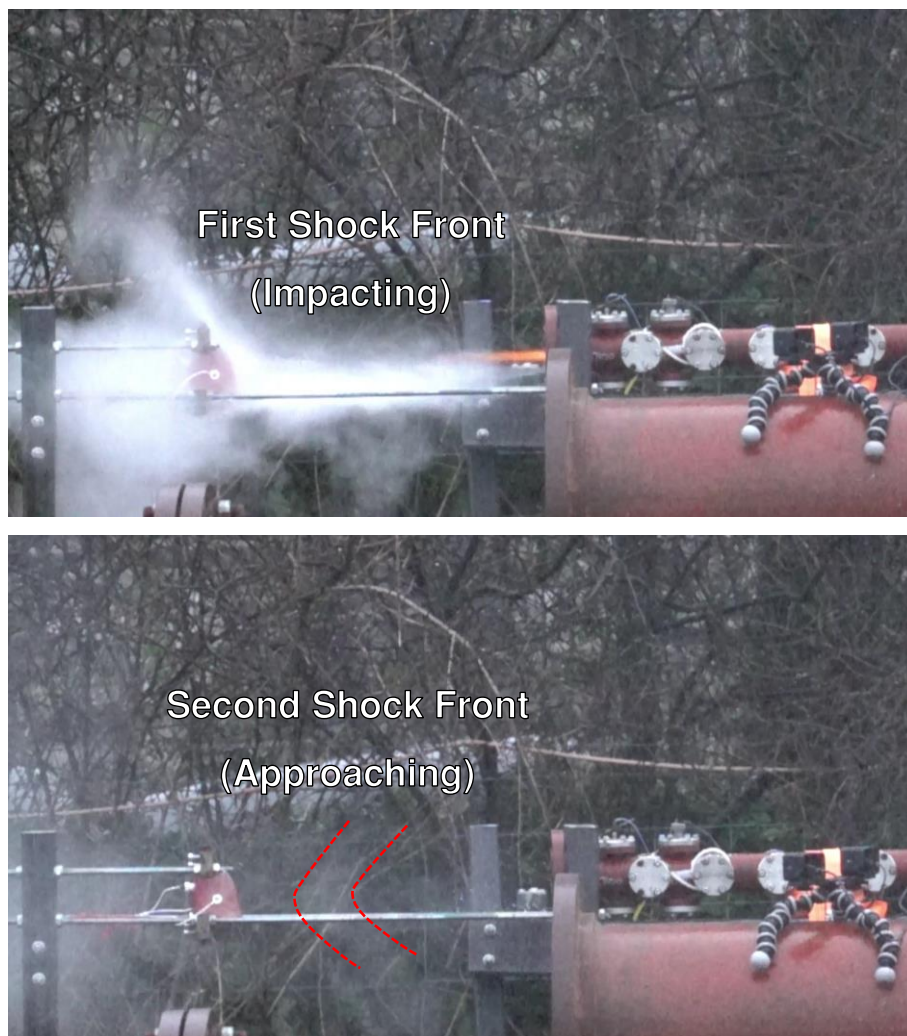
Figure 48: Experimental shock tube loading of a thorax model in poor weather conditions (snowing). Note the unintended visualisation of the shock front. Top image shows the initial wave, while the bottom image shows a second wave approaching the thorax. This also illustrates the complications of testing in poor conditions where the snow itself may have influenced the loading of the thorax. An animated version of this figure is much clearer and even shows a third reflection being generated which cannot be distinguished in still images. The animated figure can be found with the following DOI: 10.6084/m9.figshare.25602057

8.3 Summary of Experimental Analysis

In conclusion, the findings that corroborate the initial hypotheses is that the initial reading from sensor P7 is reduced compared to sensors P8 and P9 in all tests. This is possibly due to sensor P7 being distal to the mediastinum which was expected to cause proximal stress concentration due to stress wave reflections. Development of a second peak is possibly representative of reflections from the mediastinum reaching this region, which is more likely in the reduced scale model as the edges of the lungs are closer the mediastinum. Simulations of a reduced scale model were unsuccessful due to instability stemming from the required reduction in element size and corresponding reduction in time step size.

Unfortunately, the concept of stress concentration occurring proximal to the mediastinum could not be confirmed with comparison of sensors P8 and P9 within the analysis of the first thorax model as they returned similar peak pressure magnitudes. Sensor P9 was expected to be on a pathway with increased proximity to reflecting structures and exhibit slightly increased peak magnitudes, but the proximity of sensors may have obscured this data. Although the data for the second thorax was poor, analysis showed greater stresses recorded around the mediastinum than at the rear of the thorax (comparing sensors P8 and P9 between thorax models).

Finally, it should be noted that the internal pressures were expected to be significantly reduced compared to the external loads, but this was not the case. Instead, internal pressures approximately equalled the external loads when analysing the initial peak recorded. This may be due to the reduced scale of the model, or possibly a result of the internal reflections.

It is highly likely that vibrations and sensor movement is causing the poor record of results at longer durations. For any future testing using this methodology is highly likely that alternative securing methods should be explored for the sensors focusing on measures to reduce vibrations. Initial peaks are deemed reasonable to analyse as the high sample rate allows accurate initial recordings before vibrations and potential macroscopic movement of the sensors to interfere with data collection.

8.4 Potential Improvements to Test Methodology

Time constraints meant additional testing could not be carried out. Additional tests would have been very beneficial for mitigating the errors observed. Improvements for the testing methodology would have included: 1) alternative mounting bridges for the pencil probe to reduce the surface area available for reflections presented near the sensor, 2) inclusion of shielding to prevent/reduce the blast acting on sensor wires and sensor bodies which is believed to have caused significant noise and erroneous data recording throughout testing, 3) adjustment of the secondary testing position to be closer to the primary position (to receive complete impingement of the produced wave), and 4)

reduction of the instrumentation of the thorax models to reduce the likelihood of sensors interfering with each other (either by increasing the size of the thorax or reducing the number of simultaneously mounted sensors). Additionally, the testing should be completed in warmer weather where issues of detonation velocity could be more easily avoided. Wet conditions (rain and snow) should also be avoided if possible as these factors likely also hindered accurate data collection.

The most important factor to reduce would be vibration and the potential macroscopic motion of the sensors. This would require further investigations into the mounting methodology of the sensors which may be difficult to avoid due the soft material used to mimic human tissue. Artificial extension of the ribcage geometry may be suitable to create a threaded section able to secure the sensors more rigidly (i.e., using Vero material instead of the softer Agilus-30). Alternatively, whilst shielding could be implemented simply to divert blast away from wires and the sensor body, it could instead be implemented as a jacket enclosing the sensor. This would limit the load transferred to the sensor by preventing direct loading of the sensor and reduce global motion of the sensor by providing support/more rigid mounting.

Alternative sensors could also be utilised such as thin film pressure sensors or hydrophones as used by Boutillier et al in experiments on blast loading of swine [50]. This would change the instrumentation methodology entirely. The experiment could also be made more like Boutillier's by securing the thorax model with a backing plate (i.e., changing the mounting method). This may reduce vibrations, but most importantly it would adjust the loading conditions further from an open-field scenario (the intended scenario to replicate) and closer to a scenario with a reflecting wall (see chapters 1 and 2, Bowen and Bass studies [32, 34], or figures 9 and 10 for illustration of how these scenarios differ). Changing the loading conditions in this way would require significant re-consideration of the results that would be expected.

Whilst these modifications may not completely resolve the difficulties and errors encountered during the experiment, they would certainly help mitigate them. It would also be desirable to complete additional tests at variable offsets or with varying shock tube configurations. Ideally, longer duration waveforms would be desired with greater peak magnitudes which possibly be achieved with varying position or shock tube construction. Whilst the framework of the experiment allowed for this, time constraints did not. The framework did not allow for rotation of models within the region of interest as it was not included within the scope of the experiment. This would certainly be a desirable aspect of the model to investigate but would require many more samples to be designed with differing instrumentation patterns (alongside a significant overhaul of the mounting methodology).

9. Proof of Concept Studies

9.1 Environment Variation

This chapter concerns studies that underwent some initial development but did not culminate in complete analysis. These can be considered proof-of-concept studies, outlining methodologies for further work. Many of these have been discussed in prior chapters as justification for using specific methods when constructing models. Part of the scope of works was developing an easily modified platform for these specialised studies which could integrate personal armour systems. Whilst the development of any armouring layers was not explored, integration would be as simple as creating a 3D model of the armour, assigning appropriate material models, and applying suitable contact conditions between the armour and the thorax model.

A major topic of interest with or without armour being integrated is the variation of the environment in which the thorax exists (i.e., adjusting the complexity of surrounding geometry and the orientation of various structures within it). The CEL method utilised is advantageous in that the thorax model can easily be rotated within the Eulerian domain for investigations on the effects of direction of loading. Such investigations are already present within the field [6, 39], but are not common. Figure 49 shows an example of stress results varying with rotation of the computational model produced in this study. The key result shown here is the increased reflected pressure magnitude when a larger surface area is presented to the blast source (illustrating the effects of pressure clearing).
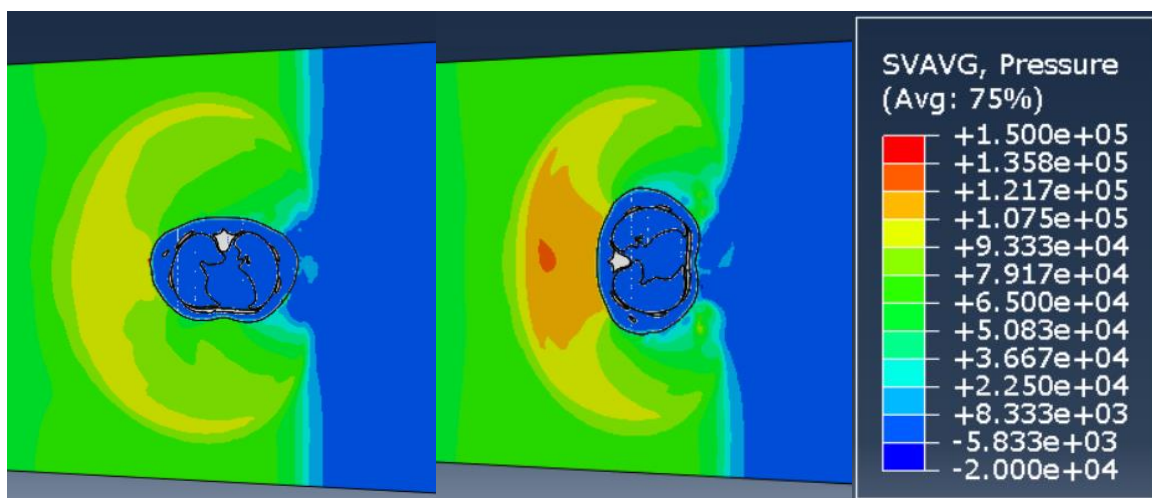

Figure 49: Example diagrams of simulations of the computational thorax model rotated through 90 degrees (left) and 180 degrees (centre). Legend for blast pressure is shown on the right, internal thorax pressures are not shown. Units of pressure are in Pascals (Pa).

Another advantage is that the model can be placed in a complex environment by including additional Lagrangian bodies such as a reflecting wall. This can be used to investigate the hypotheses of Bowen and Bass in-silico [32, 34], with an example shown in figure 50. In this preliminary simulation the reflecting wall is modelled as steel (effectively rigid) and a region of compressed air can be seen forming between the two Lagrangian models, increasing the total pressure recorded in the air and thus the loading acting on the thorax. This could also be combined with investigations of orientation to further study the dynamics under differing yet simple conditions.
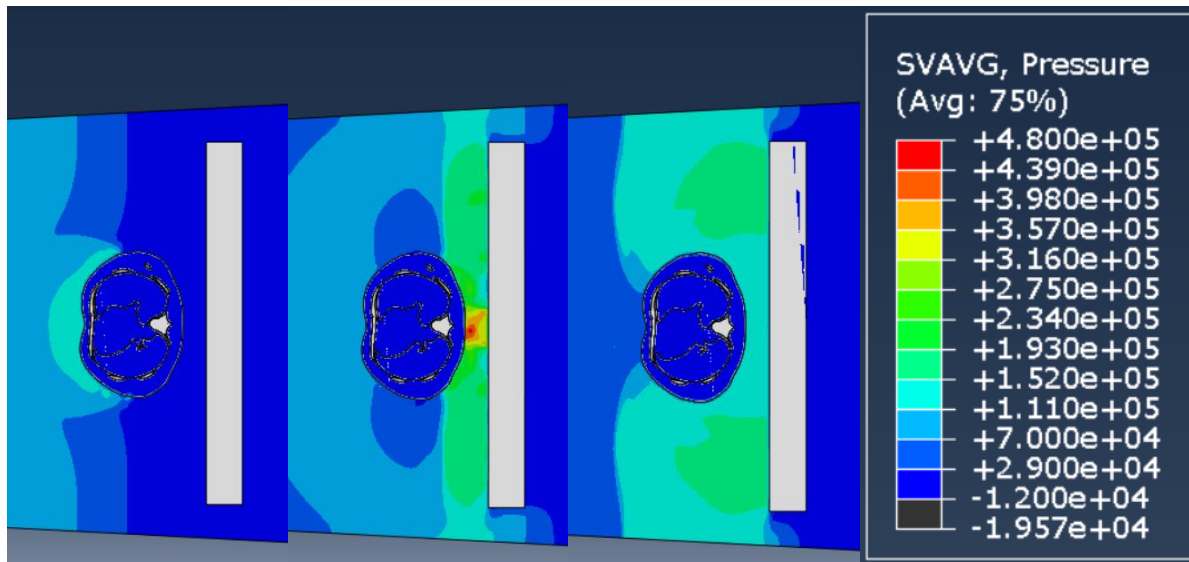
Figure 50: Time-lapse of a blast wave impacting the computational thorax model and a nearby reflecting wall. The reflections generated reach a higher maximum than in the open field scenario. The image on the left corresponds to the arrival of the blast wave with consecutive images corresponding to 0.5ms intervals after arrival. Units of stress are in Pascals (Pa)

Figure 51 furthers this concept by showing additional increased complexity of the environment with a multi-sided enclosure or a vehicle used as increased confinement. In the case of a vehicle or another fully enclosed structure, the armour material can be modelled as a hollow structure containing air in which the blast wave can be transferred to.

Figure 51 also highlights the opportunity to directly compare to Axelsson methodology by simulating a BTD in place of the thorax model. These models are easily interchangeable within the simulation. This also provides the opportunity to compare directly to experimental data recorded at blast testing sites such as Radnor Range which already utilise the Axelsson BTD in testing, including in scenarios such as within an armoured vehicle.
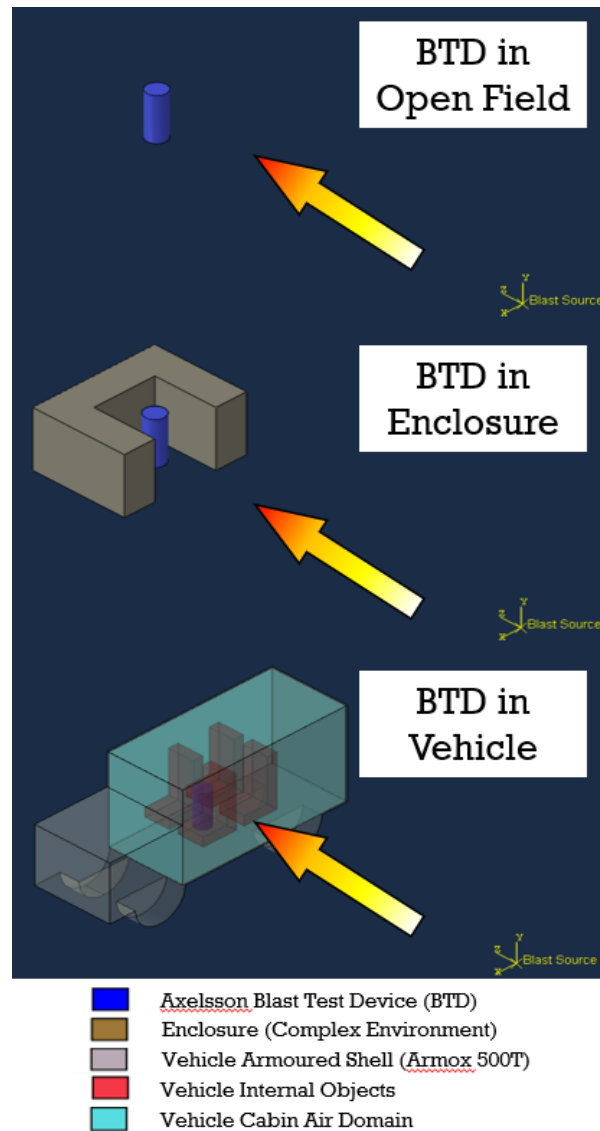
Figure 51: Examples of simulations of an Axelsson BTD in increasing complex environments. These simulations are constructed using the CEL methodology outlined without the Eulerian air domain for blast propagation shown. The BTD model can easily be replaced with the computational thorax model for in-depth analysis and comparison to BTD simulations. Effectively rigid obstacles can be modelled as steel.

Further to these variations in geometry, it should be noted that the studies in this thesis elected to focus on the threshold of injury but there would be some merit in investigation stress distributions at higher lethality levels. This would preferentially require a damage model to be implemented as rupture of parenchyma tissue would certainly lead to stress relief in the structure. This could be implemented in Abaqus by defining threshold values of stress beyond which elements (and associated contact conditions) are deleted. Alternatively, more complex models can be implemented using custom material modelling through the Abaqus VUMAT functionality.

9.2 Combined Injury Modes

Implementation of a damage model for all materials would also allow for investigation of the combined effects of primary and secondary injury. Secondary injury implies invasive penetration of a fragment into the thorax, which would require skin rupture. Investigations into this improvement would likely need to begin with identification of skin failure models and depths of penetration, which would likely best be guided by the work of Breeze et. al [7, 9, 56], experiments penetration into gelatine blocks [59], and the work of Del Linz et. al. [8]. Figure 52 shows an example of a simulation of a fragment simulating projectile (steel) impacting onto a block of material assigned biologically relevant properties (i.e., the tissue model used for the thorax). This type of modelling could be incorporated into the computational thorax model to simultaneously simulate primary and secondary blast injuries.
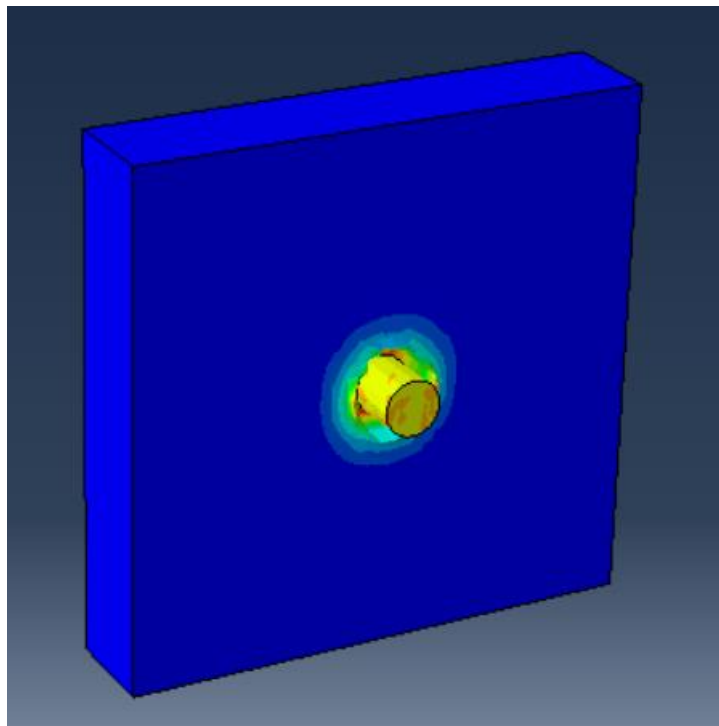
Figure 52: Example simulation of a fragment simulating projectile impacting a block with biological tissue properties applied. Contours indicate velocity. Accurate modelling of the penetration of the fragment into the tissue requires damage modelling to assess the depth of penetration. This is modelling of secondary injury, which could be incorporated into the existing thorax model to simultaneously assess primary and secondary injury.

As this thesis focused on the effects of primary loading and injury, this example simulation was not fully evaluated on whether the response was realistic. Correct and full analysis would require more in-depth study of the response of impact and penetration, culminating in analysis of the effects of combined primary and secondary loading. This all requires significant time investment to build functional individual models before combining them and introducing armour models/layers.

10.   Conclusions

10.1 Summary of Studies

Two key studies have been discussed in this thesis, 1) the computational investigations of PBLI using FE simulations, and 2) the experimental investigations using custom AM physical thorax models. Both of these models were designed to incorporate full 3D geometry of the human thorax. The importance of the 3D geometry is highlighted by comparison to the 1D wave equation which was identified as being unsuitable in isolation for injury prediction purposes.

To acquire accurate geometry of the human thorax, segmentation of CTs representative of the average male was completed. The geometry was then converted into meshes ready for simulation. This methodology is easily adaptable to examine alternative sexes or species or can be used to create bespoke personalised models. Versatility was a primary aim when designing the methodology to be used.

For loading the thorax models, theoretical blast loads can be calculated using the Kingery-Bulmash methodology, with specific expectations of injury magnitude derived from the commonly referenced lethality curves of Bowen and Bass. These methods were utilised to derive blast loads representative of several lethality levels, including the supposed threshold at which injury to the lung is first apparent. Whilst these blast loads are idealised, the models produced have the advantage of being capable of receiving realistic loads from complex environments (i.e., loading can incorporate multiple peaks and durations). The threshold of injury is highlighted as a topic of interest as it represents the level at which peak stresses are expected to be representative of tissue rupture.

Computational analysis of the threshold of injury was completed and stress metrics were explored for two scenarios. These were referred to as the near and far field scenarios, which correspond to short and long duration of loading. This was a topic of interest as there has been debate that injury levels can vary due to the dominance of impulse and stress magnitude in each scenario respectively. Analysis focused on identifying a consistent metric between the scenarios and various stresses were explored. Of these, the tensive stress provided a clear threshold value at which injury could be expected that was consistent for both scenarios.

Production of the physical thorax model was done via additive manufacturing (i.e., 3D printing). Materials selected were intended to mimic the behaviour of the biological tissues, with literature explored and a material characterisation study completed for materials of interest. This included the Agilus-706B material which is not traditionally used as a structural material, representing the first time its mechanical characteristics have been explored experimentally (to the extent of the author's knowledge).

The resulting physical model was printed using three materials simultaneously. Agilus-30 represented the soft tissues, Vero represented bones, and Agilus-706B was used to represent lungs. Printing the material simultaneously ensured encapsulation of the lungs within the anatomical geometry of the tissue and ribcage. Sensor ports were included for instrumentation, with two models produced. One was optimised for assessment of 1D propagation of the blast wave from the front to the rear of the lungs. The second model was optimised for identification of peak stresses in regions of high confinement. Both models were capable of detecting scattering from the mediastinum.

Whilst data recordings were heavily influenced by vibrations, some important results were obtained. These included evidence of reflections from the mediastinum, corroborating the hypothesis of wave propagation behaviour. Furthermore, as would be expected, greater stresses were recorded in regions of confinement (i.e., around the mediastinum). From the computational simulations of the biological human thorax, it was expected that the internal loads would be substantially less than the external loads. This was not the case in the experiments where they were approximately equal. This was attributed to the reduced scale of the thorax and the likely similarity of Agilus-30 and Agilus-706B. Whilst the physical thorax model requires further development, the computational model's proven success indicates it can be utilised in investigating further topics within the field of primary blast lung injury whilst undergoing further improvements itself.

Both the computational and physical models discussed in this thesis focused on attaining a deeper understanding of the mechanism(s) by which PBLI occurs. The key targets for these studies were outlined in chapter two. These are presented here for review:

1) a parameter/metric by which lung tissue rupture can be expected.
2) the specific location of injury for prescribed loading conditions.
3) the effect that variations in loading produce on the prediction of location, magnitude, and the mechanisms of injury.
4) Investigation of a method of experimental validation of internal loading of a model to corroborate estimates of mechanical magnitudes (i.e., peak stresses) used as indicators of injury.

The first of these targets was addressed via assessment of compressive and tensive stresses in the computational thorax model. Compressive stresses differed in the near and far field scenarios explored, indicating it would be a poor metric of injury prediction. However, a consistent tensive stress threshold of 8.7kPa was identified between the two scenarios implying that the rupture of tissue (particularly for this model) could be predicted at varying blast loads. This contributes to greater knowledge of the stresses expected within the lungs at the threshold of injury, which is a topic with limited exploration within the literature. The most commonly referenced injury prediction metrics

(Bowen [32], Bass [34], and Axelsson [35]) focus on the external loading for predicting lethality with no information on internal loads.

The use of tensile stresses as an injury prediction metric also serves to support the hypothesis that spallation caused by tensive stresses is the most prominent mechanism in instigating the rupture of lung parenchyma [3]. This is an important development for the field of study as there is little evidence corroborating this hypothesis available in the literature.

This same analysis identified that the computational model could predict peak stresses occurring in regions where known patterns of injury were expected. This was proven with a time-lapse comparison of stress contours with a CT of a real blast injured lung. The model injury patterns and the identification of the peak tensile stress injury metric is representative of success that homogeneous elastic material models capturing the wave propagation behaviour/interactions are likely adequate for exploring predictions of primary blast lung injury.

This is particularly important as the model has proven that stress concentrations at boundaries mimics the patterns of injury observed in blast victims. These findings also emphasise the importance of managing wave propagation physics when designing armour systems.

The third target has been partly addressed in the identification of a consistent injury metric between loading conditions at the threshold of injury level of blast loading. Further exploration of higher lethality levels was not addressed as a damage model would need to be implemented in the model to accurately capture the tissue rupture dynamics. Whilst this can be implemented in Abaqus CAE (and was briefly explored without a full study being completed) true validation of the model results would require experimental data. In particular there is a lack of experimental data available in the literature for blast testing due to ethical concerns, the difficulty in performing blast testing, and the difficulty involved with working with biological tissues. Even data on simplified high strain-rate material characterisation testing of biological materials is limited, with most being quasi-static or low strain-rate. To this end, the AM model was created and experimentally tested to confirm wave propagation characteristics. This was also the goal of the fourth target.

Whilst the data obtained from experimental tests was limited, the models produced successfully showed reflections occurring around the mediastinum being scattered towards the sides of the thorax and increased stress acting at regions of greater confinement such as near the mediastinum. This further supports the hypothesis that the wave propagation physics discussed is applicable to reality and can be used as an estimate for predicting injury.

Unfortunately, the experimental data was not suitable for deeper analysis of the expected injury level produced during testing due to significant vibrations limiting long duration data. This analysis would have incorporated Axelsson's BTD method (i.e., using the cylindrical model measurements to

determine injury level expected and compare to simulations of the AM thorax model materials). This was also limited by difficulty in acquiring stability of the reduced scale model in the simulation suite due to the reduced element sizes required. Nonetheless, the physical model produced presents a novel ATD which can be considerably improved via deeper investigations of the materials utilised in construction, completion of accurate simulations (using the computational methods outlined), investigations into the effects of scaling, and could even be converted into a physical analogue of injury if substituting materials with structures like lung (i.e., foams, or even excised lung tissue). This is a promising model for future development.

Both models discussed in this thesis provide versatile platforms for new developmental pathways, with ample opportunity for improvements in each, or lessons to be learnt if developing alternative models. Whilst the key targets have been partially addressed, there is still much to learn. These models have demonstrated preliminary success that can be developed much further. Future work should focus on corroboration of the conclusions of this thesis and further development of the targets outlined, which have considerable depths to be explored. This can be achieved by deeper analysis of the models' constitutive parts and expansion of the model into other known fields of study. The physical model requires significantly deeper assessment but provides a valuable opportunity for experimental validation using non-biological tissues if further developed. This is a topic of particular interest given the difficulty of handling biological tissue samples and ethical considerations.

10.2 Future Studies

Various improvements can be made to the methodologies used throughout this thesis, including deeper analysis of existing data. One aspect that was particularly difficult was managing the wealth of data acquired from a 3D model and comparing it to alternative studies/methods. Every effort was taken to investigate the parameters of greatest interest, but there are many more ways in which this model can be evaluated, such as by assessing the stress/strain over longer periods after loading is applied or closer examination of localised strain rates.

Furthermore, the computational material modelling itself can be varied and increased in complexity. This would be particularly useful to include damage modelling and investigate the dynamics of higher lethality levels/increased loading scenarios. Alternative material models may offer better capture of the lung dynamics, but this is an ongoing topic of discussion. Analysis of viscoelastic material models and the influence of the viscous components would be very beneficial.

More complete experimental validation can be achieved by completed simulations of the tests performed in this thesis. This investigation is particularly difficult due to computational limitations, specifically concerning the quarter scale model and the corresponding reduction in element size/time

step size. This would resolve the uncertainties that remain in the analysis of the experimental results (for external and internal measurements) and experimentally validate the computational model.

Finally, the experimental tests in this thesis were run under sub-optimal conditions and should be re-examined, with consideration of improvements discussed in chapter 8. It is believed that the physical thorax model could be developed further into a more robust ATD model for PBLI with more rigorous and numerous tests, either in its existing form or utilising alternative materials.

In summary, both the computational model and the experimental model serve as an important step in the development of a unified and versatile platform for PBLI research, but both require individual development whilst ensuring they do not begin to differ drastically and can still be utilised together.

11. References

1.   Smith JE. Blast lung injury. J R Nav Med Serv. 2011;97(3):99–105.

2.   Cernak I, Savic J, Zunic G, Pejnovic N, Jovanikic O, Stepic V. Recognizing, scoring, and predicting blast injuries. World J Surg. 1999;23(1):44–53.

3.   Scott TE, Kirkman E, Haque M, Gibb IE, Mahoney P, Hardman JG. Primary Blast Lung Injury - A Review. Br J Anaesth. 2017;118(3):311–6.

4.   Proud WG, Bull AMJ, Masouros S, Pope DJ, Brown KA, Karunaratne A, et al. Blast Injury Science and Engineering. Bull AMJ, Mahoney PF, Clasper J, editors. Springer; 2016.

5.   Boutillier J, Deck C, Magnan P, Wilinger R, Naz P. Primary blast injury on thorax: a critical review of the studies and their outcomes. IRC-15-77 IRCOBI Conf 2015. 2015;(September):708–21.

6.   Greer AD. Numerical Modeling for the Prediction of Primary Blast Injury to the Lung [Internet]. University of Waterloo. 2006. Available from: https://uwspace.uwaterloo.ca/handle/10012/2642

7.   Breeze J, Sedman AJ, James GR, Newbery TW, Hepper AE. Determining the wounding effects of ballistic projectiles to inform future injury models: A systematic review. J R Army Med Corps. 2014;160(4):273–8.

8.   Del Linz P, Fung TC, Lee CK, Riedel W. Response mechanisms of reinforced concrete panels to the combined effect of close-in blast and fragments: An integrated experimental and numerical analysis. Int J Prot Struct. 2021;12(1):49–72.

9.   Breeze J, James GR, Hepper AE. Perforation of fragment simulating projectiles into goat skin and muscle. J R Army Med Corps. 2013;159(2):84–9.

10.   Nguyen TTN, Carpanen D, Stinner D, Rankin IA, Ramasamy A, Breeze J, et al. The risk of fracture to the tibia from a fragment simulating projectile. J Mech Behav Biomed Mater [Internet]. 2020;102:103525. Available from: https://doi.org/10.1016/j.jmbbm.2019.103525

11.   Nyein M. Computational Modeling of Primary Blast Effects on the Human Brain. Massachusetts Institute of Technology; 2013.

12.   Wightman JM, Gladish SL. Explosions and Blast Injuries - A Primer for Clinicians. Ann Emerg Med [Internet]. 2001;37(6):664–78. Available from: http://ovidsp.ovid.com/ovidweb.cgi?T=JS&CSC=Y&NEWS=N&PAGE=fulltext&D=med4&AN=11414480

13.   Josey T. Investigation of Blast Load Characteristics On Lung Injury. University of Waterloo; 2010. Available from: https://uwspace.uwaterloo.ca/handle/10012/5053

14.   Wolf SJ, Bebarta VS, Bonnett CJ, Pons PT, Cantrill S V. Blast injuries. Lancet [Internet]. 2009;374(9687):405–15. Available from: http://dx.doi.org/10.1016/S0140-6736(09)60257-9

15.   Westrol MS, Donovan CM, Kapitanyan R. Blast Physics and Pathophysiology of Explosive Injuries. Ann Emerg Med. 2017;69(1):S4–9.

16.   Watts S, Kirkman E, Bieler D, Bjarnason S, Franke A, Gupta R, et al. Guidelines for using animal models in blast injury research. J R Army Med Corps. 2019;165(1):38–40.

17.   Dewey JM. Measurement of the Physical Properties of Blast Waves. Igra O, Seiler F, editors. Experimental Methods of Shock Wave Research. 2016. 53–86 p.

18.   Lahiri SK, Ho L. Simulation of Rapid Structural Failure Due To Blast Loads From Conventional Weapons (CONWEP). Providence, USA;

19.   Karlos V, Solomos G. Calculation of Blast Loads for Application to Structural Components. Administrative Arrangement No JRC 32253-2011 with DG-HOME Activity A5 - Blast Simulation Technology Development. Sci Tech Res Ser. 2013;

20.   Mougeotte C, Carlucci P, Recchia S, Ji H. Novel Approach to Conducting Blast Load Analyses Using Abaqus / Explicit-CEL. SIMULIA Cust Conf 2010. 2010;1–15.

21.   Ngo T, Mendis P, Gupta A, Ramsay J. Blast Loading and Blast Effects on Structures - An Overview. J Struct Eng. 2007;

22.   Pope DJ. The development of a quick-running prediction tool for the assessment of human injury owing to terrorist attack within crowded metropolitan environments. Philos Trans R Soc B Biol Sci. 2011;366(1562):127–43.

23.   Brien WDO, Kramer JM, Waldrop TG, Frizzell LA, Miller RJ, Blue JP, et al. Ultrasound-induced lung hemorrhage: Role of acoustic boundary conditions at the pleural surface. 2002;111(2).

24.   Kakogiannis D, Van Hemelrijck D, Wastiels J, Palanivelu S, Van Paepegem W, Vantomme J, et al. Assessment of pressure waves generated by explosive loading. C - Comput Model Eng Sci. 2010;65(1):75–93.

25.   Karlos V, Solomos G, Larcher M. Analysis of the blast wave decay coefficient using the Kingery–Bulmash data. Int J Prot Struct. 2016;7(3):409–29.

26.   Teland JA. Review of blast injury prediction models. Norwegian Defence Research Establishment. 2012.

27.   United States Of America Department of Defense. UFC 3-340-02 Structures To Resist The Effects Of Accidental Explosions, With Change 2. Unified Facil Criteria [Internet]. 2008;(September):1–12. Available from: https://www.wbdg.org/FFC/DOD/UFC/ufc_3_340_02_2008_c2.pdf

28.   Agur AM., Dalley AF. Grant's atlas of anatomy. 2016.

29.   Gierczycka D. Investigation of Thorax Response and Potential for Injury in Side Impacts Using Integrated Detailed Human and Vehicle Finite-Element Models. University of Waterloo; 2018.

30.   Samei E, Pelc NJ. Computed Tomography: Approaches, Applications, and Operations. Cham: Springer International Publishing; 2019. 1–470 p. Available from: http://link.springer.com/10.1007/978-3-030-26957-9

31.   Reeves AP, Xie Y, Liu S. Large-scale image region documentation for fully automated image biomarker algorithm development and evaluation. J Med Imaging. 2017;4(2).

32.   Bowen IG, Fletcher ER, Richmond DR. Estimate of man's tolerance to the direct effects of air blast. 1968.

33.   Wood GW, Panzer MB, Shridharani JK, Matthews KA, Capehart BP, Myers BS, et al. Attenuation of blast pressure behind ballistic protective vests. Inj Prev. 2012;19(1):19–25.

34.   Bass CR, Rafaels KA, Salzar RS. Pulmonary injury risk assessment for short-duration blasts. J Trauma - Inj Infect Crit Care. 2008;65(3):604–15.

35.   Axelsson H, Yelverton JT. Chest Wall Velocity as a Predictor of Nonauditory Blast Injury in a Complex Wave Environment. J Trauma Inj Infect Crit Care. 1996;40(3):31–7.

36.   Teland JA, Doormaal A Van, Horst M Van Der, Svinsås E. Single point methods for determining blast wave injury. Norwegian Defence Research Establishment (FFI); 2011.

37.   PAS 300:2018 Civilian Armoured Vehicle. Test Methods for Ballistic and Blast Protection. 2018. p. 56.

38.   Yang C, Dong-hai Z, Ling-ying L, Yong-hui Y, Yang W, Li-wei Z, et al. Simulation of blast lung injury induced by shock waves of five distances based on finite element modeling of a three-dimensional rat. Sci Rep [Internet]. 2019;9(1):1–13. Available from: http://dx.doi.org/10.1038/s41598-019-40176-7

39.   Bouamoul A, Williams K. Effect of human and sheep lung orientation on primary blast injury induced by single blast. Pers Armour Syst Symp. 2010;149–56.

40.   Dharmasena KP, Wadley HNG, Xue Z, Hutchinson JW. Mechanical response of metallic honeycomb sandwich panel structures to high-intensity dynamic loading. Int J Impact Eng. 2008;35(9):1063–74.

41.   Chen A, Louca LA, Elghazouli AY. Behaviour of cylindrical steel drums under blast loading conditions. Int J Impact Eng [Internet]. 2016;88:39–53. Available from: http://dx.doi.org/10.1016/j.ijimpeng.2015.09.007

42.   Stuhmiller JH, Chuong CJ, Phillips YY, Dodd KT. Computer modeling of thoracic response to blast. J Trauma - Inj Infect Crit Care. 1988;28(1):132–9.

43.   Stuhmiller JH, Masiello PJ, Ho KH, Mayorga MA, Lawless N, Arygros G. Biomechanical modeling of injury from blast overpressure. RTO HFM Spec Meet

"Models Aircrew Saf Assess Uses, Limitations Requir Ohio, USA, 26-28 Oct 1998, Publ RTO MP-20 [Internet]. 1998;(January). Available from: https://www.researchgate.net/publication/266469698%0ABiomechanical

44. Teland JA, Skriudalen S. Analysis of the Stuhmiller blast injury model. Norwegian Defence Research Establishment (FFI); 2013.

45. Fung YC, Yen MR, Zeng YJ. Characterization and Modeling of Thoraco-Abdominal Response to Blast Waves: Volume 3. Lung Dynamics and Mechanical Properties Determination. U.S. Army Medical Research and Development Command; 1985.

46. Yen RT, Fung YC, Ho HH, Butterman G. Speed of stress wave propagation in lung. J Appl Physiol. 1986;61(2):701–5.

47. Andrikakou P, Vickraman K, Arora H. On the behaviour of lung tissue under tension and compression. Sci Rep. 2016;6:1–10.

48. Boutillier J, Deck C, Mezzo S De, Magnan P, Prat N, Willinger R, et al. Lung injury risk assessment during blast exposure. J Biomech [Internet]. 2019;86:210–7. Available from: https://doi.org/10.1016/j.jbiomech.2019.02.011

49. Boutillier J, De Mezzo S, Deck C, Ehrhardt L, Magnan P, Naz P, et al. Shock-wave interaction with reduced-scale simplified torso surrogates. 2016 IRCOBI Conf Proc - Int Res Counc Biomech Inj. 2016;(October):428–39.

50. Boutillier J, Prat N, De Mezzo S, Magnan P, Naz P. Blast-Related Lung Injury Risk Estimation Based on Chest Wall Velocity. Hum Factors Mech Eng Def Saf [Internet]. 2021;5(1):1–9. Available from: https://doi.org/10.1007/s41314-021-00038-5

51. Boutillier J, De Mezzo S, Deck C, Magnan P, Naz P, Willinger R. Chest response assessment of post-mortem swine under blast loadings. J Biomech [Internet]. 2017;65:169–75. Available from: https://doi.org/10.1016/j.jbiomech.2017.10.012

52. Noureddine A, Eskandarian A, Digges K. Computer modeling and validation of a Hybrid III dummy for crashworthiness simulation. Math Comput Model. 2002;35(7–8):885–93.

53. Chowdhury M, Crawford D, Shanaman M, Boyle M, Armiger R, Bell C, et al. Polymeric Materials Models in the Warrior Injury Assessment Manikin (WIAMan) Anthropomorphic Test Device (ATD) Tech Demonstrator [Internet]. 2017. Available from: http://www.arl.army.mil/arlreports/2017/ARL-TR-7927.pdf

54. Baker WA, Chowdhury M, Untaroiu CD. A finite element model of an anthropomorphic test device lower limb to assess risk of injuries during vertical accelerative loading. J Biomech [Internet]. 2018;81:104–12. Available from: https://doi.org/10.1016/j.jbiomech.2018.09.020

55. Bouamoul A, Williams K, Levesque H. Experimental and Numerical Modelling of a Mannequin for the Assessment of Blast Incapacitation and Lethality Under Blast Loading. 2007;(April):1189–96.

56. Breeze J, Clasper JC. Determining the velocity required for skin perforation by fragment simulating projectiles: A systematic review. J R Army Med Corps. 2013;159(4):265–70.

57. Roberts JC, Merkle AC, Biermann PJ, Ward EE, Carkhuff BG, Cain RP, et al. Computational and experimental models of the human torso for non-penetrating ballistic impact. J Biomech. 2007;40(1):125–36.

58. Bir CA. The Evaluation of Blunt Ballistic Impacts of the Thorax. Wayne State University, Detroit, Michigan; 2000.

59. Datoc D. Finite element analysis and modeling of a .38 lead round nose ballistic gelatin test. Master's Theses Proj Reports. 2010;(April):87.

60. Humphrey C, Kumaratilake J. Ballistics and anatomical modelling – A review. Leg Med [Internet]. 2016;23:21–9. Available from: http://dx.doi.org/10.1016/j.legalmed.2016.09.002

61. Awad N, El-Dakhakhni WW, Gilani AA. A Physical Head and Neck Surrogate Model to Investigate Blast-Induced Mild Traumatic Brain Injury. Arab J Sci Eng. 2015;40(3):945–58.

62. Singh D, Cronin DS, Haladuick TN. Head and Brain Response to Blast Using Sagittal and Transverse Finite Element Model. Int j numer method biomed eng. 2014;30:470–89.

63. Chafi MS, Karami G, Ziejewski M. Biomechanical assessment of brain dynamic responses due to blast pressure waves. Ann Biomed Eng. 2010;38(2):490–504.

64. Panzer MB, Myers BS, Capehart BP, Bass CR. Development of a finite element model for blast brain injury and the effects of CSF cavitation. Ann Biomed Eng. 2012;40(7):1530–44.

65. Cabello B. Dynamic Stress Analysis of the effect of an Air Blast Wave on a Stainless Steel Plate. Rensselaer Polytechnic Institute, Hartford, Connecticut; 2011.

66. Johnson GR, Cook WH. A Computational Constitutive Model and Data for Metals Subjected to Large Strain, High Strain Rates and High Pressures. Seventh Int Symp Ballist. 1983;541–7.

67. Simulia. Abaqus 6.11

68. Engineering Toolbox [Internet]. Available from: https://www.engineeringtoolbox.com/air-density-specific-weight-d_600.htmlTheory Manual.

69.   Schroeder E, Valdez C, Krauthamer A, Khati N, Rasmus J, Amdur R, et al. Average chest wall thickness at two anatomic locations in trauma. Injury [Internet]. 2013;44(9):1183–5. Available from: http://dx.doi.org/10.1016/j.injury.2013.03.027

70.   Laan D V, Diem T, Vu N, Thiels CA, Pandian TK, Schiller HJ, et al. Chest wall thickness and decompression failure : A systematic review and meta-analysis comparing anatomic locations in needle. Injury [Internet]. 2016;47(4):797–804. Available from: http://dx.doi.org/10.1016/j.injury.2015.11.045

71.   Abrams E, Mohr M, Engel C, Bottlang M. Cross-sectional geometry of human ribs. Cortex. 2003;80:2.

72.   Bellemare F, Jeanneret A, Couture J. Sex differences in thoracic dimensions and configuration. Am J Respir Crit Care Med. 2003;168(3):305–12.

73.   Azhari H. Basics of Biomedical Ultrasound for Engineers [Internet]. Basics of Biomedical Ultrasound for Engineers. Wiley; 2010. Available from: https://onlinelibrary.wiley.com/doi/book/10.1002/9780470561478

74.   Zell K, Sperl JI, Vogel MW, Niessner R, Haisch C. Acoustical properties of selected tissue phantom materials for ultrasound imaging. Phys Med Biol. 2007;52(20).

75.   Kuhn C, Angehrn F, Sonnabend O, Voss A. Impact of extracorporeal shock waves on the human skin with cellulite: A case study of an unique instance. Clin Interv Aging. 2008;3(1):201–10.

76.   Reeve DM. Diagnostic Ultrasound [Internet]. Hoskins PR, Martin K, Thrush A, editors. Vol. 53, Journal of Nuclear Medicine. Third edition. | Boca Raton, FL: CRC Press/Taylor & Francis Group, [2019]: CRC Press; 2019. 1004–1004 p. Available from: https://www.taylorfrancis.com/books/9780429649806

77.   Allisy-Roberts PJ. Farr's Physics for Medical Imaging [Internet]. Elsevier; 2008. Available from: https://linkinghub.elsevier.com/retrieve/pii/C20090343354

78.   Tsaklis P V. Presentation of acoustic waves propagation and their effects through human body tissues. Hum Mov. 2010;11(1):58–65.

79.   Fan TB, Liu ZB, Zhang Z, Zhang D, Gong XF. Modeling of nonlinear propagation in multi-layer biological tissues for strong focused ultrasound. Chinese Phys Lett. 2009;26(8).

80.   Oelze ML, Miller RJ, Blue JP, Zachary JF, O'Brien WD. Estimation of the acoustic impedance of lung versus level of inflation for different species and ages of animals. J Acoust Soc Am. 2008;124(4):2340–52.

81.   Jin Z, Choi Y, Ko SY, Park JO, Park S. Experimental and simulation studies on focused ultrasound triggered drug delivery. Biotechnol Appl Biochem. 2017;64(1):134–42.

82. Freutel M, Schmidt H, Dürselen L, Ignatius A, Galbusera F. Finite element modeling of soft tissues: Material models, tissue interaction and challenges. Clin Biomech [Internet]. 2014;29(4):363–72. Available from: http://dx.doi.org/10.1016/j.clinbiomech.2014.01.006

83. Weed B, Patnaik S, Rougeau-Browning M, Brazile B, Liao J, Prabhu R, et al. Experimental evidence of mechanical isotropy in porcine lung parenchyma. Materials (Basel). 2015;8(5):2454–66.

84. Gallagher AJ, Ní Anniadh A, Bruyere K, Otténio M, Xie H, Gilchrist MD. Dynamic Tensile Properties of Human Skin. IRCOBI Conf. 2012;494–502.

85. Ng BH, Chou SM, Lim BH, Chong A. Strain rate effect on the failure properties of tendons. Proc Inst Mech Eng H. 2004;218(3):203-6. doi: 10.1243/095441104323118923. PMID: 15239571.

86. McKee CT, Last JA, Russell P, Murphy CJ. Indentation Versus Tensile Measurements of Young's Modulus for Soft Biological Tissues. Tissue Eng Part B. 2011;17(3).

87. Shigeta K, Kitagawa Y, Yasuki T. Development of next generation human FE-model capable of organ injury prediction. Proc 21st Enhanc Saf Veh Conf. 2009;(0111):1–20.

88. Shah CS, Yang KH, Hardy W, Wang HK, King AI. Development of a Computer Model to Predict Aortic Rupture Due to Impact Loading. In: SAE Technical Papers [Internet]. 2001. Available from: https://www.sae.org/content/2001-22-0007/

89. Yamada H. Strength of Biological Materials. Evans FG, editor. Williams and Wilkins; 1970. 297 p.

90. Abé H, Hayashi K, Sato M, editors. Data Book on Mechanical Properties of Living Cells, Tissues, and Organs [Internet]. Data Book on Mechanical Properties of Living Cells, Tissues, and Organs. Tokyo: Springer Japan; 1996. Available from: http://link.springer.com/10.1007/978-4-431-65862-7

91. Lee JB, Yang KH. Development of a Finite Element Model of the Human Abdomen. In: SAE Technical Papers [Internet]. 2001. Available from: https://www.sae.org/content/2001-22-0004/

92. Hetherington J, Smith P. Blast and Ballistic Loading of Structures [Internet]. Blast and Ballistic Loading of Structures. CRC Press; 2014. Available from: https://www.taylorfrancis.com/books/9781482269277

93. Wang F, Yang J, Miller K, Li G, Joldes GR, Wittek A, et al. Numerical investigations of rib fracture failure models in different dynamic loading conditions [Internet]. Vol. 00, Computer Methods in Biomechanics and Biomedical Engineering. Taylor & Francis; 2016. p. 0. Available from: http://dx.doi.org/10.1080/10255842.2015.1043905

94. Gibson LJ, Ashby MF. Cellular solids: Structure and properties, second edition [Internet]. Cellular Solids: Structure and Properties, Second Edition. Cambridge University Press;

2014. 1–510 p. Available from:

https://www.cambridge.org/core/product/identifier/9781139878326/type/book

95. Dai Z, Peng Y, Mansy HA, Sandler RH, Royston TJ. Comparison of poroviscoelastic models for sound and vibration in the lungs. J Vib Acoust. 2014;136(5):1–11.

96. Thuraisingham RA. Sound speed in bubbly water at megahertz frequencies. Ultrasonics. 1998;36(6):767–73.

97. Prosperetti A. The speed of sound in a gas–vapour bubbly liquid. Interface Focus. 2015;5(5).

98. Armstrong JD, Gluck EH, Crapo RO, Jones HA, Hughes JMB. Lung tissue volume estimated by simultaneous radiographic and helium dilution methods. Thorax. 1982;37(9):676–9.

99. Williams D, Kenyon A, Adamson D. Basic Science in Obstetrics and Gynaecology [Internet]. Basic Science in Obstetrics and Gynaecology. Elsevier; 2010. 173–230 p. Available from: https://linkinghub.elsevier.com/retrieve/pii/B9780443102813X00012

100. Arora H. Multivariable Calculus for Biomedical Engineers. Lecture presented at; Swansea University; 2020.

101. PolyJet. Material Data Sheets [Internet]. Available from: https://www.stratasys.com/en/materials/materials-catalog/polyjet-materials/

102. Larson K. Estimating Elastic Modulus from Durometer Hardness for Silicones. Dow Corning Corp. 2016;1–6.

103. Alhogbi BG. Examining Variability In The Mechanical Properties Of Parts Manufactured Via PolyJet Direct 3D Printing. J Chem Inf Model [Internet]. 2017;53(9):21–5. Available from: http://www.elsevier.com/locate/scp

104. Pilipović A, Raos P, Šercer M. Experimental analysis of properties of materials for rapid prototyping. Int J Adv Manuf Technol. 2009;40(1–2):105–15.

105. Wang L, Ju Y, Xie H, Ma G, Mao L, He K. The mechanical and photoelastic properties of 3D printable stress-visualized materials. Sci Rep [Internet]. 2017;7(1):1–9. Available from: http://dx.doi.org/10.1038/s41598-017-11433-4

106. Salcedo E, Baek D, Berndt A, Ryu JE. Simulation and validation of three dimension functionally graded materials by material jetting. Addit Manuf [Internet]. 2018;22(May 2017):351–9. Available from: https://doi.org/10.1016/j.addma.2018.05.027

107. Li D, Dong L, Lakes RS. A unit cell structure with tunable Poisson's ratio from positive to negative. Mater Lett [Internet]. 2016;164:456–9. Available from: http://dx.doi.org/10.1016/j.matlet.2015.11.037

108. Slesarenko V, Rudykh S. Towards mechanical characterization of soft digital materials for multimaterial 3D-printing. Int J Eng Sci [Internet]. 2018 Feb;123:62–72. Available from: https://linkinghub.elsevier.com/retrieve/pii/S0020722517306262

109. Dykstra DMJ, Busink J, Ennis B, Coulais C. Viscoelastic snapping metamaterials. J Appl Mech Trans ASME. 2019;86(11).

110. Khalid GA, Bakhtiarydavijani H, Whittington WR, Prabhu R, Jones MD. Material response characterization of three poly jet printed materials used in a high-fidelity human infant skull. Mater Today Proc [Internet]. 2020;20:408–13. Available from: https://doi.org/10.1016/j.matpr.2019.09.156

111. ASTM D1621-16, Standard Test Method for Compressive Properties of Rigid Cellular Plastics, Available from: https://www.astm.org/d1621-16.html

112. ASTM D638-22, Standard Test Method for Tensile Properties of Plastics, Available from: https://www.astm.org/standards/d638

113. Butler BJ, Boddy RL, Bo C, Arora H, Williams A, Proud WG, et al. Composite nature of fresh skin revealed during compression. Bioinspired, Biomim Nanobiomaterials [Internet]. 2015 Jun;4(2):133–9. Available from: https://www.icevirtuallibrary.com/doi/10.1680/bbn.14.00028

114. Arora H, Nila A, Vitharana K, Sherwood JM, Nguyen T-TN, Karunaratne A, et al. Microstructural Consequences of Blast Lung Injury Characterized with Digital Volume Correlation. Front Mater [Internet]. 2017;4(December). Available from: http://journal.frontiersin.org/article/10.3389/fmats.2017.00041/full

115. Thomas GO, Oakley GL. Investigations of Gas Detonations Using Shock Tubes. 1988.

116. Polio SR, Kundu AN, Dougan CE, Birch NP, Ezra Aurian-Blajeni D, Schiffman JD, et al. Cross-platform mechanical characterization of lung tissue. PLoS One. 2018;13(10):1–17.

117. Kikinis R, Pieper S, Vosburgh K. 3D Slicer: A Platform for Subject-Specific Image Analysis, Visualization, and Clinical Support. 2013.